



# **NAVAL POSTGRADUATE SCHOOL**

**MONTEREY, CALIFORNIA**

## **THESIS**

**ANALYSIS OF MICROSTRUCTURE REFINEMENT  
DURING SINGLE-PASS AND MULTI-PASS FRICTION  
STIR PROCESSING OF NIAL PROPELLER BRONZE**

by

Carolyn J. England

September 2010

Thesis Advisor:  
Second Reader:

Terry R. McNelley  
Sarath Menon

**Approved for public release; distribution is unlimited**

THIS PAGE INTENTIONALLY LEFT BLANK

|   |   |  |  |  |
|---|---|--|--|--|
| <b>REPORT DOCUMENTATION PAGE</b>  |   |  | <i>Form Approved OMB No. 0704-0188</i>                     |  |
| Public reporting burden for this collection of information is estimated to average 1 hour per response, including the time for reviewing instruction, searching existing data sources, gathering and maintaining the data needed, and completing and reviewing the collection of information. Send comments regarding this burden estimate or any other aspect of this collection of information, including suggestions for reducing this burden, to Washington headquarters Services, Directorate for Information Operations and Reports, 1215 Jefferson Davis Highway, Suite 1204, Arlington, VA 22202-4302, and to the Office of Management and Budget, Paperwork Reduction Project (0704-0188) Washington DC 20503.   |   |  |  |  |
| <b>1. AGENCY USE ONLY (Leave blank)</b>   |   | <b>2. REPORT DATE</b><br>September 2010                        | <b>3. REPORT TYPE AND DATES COVERED</b><br>Master's Thesis |  |
| <b>4. TITLE AND SUBTITLE</b> Analysis of Microstructure Refinement During Single-Pass and Multi-Pass Friction Stir Processing of NiAl Propeller Bronze  |   |  | <b>5. FUNDING NUMBERS</b>                                  |  |
| <b>6. AUTHOR(S)</b> LT Carolyn J. England   |   |  |  |  |
| <b>7. PERFORMING ORGANIZATION NAME(S) AND ADDRESS(ES)</b><br>Naval Postgraduate School<br>Monterey, CA 93943-5000   |   |  | <b>8. PERFORMING ORGANIZATION REPORT NUMBER</b>            |  |
| <b>9. SPONSORING /MONITORING AGENCY NAME(S) AND ADDRESS(ES)</b><br>ONR  |   |  | <b>10. SPONSORING/MONITORING AGENCY REPORT NUMBER</b>      |  |
| <b>11. SUPPLEMENTARY NOTES</b> The views expressed in this thesis are those of the author and do not reflect the official policy or position of the Department of Defense or the U.S. Government. IRB Protocol Number: N/A  |   |  |  |  |
| <b>12a. DISTRIBUTION / AVAILABILITY STATEMENT</b><br>Approved for public release; distribution is unlimited.  |   |  | <b>12b. DISTRIBUTION CODE</b><br>A                         |  |
| <b>13. ABSTRACT (maximum 200 words)</b><br><br><p>High strength, corrosion resistance, ductility, and toughness are material properties required for United States Navy (USN) Propellers. Propellers for both surface ships and submarines in the USN are currently made from cast Nickel Aluminum Bronze (NAB) Wrought NAB exhibits strength, corrosion resistance, high dampening capacity, low friction coefficients, and good fracture toughness for a wide range of temperatures [1].</p> <p>Casting NAB into large structures lowers some of the qualities seen in wrought material and sought after for the propellers. After casting, some of the structure exhibits high porosity and an undesirable grain structure. Friction Stir Processing (FSP) can be used to refine grain structures and remove pores created during casting. This would reduce or eliminate the need for heat treatment and fusion welding currently being used to prepare Navy propellers.</p> <p>Orientation imaging microscopy was used to aid understanding of friction stir process's effects on grain structure evolution and processes of recrystallization in Nickel Aluminum Bronze. Observations were made about the grain orientation, size, and texture within the stir zone, thermal-mechanically affected zone, and the heat-affected zone for both a single-pass and a multi pass processed pieces of bronze.</p> |   |  |  |  |
| <b>14. SUBJECT TERMS</b><br><br>Friction Stir Processing, Nickel Aluminum Bronze, Propellers, Microstructural Properties, Grain Refinement, Texture   |   |  | <b>15. NUMBER OF PAGES</b><br>107                          |  |
|   |   |  | <b>16. PRICE CODE</b>                                      |  |
| <b>17. SECURITY CLASSIFICATION OF REPORT</b><br>Unclassified  | <b>18. SECURITY CLASSIFICATION OF THIS PAGE</b><br>Unclassified | <b>19. SECURITY CLASSIFICATION OF ABSTRACT</b><br>Unclassified | <b>20. LIMITATION OF ABSTRACT</b><br>UU                    |  |

THIS PAGE INTENTIONALLY LEFT BLANK

**Approved for public release; distribution is unlimited**

**ANALYSIS OF MICROSTRUCTURE REFINEMENT DURING SINGLE-PASS  
AND MULTI-PASS FRICTION STIR PROCESSING OF NIAL PROPELLER  
BRONZE**

Carolyn J. England  
Lieutenant, United States Navy  
B.S., University of Texas at Austin, 2004

Submitted in partial fulfillment of the  
requirements for the degree of

**MASTER OF SCIENCE IN MECHANICAL ENGINEERING**

and

**MECHANICAL ENGINEER**

from the

**NAVAL POSTGRADUATE SCHOOL  
September 2010**

Author: Carolyn J. England

Approved by: Terry R. McNelley  
Thesis Advisor

Sarath Menon  
Second Reader

Knox Millsaps, PhD  
Chairman, Department of Mechanical and Aerospace Engineering



THIS PAGE INTENTIONALLY LEFT BLANK

## **ABSTRACT**

High strength, corrosion resistance, ductility, and toughness are material properties required for United States Navy (USN) Propellers. Propellers for both surface ships and submarines in the USN are currently made from cast Nickel Aluminum Bronze (NAB) Wrought NAB exhibits strength, corrosion resistance, high dampening capacity, low friction coefficients, and good fracture toughness for a wide range of temperatures [1].

Casting NAB into large structures lowers some of the qualities seen in wrought material and sought after for the propellers. After casting, some of the structure exhibits high porosity and an undesirable grain structure. Friction Stir Processing (FSP) can be used to refine grain structures and remove pores created during casting. This would reduce or eliminate the need for heat treatment and fusion welding currently being used to prepare Navy propellers.

Orientation imaging microscopy was used to aid understanding of friction stir process's effects on grain structure evolution and processes of recrystallization in Nickel Aluminum Bronze. Observations were made about the grain orientation, size, and texture within the stir zone, thermal-mechanically affected zone, and the heat-affected zone for both a single-pass and a multi pass processed pieces of bronze.



THIS PAGE INTENTIONALLY LEFT BLANK

## TABLE OF CONTENTS

|             |   |           |
|-------------|---|-----------|
| <b>I.</b>   | <b>INTRODUCTION.....</b>  | <b>1</b>  |
| <b>II.</b>  | <b>BACKGROUND .....</b>   | <b>3</b>  |
| <b>A.</b>   | <b>FRICITION STIR PROCESSING .....</b>  | <b>3</b>  |
| <b>B.</b>   | <b>NICKEL ALUMINUM BRONZE.....</b>  | <b>7</b>  |
|             | 1.    Alpha Phase .....   | 9         |
|             | 2.    Beta Phase.....   | 10        |
|             | 3.    Kappa Phases .....  | 11        |
| <b>C.</b>   | <b>ORIENTATION IMAGING.....</b>   | <b>12</b> |
| <b>III.</b> | <b>EXPERIMENTAL PROCEDURE.....</b>  | <b>15</b> |
| <b>A.</b>   | <b>MATERIAL PROCESSING .....</b>  | <b>15</b> |
| <b>B.</b>   | <b>MICROSTRUCTURE ANALYSIS WITH ORIENTATION<br/>IMAGING.....</b>                  | <b>17</b> |
|             | 1.    Sample Preparation .....  | 17        |
|             | 2.    Orientation Imaging Procedure.....  | 18        |
|             | a.    Mounting the Sample.....  | 18        |
|             | b.    Rotating the Sample.....  | 19        |
|             | c.    Taking Data.....  | 19        |
| <b>IV.</b>  | <b>RESULTS AND DISCUSSION .....</b>   | <b>25</b> |
| <b>A.</b>   | <b>OVERVIEW.....</b>  | <b>25</b> |
| <b>B.</b>   | <b>INVERSE POLE FIGURES AND IMAGE QUALITY MAPS .....</b>                          | <b>25</b> |
|             | 1.    Base Material.....  | 26        |
|             | 2.    Single-Pass .....   | 28        |
|             | 3.    Multi-pass .....  | 31        |
| <b>C.</b>   | <b>MISORIENTATION ANGLES.....</b>   | <b>35</b> |
| <b>D.</b>   | <b>TEXTURE .....</b>  | <b>42</b> |
|             | 1.    Single-Pass Texture.....  | 44        |
|             | 2.    Multipass Texture .....   | 46        |
|             | 3.    FSP Texture Summary .....   | 49        |
| <b>E.</b>   | <b>PLAUSIBLE MODELS FOR FRICTION STIR PROCESSING OF<br/>NAB .....</b>             | <b>51</b> |
|             | 1.    Dynamic Restoration .....   | 51        |
|             | 2.    Grain Boundary Sliding .....  | 52        |
|             | a.    Sequence of Microstructural Development in Ni Al<br>Bronze During FSP ..... | 53        |
|             | b.    Diffusion of Iron in Copper.....  | 54        |
| <b>V.</b>   | <b>CONCLUSIONS .....</b>  | <b>57</b> |
| <b>A.</b>   | <b>CONCLUSIONS FROM RESULTS.....</b>  | <b>57</b> |
| <b>B.</b>   | <b>FUTURE RESEARCH.....</b>   | <b>58</b> |
|             | <b>APPENDIX A – SINGLE-PASS.....</b>  | <b>59</b> |

|                                 |  |    |
|---------------------------------|--|----|
| A.                              | EXTRA DATA AND FIGURES FOR HORIZONTAL CENTERLINE ..... | 59 |
| B.                              | EXTRA DATA AND FIGURES FOR VERTICAL CENTERLINE.....    | 64 |
| APPENDIX B – MULTI-PASS.....    |  | 71 |
| A.                              | EXTRA DATA AND FIGURES FOR HORIZONTAL CENTERLINE ..... | 71 |
| B.                              | EXTRA DATA AND FIGURES FOR VERTICAL CENTERLINE.....    | 80 |
| LIST OF REFERENCES .....        |  | 85 |
| INITIAL DISTRIBUTION LIST ..... |  | 87 |

## LIST OF FIGURES

|            |  |    |
|------------|--|----|
| Figure 1.  | Friction Stir Processing Tool Used to Process Nickel Aluminum Bronze. ....   | 3  |
| Figure 2.  | Friction stir processing illustration showing a) rotating tool with pin; b) application of pressure to force pin into work piece through adiabatic heating and softening; c) creation of stir zone around the tool; d) transversing of tool through work piece. From [4]. ....   | 5  |
| Figure 3.  | Example of FSP Zones Drawn on an Optical Micrograph of the Transverse View of Single-Pass NAB. After [5]. ....   | 6  |
| Figure 4.  | Vertical section of the Cu-Al-5Ni-5Fe equilibrium diagram. (Created by T.R. McNelley) ....   | 8  |
| Figure 5.  | Transformation Products of NAB during Cooling From [7] ....  | 9  |
| Figure 6.  | Image quality of as-cast NAB showing $\alpha$ and $\kappa$ phases ( $\kappa_i$ phase is not present). ....   | 10 |
| Figure 7.  | Sample Kikuchi (a) Pattern. (b) Pattern with indexing ....   | 12 |
| Figure 8.  | Representative axes for EBSD/OIM coordinate system. From [9] ....  | 13 |
| Figure 9.  | Example of a rectangular spiral pattern used for FSP of multiple pass plates. From [4] ....  | 15 |
| Figure 10. | SEM images combined to form the entire Multi-pass 1200 RPM 2 IPM sample image. Stir zone boundary drawn in with dashed line. The circle represents the area that was electropolished. ....   | 16 |
| Figure 11. | Example of Mounted Single-Pass Sample (a) top view (b) bottom view ....  | 19 |
| Figure 12. | Single-pass sample SEM compilation showing black carbon deposits in scan locations. ....   | 21 |
| Figure 13. | Sketch of Data Acquisition Locations for the Single-Pass 1200 RPM 2 IPM Sample. The sample is outlined in black with the stir zone roughly estimated with a blue dotted line. The red *'s and light blue +'s represent locations that data was taken. The scans are numbered in order from the farthest outside the stir zone to the farthest inside the stir zone. Scan 8 will be considered with the analysis of the stir zone for the vertical centerline and will be referred to as scan I ....  | 22 |
| Figure 14. | Multi-pass 1200 RPM 2 IPM SEM image of grain structure around Scans 1-8 and A-E. ....  | 23 |
| Figure 15. | Sketch of Data Acquisition Locations for the Multi-pass 1200 RPM 2 IPM Sample. The Black lines represent the edge of the cut out sample. The blue dotted lines roughly represent the edge of the stir zone as the tool traveled through the material during the last three passes. The red *'s, purple x's, and light blue +'s represent locations that data was taken. The scans are numbered in order from the farthest outside the stir zone to the farthest inside the stir zone. Scan 11 will be considered with the analysis of the stir zone for the vertical centerline and will be referred to as scan F .... | 24 |
| Figure 16. | Representative FCC crystal structure with orientation axis. ....   | 26 |
| Figure 17. | Image quality maps of as cast material in three different scales. ....   | 27 |

|            |  |    |
|------------|--|----|
| Figure 18. | Representative comparison of Single-Pass image quality maps from (a) As Cast (b) HAZ (c) TMAZ (d) Stir Zone .....  | 29 |
| Figure 19. | Representative comparison of Single-Pass IPF from (a) As Cast (b) HAZ (c) TMAZ (d) Stir Zone .....   | 30 |
| Figure 20. | Representative comparison of multi-pass image quality from (a) HAZ (b) TMAZ (c) Stir Zone with one pass of tool (d) stir zone with two passes.....   | 32 |
| Figure 21. | Representative comparison of multi-pass IPF from (a) HAZ (b) TMAZ (c) Stir Zone with one pass of tool (d) stir zone with two passes.....   | 34 |
| Figure 22. | Representative Inverse Pole Figure from inside a multi-pass stir Zone showing annealing twins and a refined grain structure. The black spots represent the $\kappa$ phases. ....                 | 36 |
| Figure 23. | Representative misorientation graph. The Number Fraction of Grain Boundary Misorientation Angles for multipass scan 8.....   | 38 |
| Figure 24. | Number Fraction of Low angle Grain boundaries (a) for single and multipass along horizontal centerline (b) for single and multipass along vertical centerline.....                               | 39 |
| Figure 25. | Number fraction of 60 degree Grain boundary misorientation (a) for single and multipass along horizontal centerline (b) for single and multipass along vertical centerline.....                  | 41 |
| Figure 26. | (a) Sketch of transverse section of FSP multi-pass sample with (b) pole figure axis defined.....   | 43 |
| Figure 27. | Representitive as-cast pole figure with texture pole.....  | 44 |
| Figure 28. | Representative Single-Pass HAZ pole figure with coorisponding texture pole figure. This was taken from Single-Pass scan A.....   | 45 |
| Figure 29. | Representative Single-Pass TMAZ pole figure with coorisponding texture pole figure. This was taken from single-pass scan 5. ....   | 45 |
| Figure 30. | Representative Single-Pass Stir Zone pole figure with coorisponding texture pole figure.This was taken from single-pass scan 7. ....   | 46 |
| Figure 31. | Representative Multipass HAZ pole figure with coorisponding texture pole figure. Taken from the multipass sample scan 2.....   | 47 |
| Figure 32. | Representative Multipass TMAZ pole figure with coorisponding texture pole figure. Taken from the multipass sample scan scan 6.....   | 48 |
| Figure 33. | Representative Multipass Stir Zone pole figure with coorisponding texture pole figure. Images from multi-pass scan 11. ....  | 48 |
| Figure 34. | Peak intensities given by texture pole figures for all data locations. Peak intensities over ten represent a prefered orientation or texture. (a) for single and multipass along horizontal..... | 50 |
| Figure 35. | Sketch of grain structure while at an elevated temperature. (Created by T.R. McNelly).....   | 53 |
| Figure 36. | Sketch of subgrains within the recrystalized primary $\alpha$ grains. (Created by T.R. McNelly).....   | 53 |
| Figure 37. | Sketch of an elongated primary $\alpha$ grain with a diameter about the size of the sub grains. (Created by T.R. McNelly).....   | 54 |
| Figure 38. | Sketch of $\beta$ phase spreading along the primary $\alpha$ subgrains. (Created by T.R. McNelly).....   | 54 |

|            |   |    |
|------------|---|----|
| Figure 39. | Single-Pass Pole Figure with Coorisponding texture pole figure from Scan 1..... | 60 |
| Figure 40. | Single-Pass Pole Figure with coorisponding texture pole figure from Scan 2..... | 60 |
| Figure 41. | Single-Pass Pole Figure with coorisponding texture pole figure from Scan 3..... | 61 |
| Figure 42. | Single-Pass Pole Figure with coorisponding texture pole figure from Scan 4..... | 61 |
| Figure 43. | Single-Pass Pole Figure with coorisponding texture pole figure from Scan 5..... | 62 |
| Figure 44. | Single-Pass Pole Figure with coorisponding texture pole figure from Scan 6..... | 62 |
| Figure 45. | Single-Pass Pole Figure with coorisponding texture pole figure from Scan 7..... | 63 |
| Figure 46. | Single-Pass Pole Figure with coorisponding texture pole figure from Scan 8..... | 63 |
| Figure 47. | Single-Pass Pole Figure with coorisponding texture pole figure from Scan A..... | 65 |
| Figure 48. | Single-Pass Pole Figure with coorisponding texture pole figure from Scan B..... | 65 |
| Figure 49. | Single-Pass Pole Figure with coorisponding texture pole figure from Scan C..... | 66 |
| Figure 50. | Single-Pass Pole Figure with coorisponding texture pole figure from Scan D..... | 66 |
| Figure 51. | Single-Pass Pole Figure with coorisponding texture pole figure from Scan E..... | 67 |
| Figure 52. | Single-Pass Pole Figure with coorisponding texture pole figure from Scan F..... | 67 |
| Figure 53. | Single-Pass Pole Figure with coorisponding texture pole figure from Scan G..... | 68 |
| Figure 54. | Single-Pass Pole Figure with coorisponding texture pole figure from Scan H..... | 68 |
| Figure 55. | Single-Pass Pole Figure with coorisponding texture pole figure from Scan I..... | 69 |
| Figure 56. | Multipass Pole Figure with coorisponding texture pole figure from Scan 1 ...    | 73 |
| Figure 57. | Multipass Pole Figure with coorisponding texture pole figure from Scan 2 ...    | 73 |
| Figure 58. | Multipass Pole Figure with coorisponding texture pole figure from Scan 3 ...    | 74 |
| Figure 59. | Multipass Pole Figure with coorisponding texture pole figure from Scan 4 ...    | 74 |
| Figure 60. | Multipass Pole Figure with coorisponding texture pole figure from Scan 5 ...    | 75 |
| Figure 61. | Multipass Pole Figure with coorisponding texture pole figure from Scan 6 ...    | 75 |
| Figure 62. | Multipass Pole Figure with coorisponding texture pole figure from Scan 7 ...    | 76 |
| Figure 63. | Multipass Pole Figure with coorisponding texture pole figure from Scan 8 ...    | 76 |
| Figure 64. | Multipass Pole Figure with coorisponding texture pole figure from Scan 9 ...    | 77 |
| Figure 65. | Multipass Pole Figure with coorisponding texture pole figure from Scan 10.....  | 77 |

|            |  |    |
|------------|--|----|
| Figure 66. | Multipass Pole Figure with coorisponding texture pole figure from Scan 11..... | 78 |
| Figure 67. | Multipass Pole Figure with coorisponding texture pole figure from Scan 12..... | 78 |
| Figure 68. | Multipass Pole Figure with coorisponding texture pole figure from Scan 13..... | 79 |
| Figure 69. | Multipass Pole Figure with coorisponding texture pole figure from Scan A ..    | 81 |
| Figure 70. | Multipass Pole Figure with coorisponding texture pole figure from Scan B ..    | 81 |
| Figure 71. | Multipass Pole Figure with coorisponding texture pole figure from Scan C ..    | 82 |
| Figure 72. | Multipass Pole Figure with coorisponding texture pole figure from Scan D ..    | 82 |
| Figure 73. | Multipass Pole Figure with coorisponding texture pole figure from Scan E...    | 83 |
| Figure 74. | Multipass Pole Figure with coorisponding texture pole figure from Scan F...    | 83 |

## LIST OF TABLES

|          |   |    |
|----------|---|----|
| Table 1. | ASTM B-148-78 designation C95800 specifications of composition data (wt%) for propeller bronze. From [17] ..... | 7  |
| Table 2. | Chemical Analyses (Wt Pct $\pm$ std. dev.) of Phases in Cast NAB. After [8]. ..                                 | 11 |
| Table 3. | Composition data (wt %). After [4]. .....   | 17 |
| Table 4. | Polishing regime. ....  | 18 |
| Table 5. | Single-Pass Horizontal Centerline Number Fraction of Grain Boundaries at a Misorientation Angle.....            | 59 |
| Table 6. | Single-Pass Vertical Centerline Number Fraction of Grain Boundaries at a Misorientation Angle .....             | 64 |
| Table 7. | Multi-pass Horizontal Centerline Number Fraction of Grain Boundaries at a Misorientation Angle .....            | 72 |
| Table 8. | Multi-pass Vertical Centerline Number Fraction of Grain Boundaries at a Misorientation Angle .....              | 80 |



THIS PAGE INTENTIONALLY LEFT BLANK

## **LIST OF ABBREVIATIONS**

OIM – Orientation Imaging Microscopy  
FSW – Friction Stir Welding  
FSP – Friction Stir Processing  
USN – United States Navy  
NAB – Nickel Aluminum Bronze  
EDM - Electric Discharge Machine  
RPM – Rotations Per Minute  
IPM – Inches Per Minute  
SZ – Stir Zone  
TMAZ – Thermo-Mechanically Affected Zone  
HAZ – Heat Affected Zone  
BCC – Body Centered Cubic  
FCC – Face Centered Cubic  
SEM – Scanning Electron Microscope  
IPF – Inverse Pole Figure  
IQ – Image Quality  
FE-SEM – Field-Emission Scanning Electron Microscope

THIS PAGE INTENTIONALLY LEFT BLANK

## ACKNOWLEDGMENTS

During the course of this research there were extensive amounts of time spent using the Ziess NEON40 SEM. Thank you, Garth “Will” Young and Dr. Sarath Menon for teaching me how to use the SEM and showing me again when I forgot something. Also thank you for working your use of the SEM around my schedule.

Thank you, Dr. Sarath Menon and Dr. Alex Zhilyaev for teaching me how to use the TSL software to best look for sought after knowledge and images. A special thanks to Dr. Menon for your patience with me as I disturbed your work with questions regularly.

To my material science instructors at Naval Postgraduate School, Lieutenant Colonel Randall ‘Ty’ Pollak, Dr. Sarath Menon, and Dr. Terry McNelley, Thank you for giving me the background knowledge necessary for understanding and completing this thesis.

To my thesis advisor Dr. Terry McNelley, thank you for giving me the opportunity to work with you. Your belief in me, support, and direction were very valuable throughout this entire thesis process.

Lastly, I would like to thank my husband Jake for understanding the extra hours needed to be spent working on my thesis. For all the support and extra work you picked up at home, thank you.

THIS PAGE INTENTIONALLY LEFT BLANK

## I. INTRODUCTION

High strength, ductility, and toughness are sought in most material structure applications, including the United States Navy (USN) Propellers. Propellers for both surface ships and submarines in the USN are currently made from cast Nickel Aluminum Bronze (NAB). NAB has many desirable characteristics for marine use. Including but not limited to strength, corrosion resistance, high dampening capacity, low friction coefficients, and good fracture toughness for a wide range of temperatures. [1]

Casting NAB into large propellers lowers some of the qualities seen in wrought material and sought after for the propellers. Large structures like USN propellers have low and variable cooling rates throughout the structure in the casting process. These cooling rates may result in high porosity and a coarse grain structure. Currently, to correct the casting surface defects, the surface is heat-treated, inspected, weld repaired, and re-inspected. Weld repair will be done until no surface pores are apparent. This is time consuming and costly. Also, after use of the propeller and the surface is worn slightly, some porosity of the structure will be revealed and need to be repaired.

Friction Stir Processing (FSP) is a promising technique that can be used to reduce production and repair time/cost for Navy Propellers. FSP refines the grains and removes the casting pores in a processed surface layer. This would reduce or eliminate the need for heat treatment and fusion welding. It is not currently being used because there are still many unknowns and the current research is intended to clarify issues of microstructure evolution.

One unknown is the mechanism of grains deformation during FSP. This thesis will use orientation imaging microscopy (OIM) to look at the grain orientation and texture. The data will be used to examine the possibility that grain movement during deformation involves grain or phase boundary sliding.

THIS PAGE INTENTIONALLY LEFT BLANK

## II. BACKGROUND

### A. FRICTION STIR PROCESSING

“Friction stir processing (FSP) is a solid-state technique that can provide localized modification and control of microstructure in the near-surface regions of a deformable metal” [2]. It originated from friction stir welding (FSW). FSW was discovered and patented at The Welding Institute in Cambridge, England in 1991 [3]. FSW takes two pieces of base metal and welds them together without the addition of any outside welding material. This welding procedure is a solid-state welding process that uses a special tool to move the material already present to create a bond between the two separate pieces of metal.

To prepare two pieces of metal for FSW, they are rigidly clamped together so they do not move when the rotating tool is inserted. The tool consists of a rotating cylinder with a pin, threaded feature, or spiral feature at its end (see Figure 1). The rotating tool is inserted into the metal. The compression and friction cause the material to heat up to a working temperature (below the melting point). The material flows around the tool, and a bond is formed during the severe local deformation taking place around the tool. The tool traverses along the two surfaces to be welded and when completed the tool is removed before cooling. When the metals are cooled, a weld is created. Since FSW does not add any welding material, the chemical composition of the weld is determined by the base metal(s).

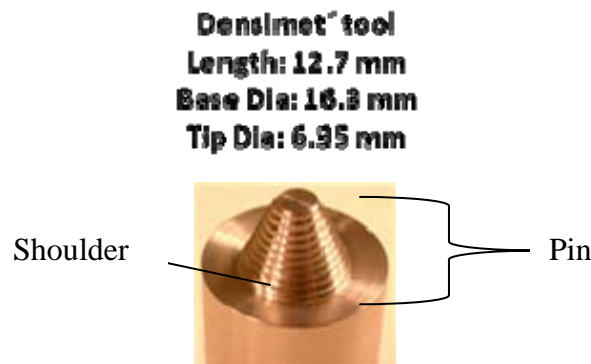


Figure 1. Friction Stir Processing Tool Used to Process Nickel Aluminum Bronze.



Friction Stir Processing uses the same idea but on one piece of metal instead of two. On that single piece of metal, FSP creates a localized thermo-mechanical cycle that refines and homogenizes grains. In as-cast materials, it also removes pores. “The extent of improvements in tensile properties depends on FSP parameters, i.e., tool design, rotation rate, and transversing speed” [2].

FSP uses the same type of tool as FSW, a cylindrical tool with a smaller diameter pin on the end. Depending on the type of processing required, the pin can be threaded, have step diameters, have spirals, have flutes, or be absent completely. See Figure 1 for an example of a step diameter pin shape. This tool is the one used to process material for this study. The larger diameter above the pin is a shoulder that prevents material from moving upward. Like the pin, the shoulder can be designed to have many shapes. See Figure 1 for shoulder location and an example of the shape. Currently, there is research on other applications of FSP with new tool configurations.

The tool is always made of a wear-resistant material. The material needed for the tool depends on the material it is being plunged into. The tool should not deform at the temperatures and forces needed for processing the material. For example, tool steel can be used in aluminum, but tungsten-based alloys should be used in copper and titanium based alloys. The material chosen for the tool to process NAB was Densiment®, which are tungsten particles in a small amount of NiFe or NiCu binder.

Once the proper rotating tool is established for the process, it is rotated and plunged into the metal work-piece, creates a stir zone, and is then traversed over the surface of the material. See Figure 2 for a schematic of initiation of FSP. The shoulder is designed to leave only one direction for the material to move to give way for the tool. The material moves around the sides of the pin as it is traversed. There is an advancing side and a retreating side in the material. (See Figure 2 (d).) On the advancing side, material flows with the direction of tool motion. While on the retreating side it flows against the rotation.

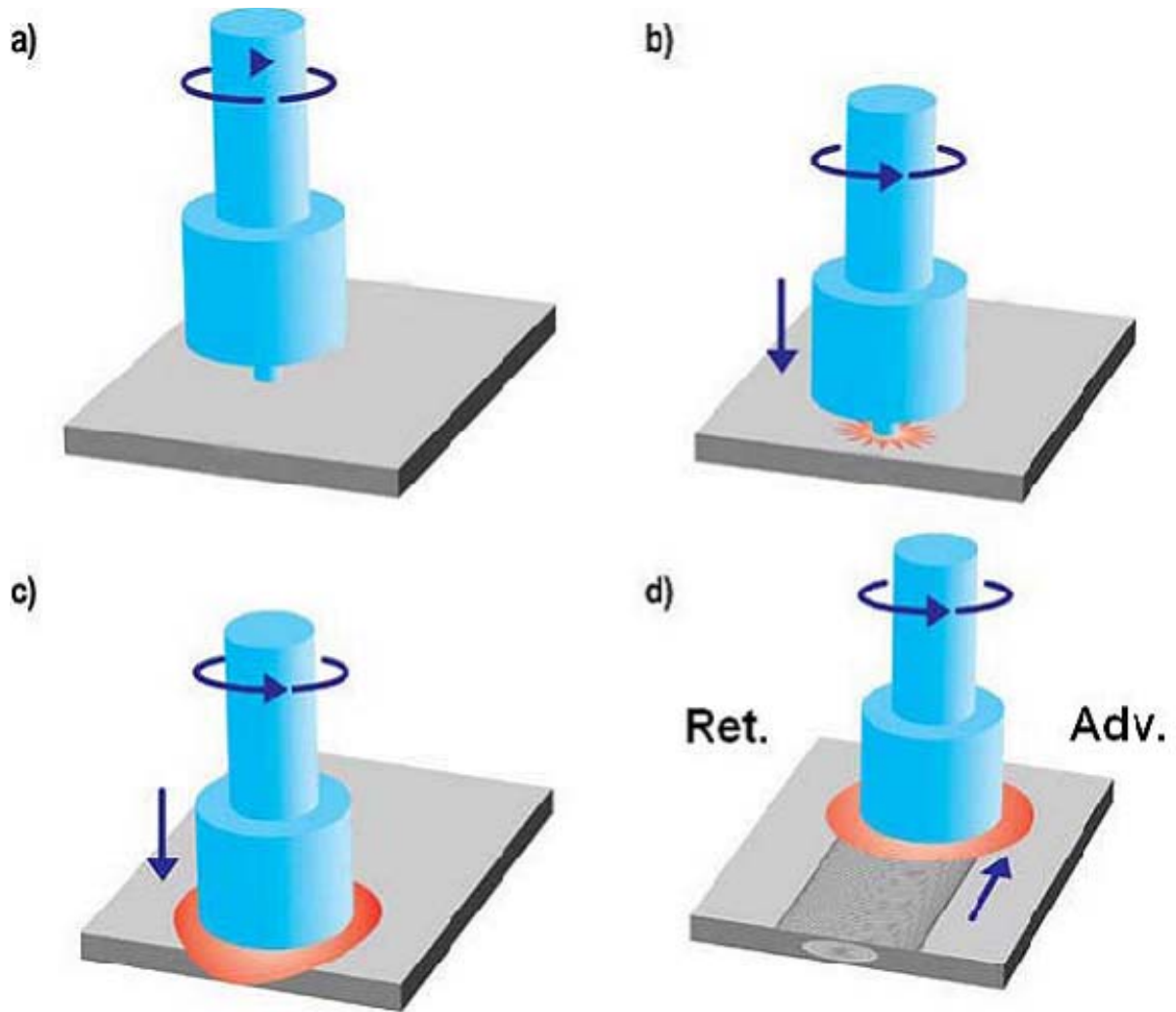


Figure 2. Friction stir processing illustration showing a) rotating tool with pin; b) application of pressure to force pin into work piece through adiabatic heating and softening; c) creation of stir zone around the tool; d) transversing of tool through work piece. From [4].

The movement of material around the pin creates a region of severe deformation, i.e., the Stir Zone (SZ). The size and shape depend on the tool shape, rotation speed, and transverse speed. Inside the SZ the material has experienced large deformations, but also shows large gradients in strains, strain rates, and temperatures. Steeper gradients have been noted on the advancing side [2]. Outside the SZ the material is still affected by the tool but the material does not move around the tool like in the SZ. The region is called the thermo-mechanically affected zone (TMAZ). Grain structure is deformed and

elongated but does not see the same refinement that is seen inside the SZ [4]. The grain structure right outside the TMAZ will also change slightly due to the dissipation of heat from FSP. The grains are not elongated as they are in the TMAZ, but there is a difference in microstructure and mechanical properties from the base material. This region is called the heat-affected zone (HAZ) [2]. Regions are represented in an optical micrograph of a Single-Pass friction stir processes sample of NAB in Figure 3.

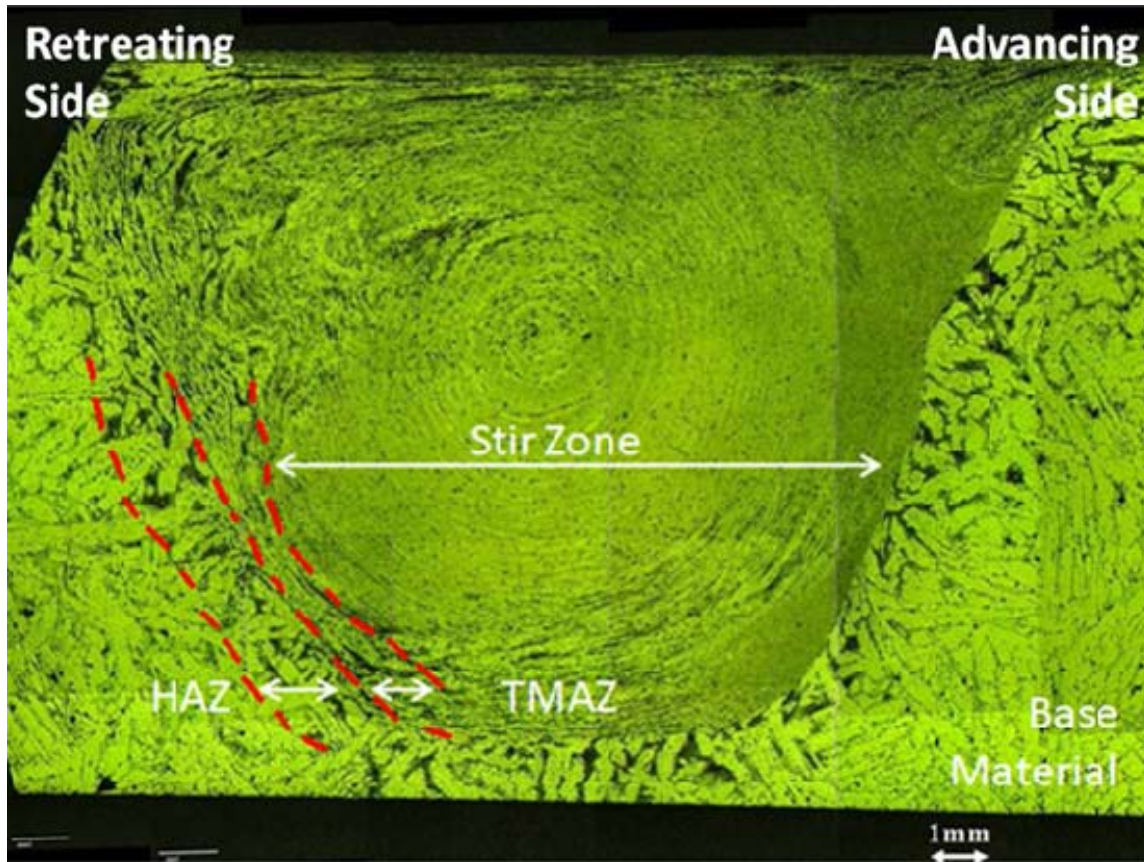


Figure 3. Example of FSP Zones Drawn on an Optical Micrograph of the Transverse View of Single-Pass NAB. After [5]

In Figure 3, there is a difference in grain structure between the advancing side and the retreating side. On the advancing side, there are definitive boundaries between the zones. In this Figure, there is not a large TMAZ on the advancing side. By changing tool parameters, larger TMAZ have been observed [4]. The retreating side has gradual and undefined borders of each of the zones.

With the changed properties in the SZ, TMAZ, and the HAZ, all applications of FSP and FSW have shown signs of microstructure refinement and surface strengthening [6]. FSW and FSP have mostly been used for aluminum and aluminum alloys where fusion welding is difficult. They have also been used with many other alloys such as copper, nickel, titanium, magnesium, and steels. In addition, each processed alloy had other material characteristics that changed from the base material. Some changes were improvements and some were not. This study looked at nickel aluminum bronze (NAB).

## B. NICKEL ALUMINUM BRONZE

Nickel aluminum bronze is nominally Cu-9 wt pct Al-5 wt pct Ni- 4 wt pct Fe. It has good resistance to corrosion, fatigue, and erosion, which makes it good for use in marine environment [1]. The different alloying compositions of NAB yield different material qualities. One composition has earned the nickname of propeller bronze from its use in ship propellers. Its alloying compositions are given in Table 1.

Table 1. ASTM B-148-78 designation C95800 specifications of composition data (wt%) for propeller bronze. From [17]

| Element | Cu         | Al      | Ni      | Fe      | Mn     | Si         | Pb         |
|---------|------------|---------|---------|---------|--------|------------|------------|
| Min-Max | (min) 79.0 | 8.5-9.5 | 4.0-5.0 | 3.5-4.5 | .8-1.5 | 0.10 (max) | 0.03 (max) |
| Nominal | 81         | 9       | 5       | 4       | 1      | -          | -          |

A schematic representation of a vertical section in a quaternary phase diagram in the Cu-Al-Ni-Fe system is shown in Figure 4. This was drawn based on analysis in [8] and [2] of the constitution of NAB materials. The nominal composition and composition range for the NAB material of interest here is indicated in Figure 4. During FSP of NAB, the peak temperature inside the stir zone is between 800 and 1000 degrees Celsius [4], and thus the material deforms in a two-phase region of  $\alpha$  and  $\beta$  phases.

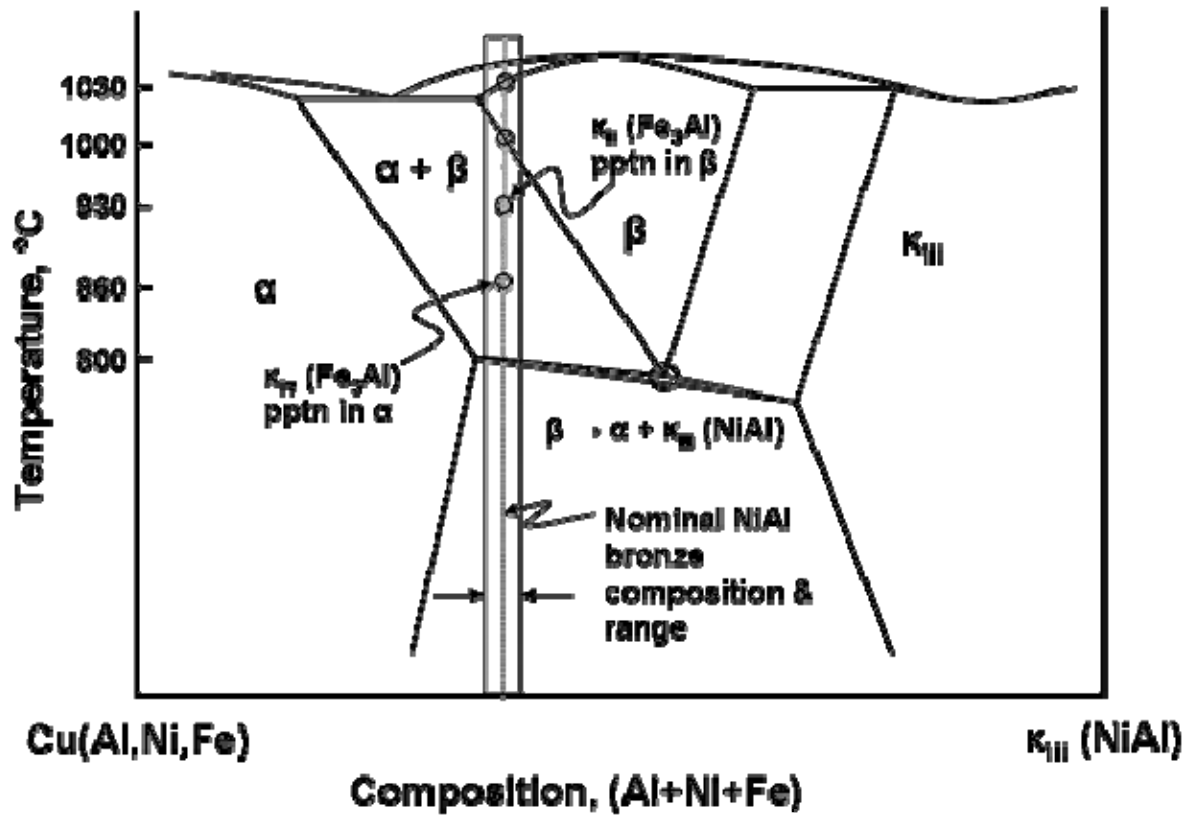


Figure 4. Vertical section of the Cu-Al-5Ni-5Fe equilibrium diagram.  
(Created by T.R. McNelley)

To cast a propeller, NAB is melted and poured into a sand mold. Once in the mold, it cools. Around 1070°C, the bronze solidifies and slowly cools at an equilibrium rate of approximately  $10^{-3} \text{ } ^\circ\text{C s}^{-1}$  [4]. During solidification, the bronze forms a  $\beta$  phase. As this  $\beta$  phase is cooled, an  $\alpha$  phase forms in the  $\beta$  with Widmanstätten morphology [7]. Below 930°C, the globular  $\kappa_{II}$  phase forms from some of the  $\beta$  phase [7]. Below 860°C, the  $\kappa_{IV}$  precipitates in the  $\alpha$ . Below 800°C, the remaining  $\beta$  phase transforms into  $\alpha$  and  $\kappa_{III}$  in a lamellar eutectoid [7]. Once completely cooled, there are four phases present,  $\alpha$ ,  $\kappa_{II}$ ,  $\kappa_{III}$ , and  $\kappa_{IV}$ . A summary of equilibrium cooling is represented in the left side of Figure 5.

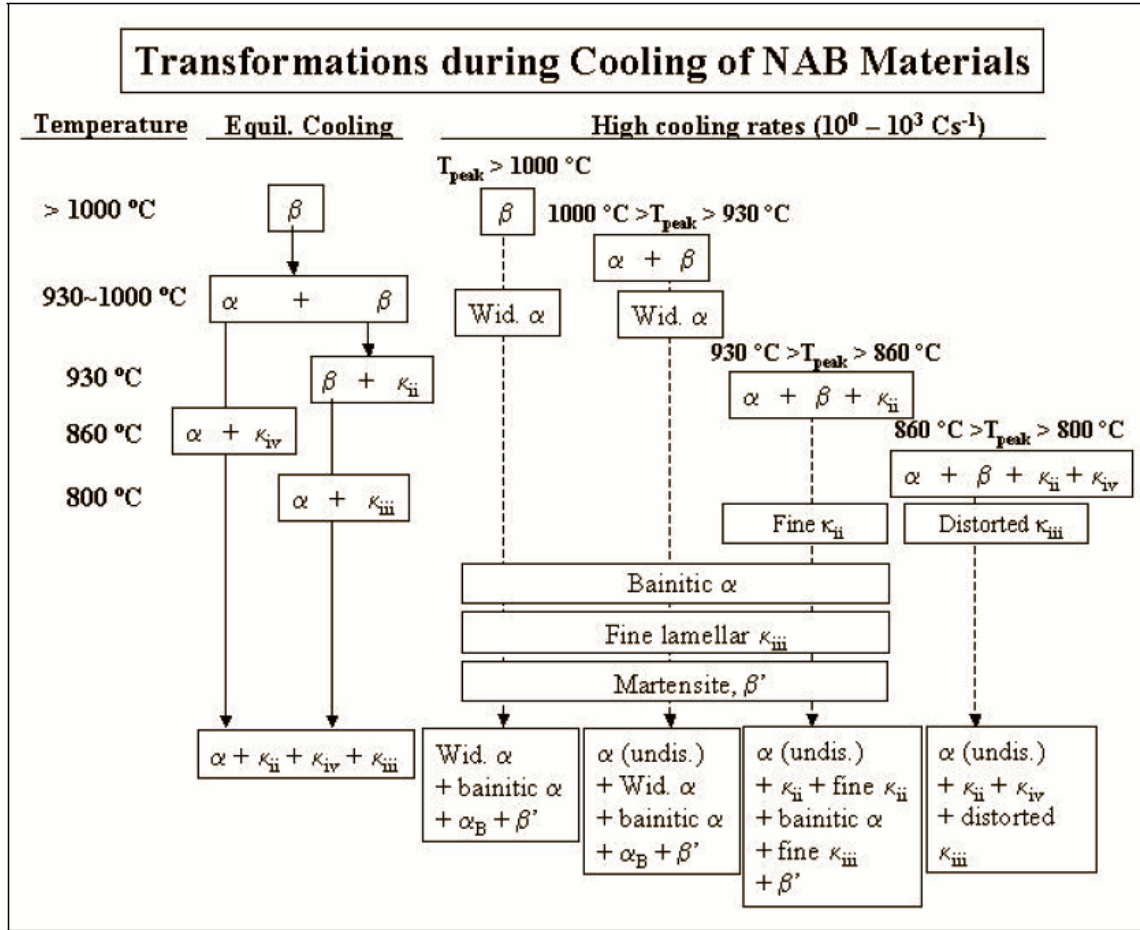


Figure 5. Transformation Products of NAB during Cooling From [7]

## 1. Alpha Phase

The  $\alpha$  phase is copper rich with a face centered cubic (FCC) structure. The lattice parameter is  $3.64 \pm 0.04 \text{ \AA}$  [8]. When a cast sample is at room temperature, this phase makes up most of the cast NAB structure. See Figure 6 for an image quality map of as-cast NAB created by equilibrium cooling. Table 2 shows the weight percent of elements making up the  $\alpha$  phase and all other phases.

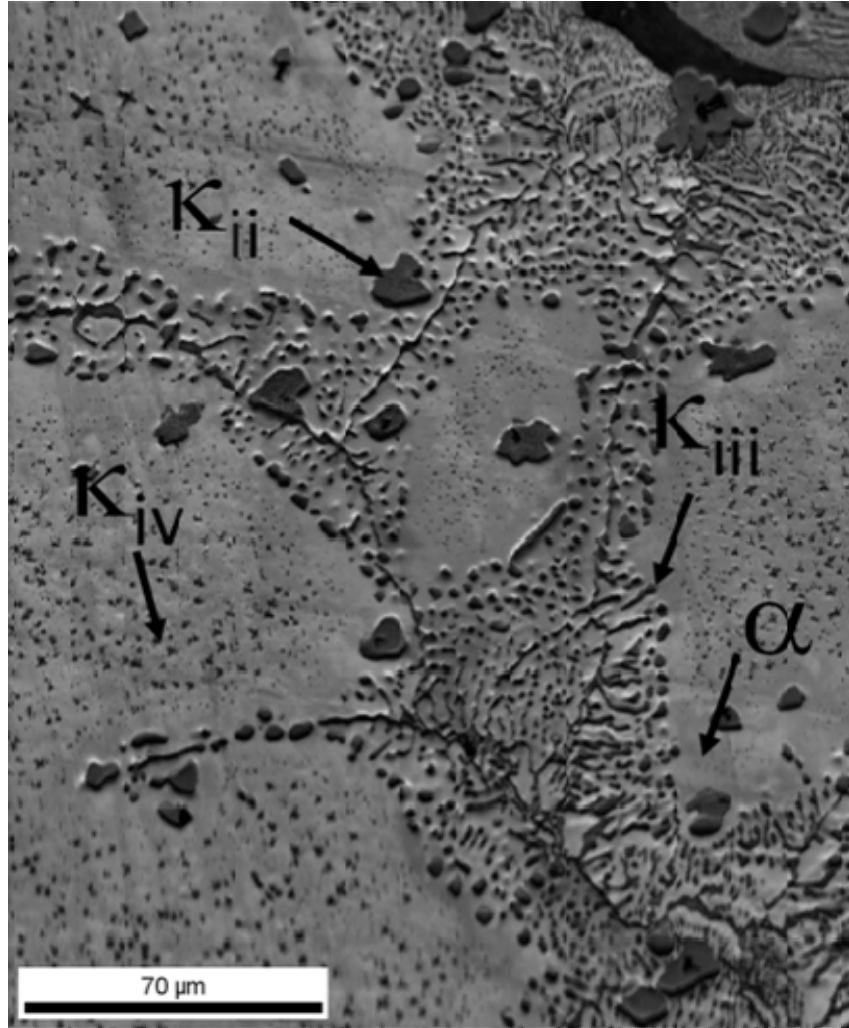


Figure 6. Image quality of as-cast NAB showing  $\alpha$  and  $\kappa$  phases ( $\kappa_i$  phase is not present)

## 2. Beta Phase

The  $\beta$  phase in a Cu-Al-Ni-Fe alloy exists at high temperatures and has a body centered cubic (BCC) structure [8]. When cooled to room temperature with a variety of  $\kappa$  phases precipitate (discussed in the next section) during slow cooling and eventually the eutectoid transformation occurs. At very high quenching rates, a martensitic transformation can occur, and under moderate cooling rates, a bainitic transformation is also possible. The martensite is a B2 structure with a lattice parameter of  $2.85 \pm 0.03 \text{ \AA}$  [8]. The B2 structure is a BCC structure with one element in the center and the other in the corners.

### 3. Kappa Phases

There are four different  $\kappa$  phases. The first one  $\kappa_i$  is created only when there is a large enough iron content. When created, the  $\kappa_i$  phase is a large (20-50  $\mu\text{m}$  diameter) dendrite shaped particle in the center of  $\alpha$  grains [8]. Unlike all the other phases,  $\kappa_i$  is defined by its shape and location not its microstructure. It exhibits multiple microstructures including an iron rich BCC,  $\text{Fe}_3\text{Al}$  in a  $\text{DO}_3$  structure, and  $\text{FeAl}$  in a B2 structure [8].

The second phase,  $\kappa_{ii}$ , looks a lot like  $\kappa_i$  but is smaller (5-10  $\mu\text{m}$  diameter) and located in regions close to  $\kappa_{iii}$  since both are transformation products of the  $\beta$  phase that is present below 930°C.  $\kappa_{ii}$  is mostly  $\text{Fe}_3\text{Al}$  with a  $\text{DO}_3$  structure. There are some substitutions for Iron and Aluminum in the microstructure but it remains in a  $\text{DO}_3$  structure. The weight percentage of all the elements in  $\kappa_{ii}$  can be seen in Table 2. The overall lattice parameter for this  $\text{DO}_3$  structure is  $5.71 \pm 0.06\text{\AA}$ .

The third phase,  $\kappa_{iii}$ , is a lamellar eutectoid decomposition product. It can be identified by its linear or elongated morphology in Figure 6. It is mostly  $\text{NiAl}$  with a B2 structure and a lattice parameter of  $2.88 \pm 0.03\text{\AA}$  [8]. Like  $\kappa_{ii}$  the  $\kappa_{iii}$  phase has substitutions in the structure for other elements in the place of nickel. For overall weight percentages in the structure see Table 2.

The fourth  $\kappa$  phase,  $\kappa_{iv}$ , is a precipitate formed as the  $\alpha$  phase cools. It is distributed throughout the  $\alpha$  grains in a range of sizes.  $\kappa_{iv}$  has a similar structure and composition to  $\kappa_{ii}$ .  $\kappa_{iv}$  is nominally  $\text{Fe}_3\text{Al}$  in a  $\text{DO}_3$  structure with a lattice parameter of  $5.77 \pm 0.06\text{\AA}$  [8].

Table 2. Chemical Analyses (Wt Pct  $\pm$  std. dev.) of Phases in Cast NAB. After [8]

| Phases         | Al             | Si            | Mn            | Fe             | Ni             | Cu             |
|----------------|----------------|---------------|---------------|----------------|----------------|----------------|
| $\kappa_i$     | $9.3 \pm 0.5$  | $1.6 \pm 0.4$ | $2.9 \pm 0.5$ | $72.2 \pm 1.4$ | $3.5 \pm 0.4$  | $10.5 \pm 1.0$ |
| $\kappa_{ii}$  | $12.3 \pm 1.3$ | $4.1 \pm 0.8$ | $2.2 \pm 0.2$ | $31.3 \pm 4.9$ | $8.0 \pm 1.8$  | $12.1 \pm 3.1$ |
| $\kappa_{iii}$ | $26.7 \pm 1.0$ | $< 0.1$       | $2.0 \pm 0.4$ | $12.8 \pm 1.6$ | $41.3 \pm 6.0$ | $17.0 \pm 4.6$ |
| $\kappa_{iv}$  | $10.5 \pm 1.7$ | $4.0 \pm 0.5$ | $2.4 \pm 0.2$ | $73.4 \pm 2.3$ | $7.3 \pm 1.5$  | $2.6 \pm 0.7$  |
| $\beta'$       | $28.1 \pm 0.8$ | $0.4 \pm 0.3$ | $2.2 \pm 0.3$ | $14.0 \pm 6.0$ | $35.1 \pm 8.6$ | $20.2 \pm 3.7$ |
| $\alpha$       | $7.2 \pm 0.4$  | $< 0.1$       | $1.1 \pm 0.1$ | $2.8 \pm 0.3$  | $3.0 \pm 0.2$  | $85.8 \pm 0.4$ |



### C. ORIENTATION IMAGING

Orientation Imaging Microscopy (OIM) is used to determine lattice orientations in a microstructure. These orientations can be used, in turn, to determine grain boundaries, misorientation angle between grains, grain texture, pole plots, and much more.

In OIM an electron beam is incident on the sample at a point. The sample is rotated to an angle of 70 degrees to the horizontal. Diffracted electrons hit a phosphor screen creating a Kikuchi pattern. The Kikuchi pattern is made up of straight lines that create intersecting bands. See Figure 7 for a sample pattern. Depending on the structure and orientation of the lattice in the sample, the bands will be oriented differently.

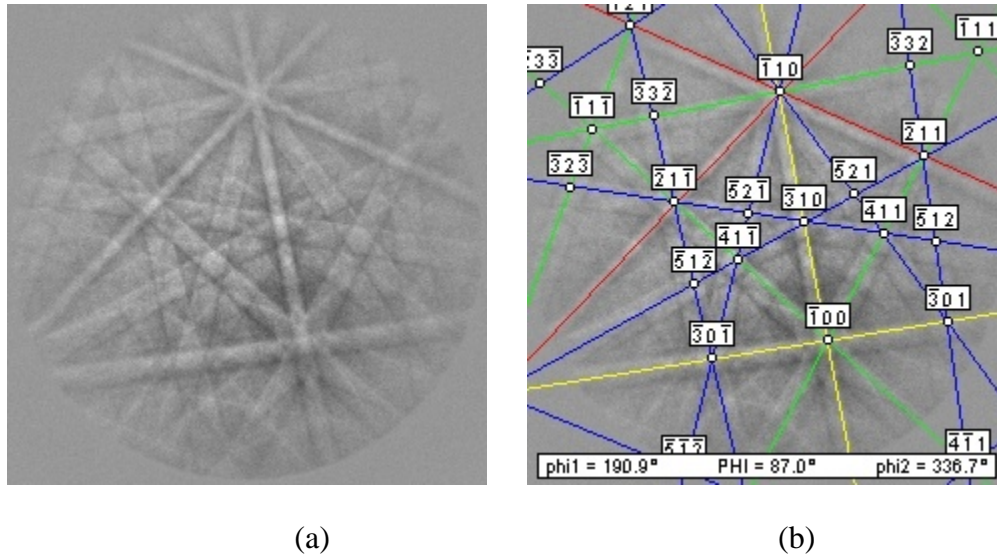


Figure 7. Sample Kikuchi (a) Pattern. (b) Pattern with indexing.

Software analyzes the Kikuchi patterns and determines the Euler angles that describe the lattice orientation. The EBSD hardware used in OIM were developed by TEXSEM, Inc. The software used to take orientation imaging data was OIM 5.3 by TSL which is a subsidiary of EDAX Inc. EDAX Inc. is a business unit of AMETEK Inc., Materials Analysis Division.

The OIM software requires that external reference axes be defined to ensure proper analysis. These axes are the reference/rolling direction (RD), the normal direction (ND) and the Transverse direction (TD). RD is assigned as a positive downward along

the sample surface. ND is assigned as normal to the sample surface toward the phosphor screen. TD is assigned parallel to horizontal along the sample surface [9]. See Figure 8 for a sample setup with defined axes.

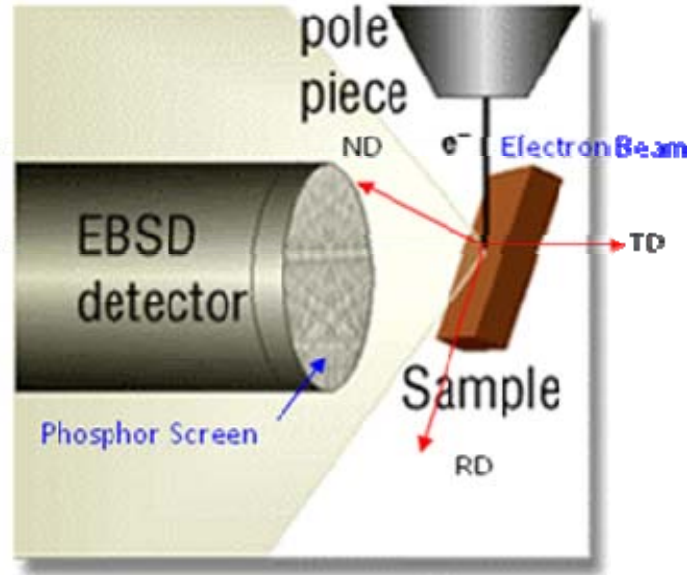


Figure 8. Representative axes for EBSP/OIM coordinate system. From [9]

Once the Kikuchi pattern is created and axes are defined, the software can compare the pattern to a known lattice parameter and crystalline structure. The bands on the Kikuchi pattern will intersect at a different spacing for each rotation of the crystalline structure. The spacing of the intersection points can be used to define the orientation within a certain confidence index. See Figure 7 for a Kikuchi pattern with an indexed orientation. If the point is below a certain confidence, then the point is usually along a grain boundary where there are two orientations in the same area.

Any rotation of the crystal lattice can be defined with three rotation angles about the defined axes. The software finds and stores the three rotation angles at each position and moves on to the next one. At each data point, the software also identifies and records image quality, confidence index, and phase.

TSL software allows the user to define multiple phases in the structure as long as they have unique distinguishable crystal structures. Since the  $\alpha$  and  $\kappa$  phases of NAB are

distinguishable from one another, OIM will work for yielding high quality data/images of NAB  $\alpha$  phase. Since the three  $\kappa$  phases are ordered cubic with similar lattice parameters, they are not distinguishable from one another and will be lumped together for most of the discussion.

Once the data is stored for each point, the software can analyze this data in many different ways, such as creating pole figures, grain boundary maps, and color-coordinated orientation maps. Only a few of many techniques provided by the software will be used to analyze friction stir processes of NAB.

### III. EXPERIMENTAL PROCEDURE

#### A. MATERIAL PROCESSING

The material samples used were two of the four samples studied by Nelson [4].

This is the materials' background:

Nickel aluminum bronze plates were processed using friction stir processing (FSP) by Rockwell Scientific Corporation (now Teledyne Scientific Company) using several different RPM and IPM combinations. A step-spiral Densimet® tool (See Figure 1 for an image of the tool) with a shoulder diameter of 12.7 mm was used for this processing. Densimet® is a tungsten-iron powder metallurgy material with elevated temperature strength and erosion resistance when used for FSP of nickel aluminum bronzes. From these plates, several samples were cut using a computer controlled Charmilles Andrew EF630 electric discharge machine (EDM) and a consumable brass cutting wire with a nominal diameter of 0.30 mm. Of these sample cuts, [two] were chosen that were sectioned so that the transverse plane (normal to the direction of tool travel) would be visible for analysis. [4]



Figure 9. Example of a rectangular spiral pattern used for FSP of multiple pass plates. From [4]

[One] sample came from a plate that was processed with a single FSP pass using a tool rotational speed of 1200 RPM and a tool traversing rate of 2 IPM. This created a SZ that was 2.6 cm across and 1.2 cm deep. The [second] sample came from a plate that was processed with multiple FSP passes using a tool rotational speed of 1200 RPM and a tool traversing rate of 2 IPM. This was done in a rectangular spiral pattern [Figure 9] by working from the inside to the outside of the plate and keeping the

advancing side of the tool to the outside of the plate. A step over distance of 4.5 mm was maintained between consecutive passes. The final area processed was 9.8 cm across and 22.5 cm long. The SZ examined in this sample was 2.9 cm long (due to the location of cutting of the sample) and 1.2 cm deep. [4]

Figure 10 shows a montage of SEM images from the transverse plane of the multi-pass sample after polishing. The circular ring in the center was created from material deposits along the electropolishing aperture during the electropolishing process. A black dotted line was drawn to help identify the stir zone boundary.

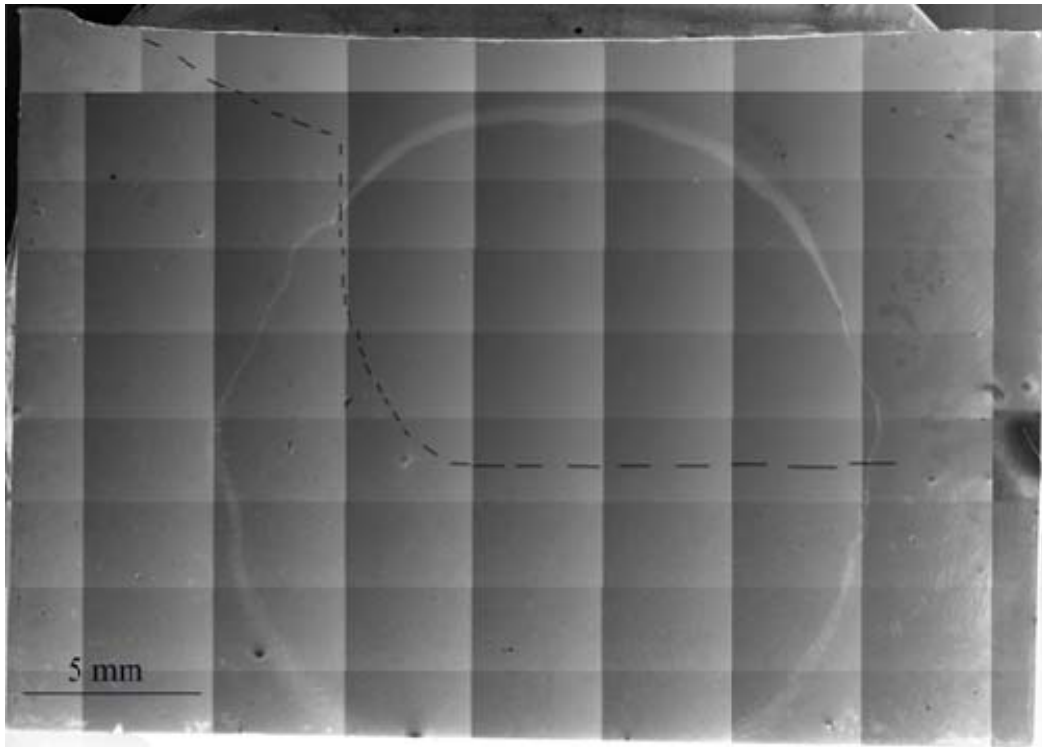


Figure 10. SEM images combined to form the entire Multi-pass 1200 RPM 2 IPM sample image. Stir zone boundary drawn in with dashed line. The circle represents the area that was electropolished.

Composition data for the samples of this investigation are as shown in Table 3.

Table 3. Composition data (wt %). After [4]

| Element | Cu   | Al   | Ni   | Fe   | Mn   | Si   | Pb     |
|---------|------|------|------|------|------|------|--------|
| 1200/2  | 81.3 | 9.17 | 4.46 | 3.68 | 1.24 | 0.06 | <0.005 |

For orientation imaging in the Zeiss Neon 40 field-emission scanning electron microscope (FE-SEM), the sample must be thin and small enough that when rotated in the microscope's vacuum chamber, it will not touch any camera or microscope lens. The single-pass sample was cut in half with the EDM to make it thin enough for rotation in the chamber.

## **B. MICROSTRUCTURE ANALYSIS WITH ORIENTATION IMAGING**

### **1. Sample Preparation**

Sample preparation was conducted in three phases including grinding, polishing, and electropolishing. The first step was to grind the surface using a Buehler ECOMET 4 Variable Speed Grinder-Polisher. This was done using a succession of fine grit SiC sandpapers (600 grit, 2400 grit, then 4000 grit) with an abundance of water, for about 5 minutes per sandpaper grit at 120 RPM. Upon completion of each step of grinding, the sample was rinsed well with water.

Second, using a Buehler ECOMET 3 Variable Speed Grinder-Polisher, samples were polished to a mirror finish. This was accomplished by first using 3 $\mu$  Buehler MetaDi Monocrystalline Diamond Suspension (water based) for 10 minutes at 100 RPM. Then, further polishing was done using 1 $\mu$  Buehler MetaDi Monocrystalline Diamond Suspension (water based) for 10 minutes at 100 RPM. The next step for polishing was accomplished using Buehler Mastermet 0.05 $\mu$  Colloidal Silica Polishing Suspension at 100 RPM until the samples were completely scratch-free with a mirror finish. Between each step of polishing, samples were rinsed with generous amounts of water. Upon completion of polishing, the samples were ultrasonically cleaned for 10 minutes in methanol and dried with a hot air gun.

Third, the sample was electro polished using a solution of 33% Nitric Acid – 67% Methanol at 0°C. It was polished for 3 sec at 15 Amps. Immediately after polishing, the sample was rinsed thoroughly with methanol and dried with a hot air gun. This step leaves a ring of removed material around the periphery of the polishing area. The size of the ring is dependent on the electro polishing apparatus used. A summary of the polishing is in the Table 4.

Table 4. Polishing regime.

| Step | Abrasive Material                  | Time      | RPM |
|------|------------------------------------|-----------|-----|
| 1    | 600 Grit SiC Paper                 | 5 min     | 120 |
| 2    | 2400 Grit SiC Paper                | 5 min     | 120 |
| 3    | 4000 Grit SiC Paper                | 5 min     | 120 |
| 4    | 3 Micron Metadi Diamond Suspension | 15 min    | 100 |
| 5    | 1 Micron Metadi Diamond Suspension | 15 min    | 100 |
| 6    | 0.05 micron Colloidal Silica       | 10-25 min | 100 |
| 7    | 33% Nitric Acid - 67% Methanol     | 3 sec     | N/A |

## 2. Orientation Imaging Procedure

Orientation Imaging was done using the Zeiss NEON 40 FE-SEM with TSL's OIM Data collection 5 software.

### *a. Mounting the Sample*

The polished sample was mounted onto a circular disc specifically designed for use in the Zeiss FE-SEM (Figure 11). To mount the sample, fast drying silver paint was placed on the disc where the sample was touching it. Fast drying paint consists of silver suspended in Iso-Butyl Methyl Ketone. The sample was put on the silver painted disc and placed in a vacuum chamber for fifteen minutes to remove any air in between the sample and the disc. The sample was then checked for a secure bond. If the bond was not secure, the sample was removed, disc cleaned, and the sample remounted on the disc.

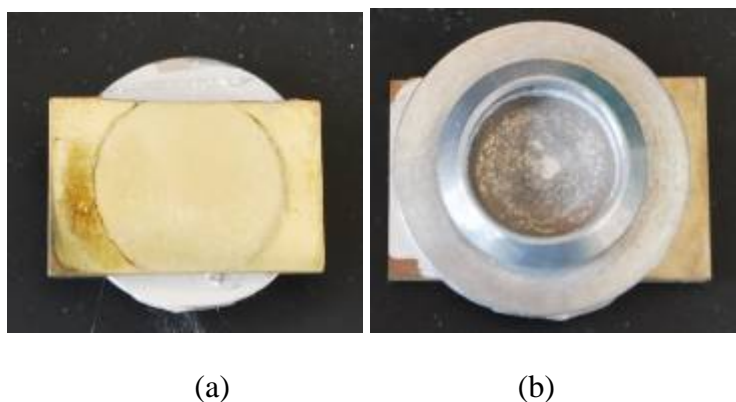


Figure 11. Example of Mounted Single-Pass Sample (a) top view (b)bottom view.

Once the sample was securely mounted to the disc, the disc and sample were placed on a pedestal in the Zeiss SEM. This pedestal has an attachment that snaps into the bottom portion of the disc. Once attached to the pedestal, the sample, disc, and pedestal were placed into the vacuum chamber and the door closed. While the chamber was open, Nitrogen at 10 psig was fed into the chamber to help displace atmospheric oxygen around the sample. Once the door was closed, Nitrogen filled the chamber and a vacuum was drawn.

***b. Rotating the Sample***

Once the sample was in the SEM chamber, the sample was moved into position at a working distance of 15 mm. Then, the horizontal sample was rotated. The sample needs to remain in focus and centered as it is rotated.

The tilt of the pedestal was adjusted to 70-degree in small angle increments, one to five degrees. Every time the tilt was adjusted, the microscope was focused again to maintain a centered sample position and checked to make sure the sample would not touch any equipment in the chamber with the next rotation.

***c. Taking Data***

Once the sample was in position, the data collection was done using the TSL software associated with OIM. The software controls the phosphorous lens that was inserted to take data. Once the lens was inserted, the contrast was adjusted to the proper level.



The first was to collect a good background image. The gain, exposure rate, and darkness were adjusted until the sample was properly exposed to the electron beam. Once those were set, a background image was taken and set to be subtracted from every image taken.

The second step was to define the crystal structure of the phases that were in the sample. The phases used were the copper FCC already present in the software package and generic BCC phase with a lattice parameter of 0.288  $\mu\text{m}$ . These two phase represent the  $\alpha$  phase and the  $\kappa_{\text{iii}}$  phase. From optical microscopy done by Nelson [4] it was seen that there was no  $\kappa_{\text{i}}$  or  $\beta'$  present. The other  $\kappa$  phases were indistinguishable from one another. It is likely that they are indistinguishable from  $\kappa_{\text{iii}}$  since the inter atom distances in the  $\text{DO}_3$  structure of the  $\kappa_{\text{ii}}$  and  $\kappa_{\text{iv}}$  are nearly the same as the inter atom distance in the B2 structure of the  $\kappa_{\text{iii}}$ . The software used the lattice parameter and crystal structure to help index each Kikuchi pattern.

The third step was to capture a SEM image and set up a scan. The scan area was located in the center of the captured SEM since that is the origin of the reference angles. The confidence index decreased as the scan got farther from the origin. The step size for the scan was small enough that there are several points taken for each grain, 0.25 microns was used. Before starting each scan it was double-checked that the indexing was valid and confidence indexes were high for several points in the scan area.

For the single-pass sample, there were a total of sixteen positions in the SZ, TMAZ, and HAZ where orientation data was collected. These positions can be seen in Figure 12 and 13. Data was taken in a horizontal line that incorporates the advancing side of the stir zone along with a vertical line from base material up into the stir zone.

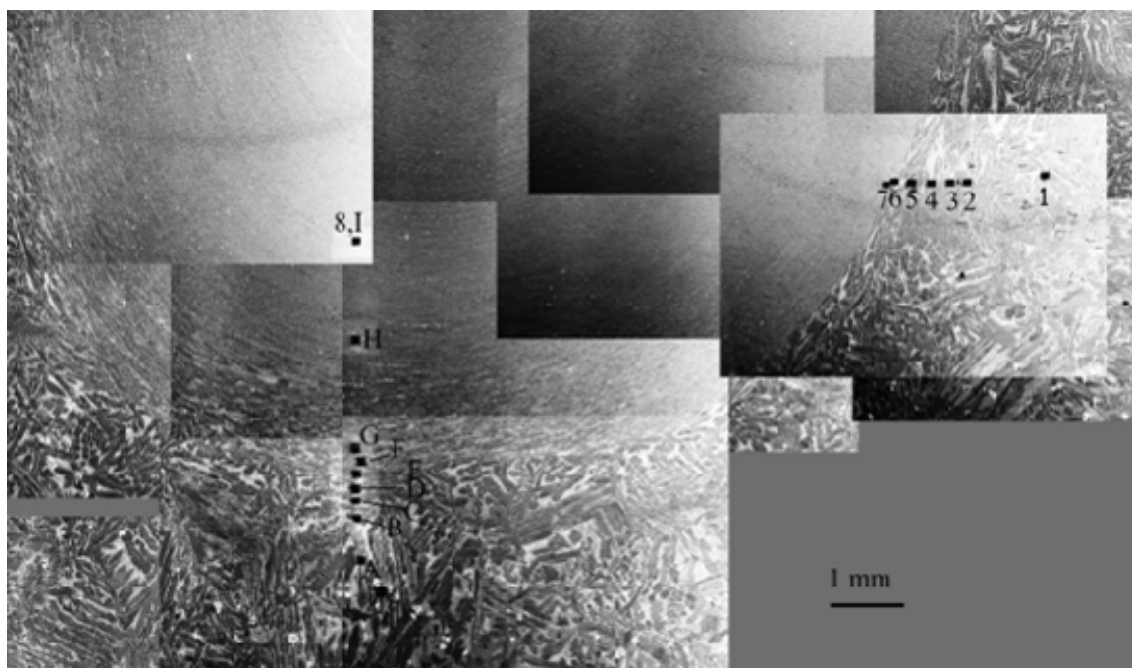


Figure 12. Single-pass sample SEM compilation showing black carbon deposits in scan locations.

Figure 12 is a montage of SEM scans taken after the OIM data was collected. In the data collection process a residue is left behind creating a darker spot. These spots are labeled for location reference later. Figure 13 is a sketch of the entire sample with the data collection locations. This graph shows the locations of the scans relative to the edges of the sample and the depth into the stir zone. The blue dotted line represents the edge of the stir zone; however, the data collection sites with respect to the stir zone border can be seen easier in the SEM scan (Figure 12).

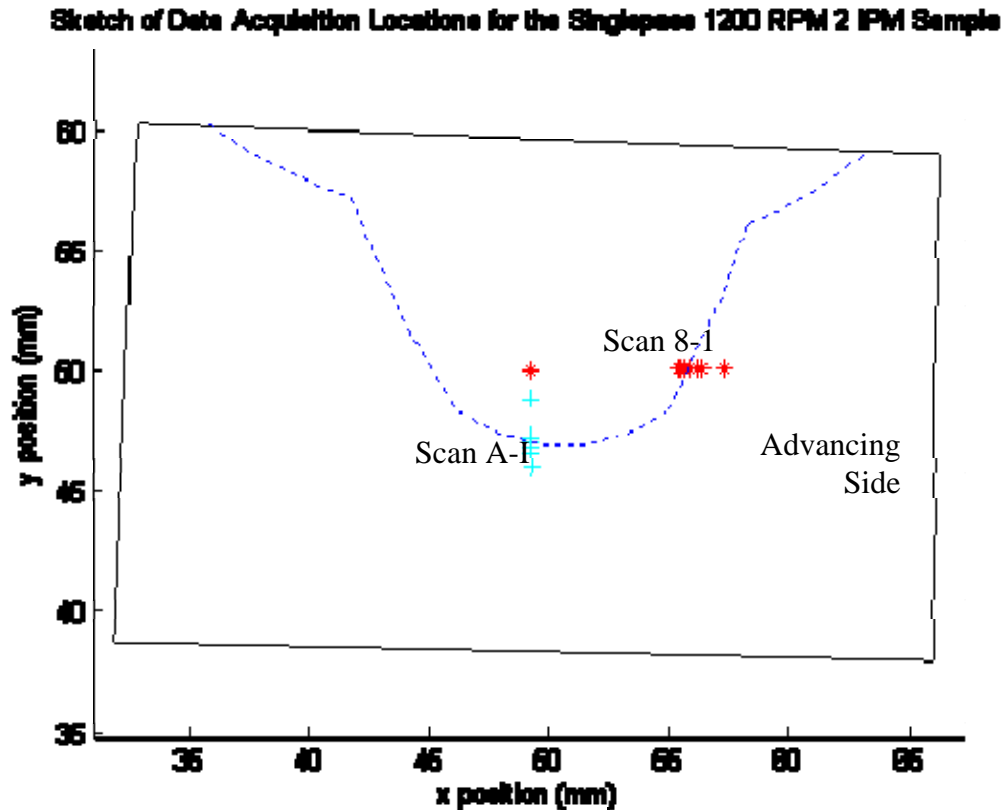


Figure 13. Sketch of Data Acquisition Locations for the Single-Pass 1200 RPM 2 IPM Sample. The sample is outlined in black with the stir zone roughly estimated with a blue dotted line. The red \*'s and light blue +'s represent locations that data was taken. The scans are numbered in order from the farthest outside the stir zone to the farthest inside the stir zone. Scan 8 will be considered with the analysis of the stir zone for the vertical centerline and will be referred to as scan I.

For the multi-pass sample, there were a total of eighteen positions in the SZ, TMAZ, and HAZ where orientation data was collected. These positions can be seen in Figure 14 and 15. Data was taken in a horizontal and a vertical line that incorporates the edge of the stir zone. The horizontal line was extended into the stir zone to incorporate material that has seen more than one pass of the tool.

Figure 14 is a montage of SEM scans taken after the OIM data was collected. This figure shows the locations of data collected close to the stir zone border. These spots are labeled for location reference later on. Figure 15 is a sketch of the entire sample with the data collection locations also labeled for ease of reference later. This

graph shows the locations of the scans relative to the edges of the sample and the depth into the stir zone. The blue dotted lines represent the edge of the stir zone with the last three passes of the tool. It is clear that scan 13 has seen two passes of the tool and scans 10, 11, and 12 were on the edge of the stir zone before the last pass of the tool.

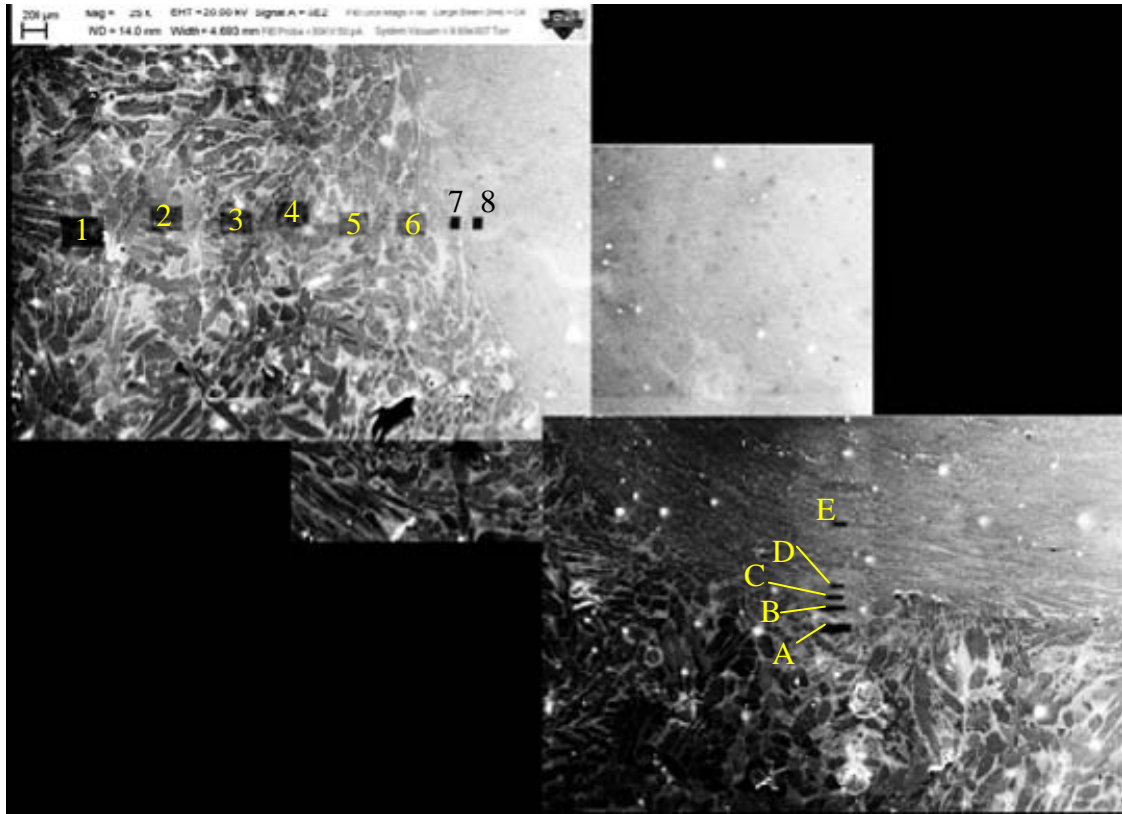


Figure 14. Multi-pass 1200 RPM 2 IPM SEM image of grain structure around Scans 1-8 and A-E.

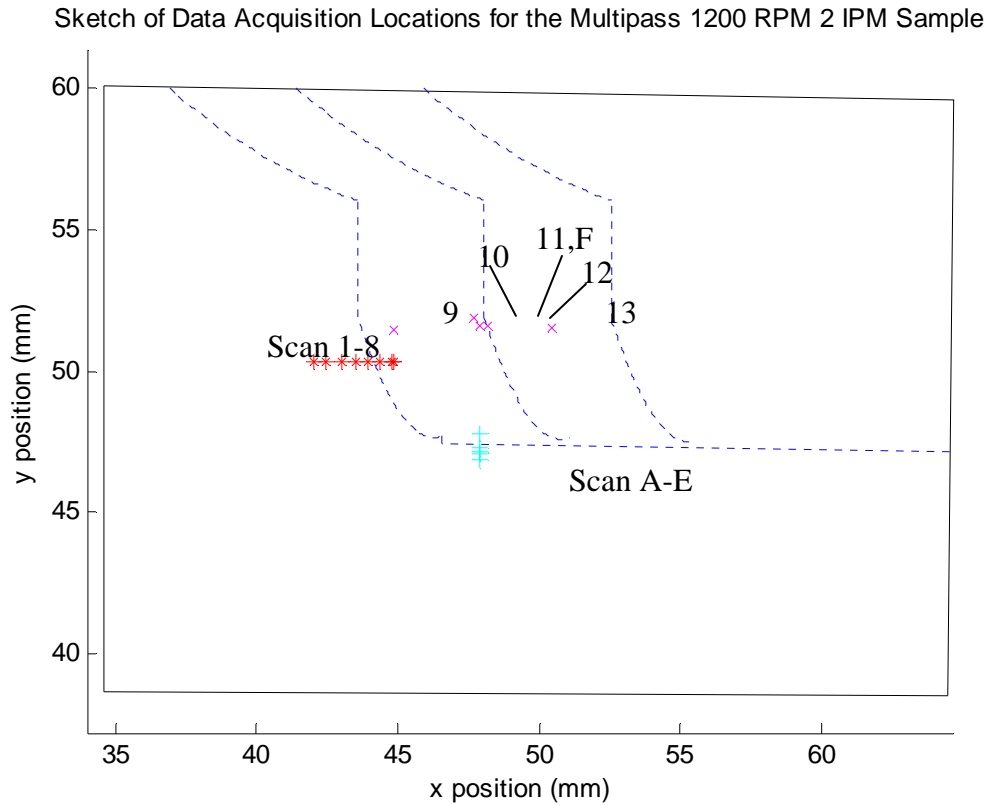


Figure 15. Sketch of Data Acquisition Locations for the Multi-pass 1200 RPM 2 IPM Sample. The Black lines represent the edge of the cut out sample. The blue dotted lines roughly represent the edge of the stir zone as the tool traveled through the material during the last three passes. The red \*'s, purple x's, and light blue +'s represent locations that data was taken. The scans are numbered in order from the farthest outside the stir zone to the farthest inside the stir zone. Scan 11 will be considered with the analysis of the stir zone for the vertical centerline and will be referred to as scan F.

## **IV. RESULTS AND DISCUSSION**

### **A. OVERVIEW**

Two samples that had undergone FSP at 1200 RPM and 2 IPM were studied in detail. One sample had seen a single-pass of the tool while the other saw multiple passes of the tool in a rectangular spiral pattern. Using OIM the grain structure and orientation are studied to help understand the mechanism(s) of deformation responsible for the SZ microstructure created during FSP of NAB. Some as-cast NAB was also looked at for a starting point to the friction stir process.

There is information from previous studies of FSP such as the primary  $\alpha$  grain structure is refined in the stir zone, the porosity of the material is eliminated in the stir zone, and there are elongated  $\alpha$  grains in the TMAZ. The data discussed in this chapter supports these observations along with giving more detail about them.

### **B. INVERSE POLE FIGURES AND IMAGE QUALITY MAPS**

In this section, Inverse Pole Figures (IPF) and Image Quality (IQ) maps will be examined at key locations in both the single and multi-pass samples. These plots will be used to draw conclusions about orientation and grain structure.

IPF uses a color-coded map to plot the location and orientation. It uses dark blue to represent crystals with their  $\langle 111 \rangle$  axis normal to the surface. Red is used to represent crystals with their  $\langle 001 \rangle$  axis normal to the surface. And, green is used to represent the  $\langle 101 \rangle$  axis normal to the surface. For any orientation in between the three orientations, the color is a combination of red, blue, and green depending on how close the orientation is to the color defined orientations. Below is a representative crystal structure with orientation axis for the FCC  $\alpha$  phase.

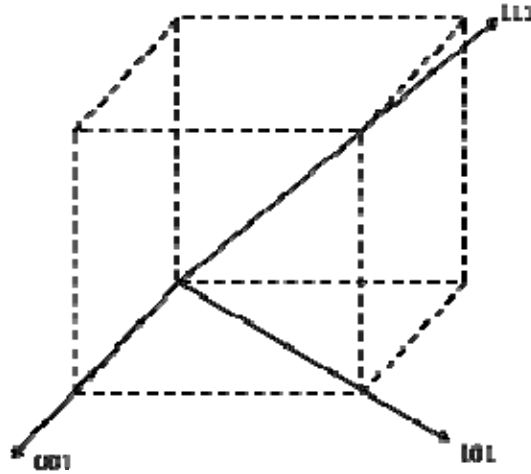
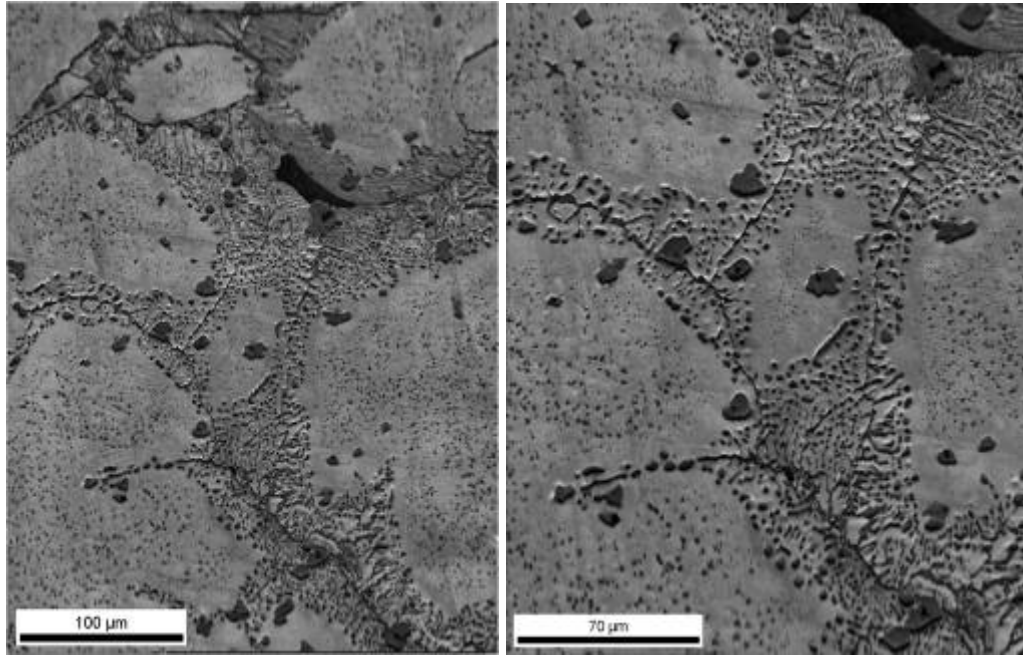


Figure 16. Representative FCC crystal structure with orientation axis.

Along with orientation data, image quality data was taken at each location. IQ represents how easily the crystal orientation was to define and had a range from 0 to around 3000 for each scan location. For each scan a grey scale plot or IQ map can be made for visualization. An IQ of zero is plotted in black and the higher the number the lighter the grey becomes. The higher the IQ value, the closer the data recorded is to an easily defined orientation. Along grain boundaries or locations where orientation changes, the regions that are next to one another are not in the same crystalline orientation which makes the orientation more difficult to define. If the data could not be identified with any orientation the IQ would be zero.

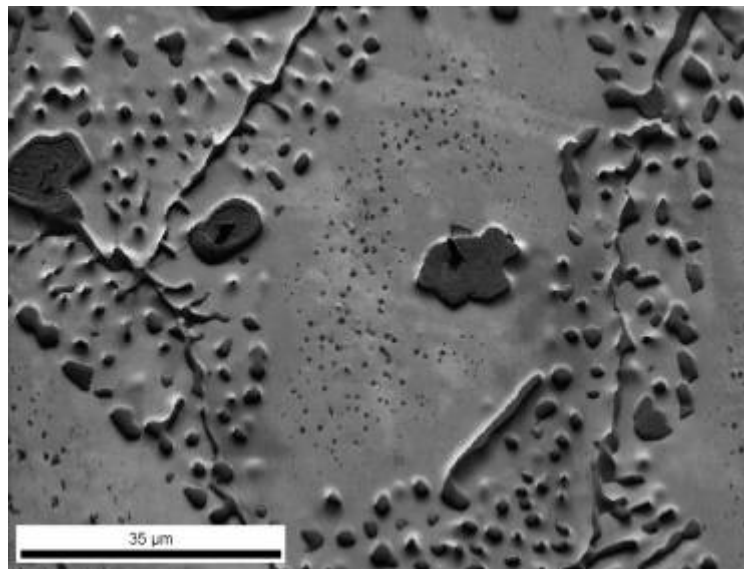
### 1. Base Material

Figure 17 shows three IQ maps of as-cast NAB from the same location but different magnifications. These IQ maps of base NAB show a mixture of large coarse primary  $\alpha$  grains with diameters greater than 50 less than 150  $\mu\text{m}$  and the  $(\alpha + \kappa_{\text{iii}})$  eutectoid regions. Fine  $\kappa_{\text{iv}}$  precipitates can be seen within the  $\alpha$  phase also. Both the  $\alpha$  and  $\kappa$  phases are plotted. These images look similar to previous images taken by conventional SEM and optical microscopy [4, 2, and 7]. No new information is gained from the as-cast NAB images, but this provides a good basis to start when analyzing the grain structure from base material to the stir zone.



(a)

(b)



(c)

Figure 17. Image quality maps of as cast material in three different scales.



## 2. Single-Pass

Figure 18 shows representative IQ maps for the  $\alpha$  phase of the as-cast material and the single-pass sample heat affected zone (HAZ), thermo-mechanically affected zone (TMAZ), and stir zone (SZ). The black areas are where  $\kappa$  phase data was removed. By comparing Figure 18 (a) to (b), the grain structure does not change much between the as-cast material to the heat affected zone for a single-pass. The grains remain large with  $\kappa$  phases in the grains and along the grain boundaries. However, there may be some coarsening of the  $\kappa_{IV}$ .

In Figure 18 (c) there is still the resemblance of a large grain in the TMAZ but now these primary  $\alpha$  grains seem to be composed of many small grains. Also, in between the large grains, there are some smaller grains mixed in with the  $\kappa$  phases. These small grains are the about the same size as the as the ones within the larger grain.

In Figure 18 (d) there is no resemblance of any large grains left in the SZ. Within the stir zone there are only small grains with the  $\kappa$  phase in between. There are no large collections of the  $\kappa$  phase left. It is dispersed evenly between all the grains.

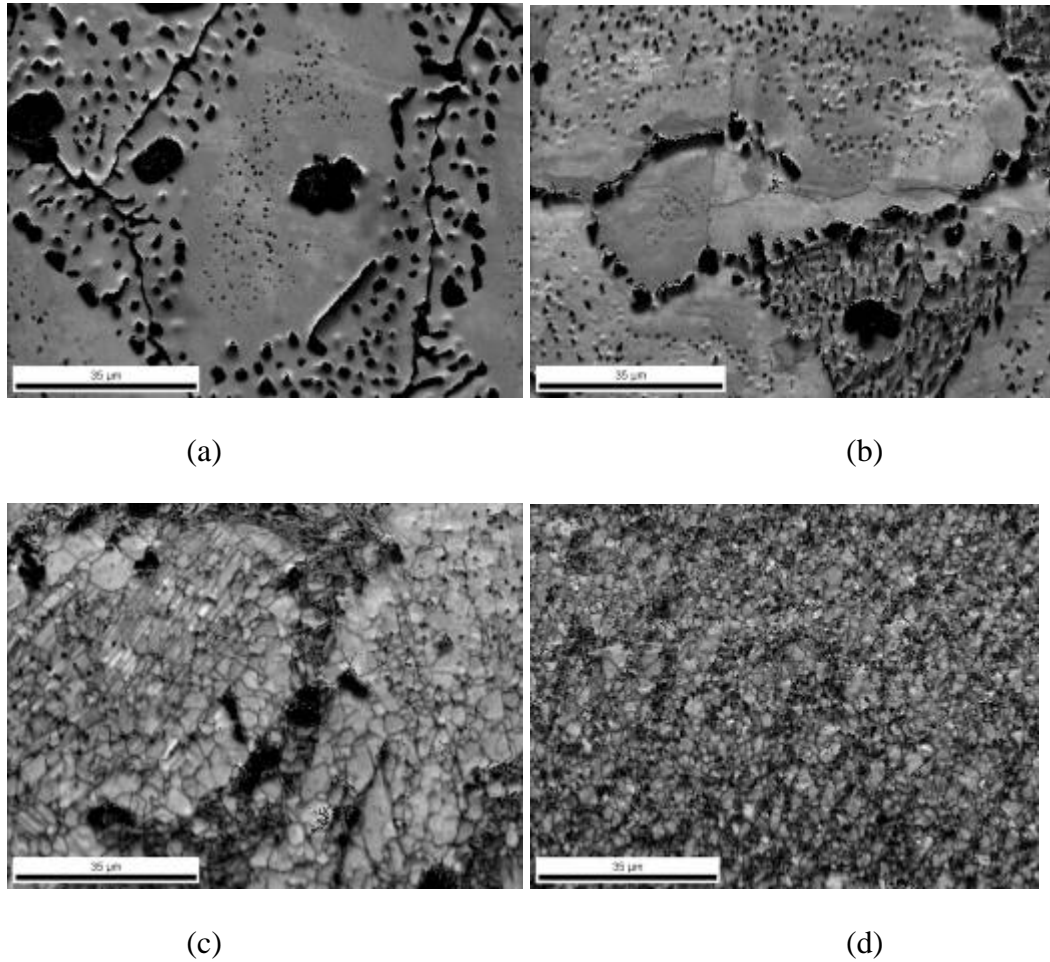


Figure 18. Representative comparison of Single-Pass image quality maps from (a) As Cast (b) HAZ (c) TMAZ (d) Stir Zone.

To make sure that the large looking grain structures are one grain and not many small ones the orientation within the grain should be the same. This can be seen in an IPF. Figure 19 contains representative IPFs for the IQ maps in Figure 18. The black spots represent data for the  $\kappa$  phase. Each color represents a different orientation. The colors give the visualization of grains. However, every time there is a change in color there is not a different grain. Inside a grain a 60-degree shift in orientation represents an annealing twin (this will be discussed further in the misorientation section).

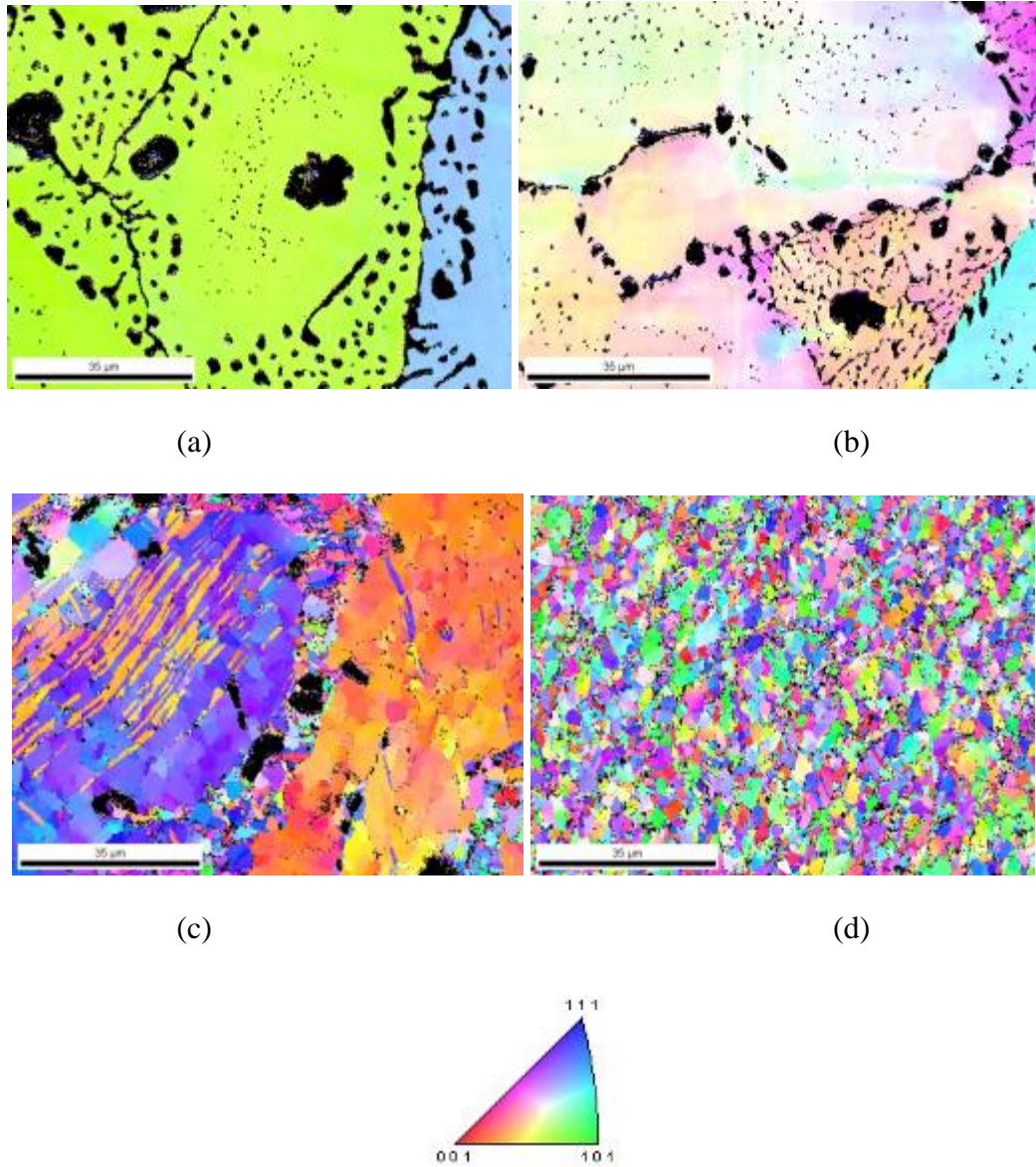


Figure 19. Representative comparison of Single-Pass IPF from (a) As Cast (b) HAZ (c) TMAZ (d) Stir Zone.

In the base material, there is one color per large primary  $\alpha$  phase area (see Figure 19 (a)). This shows that the base material does in fact have a coarse grain size with a single definable orientation per primary  $\alpha$  grain. In the HAZ (Figure 19 (b)) there is a

gradual orientation change from one side of the large primary  $\alpha$  grain to the other. This change in orientation suggests the formation of low-angle boundaries in a sub grain structure within the primary  $\alpha$ .

In the TMAZ (Figure 19 (c)) the large  $\alpha$  grains have distinct shifts in orientation from one end to the other. However, unlike the smooth transitions in orientation seen in the HAZ the TMAZ shows small sharp changes in orientation within the grains. These sharp changes happen along what appears to be smaller grains or sub grains. There are lines that run through some of the grains where the orientation changes about 60-degree (orange to purple). These lines represent annealing twins. In-between the large grains there are smaller grains with random orientation. These grains are the same size as the sub grains that compose the larger grains. In the SZ (Figure 19 (d)) the small grains have different orientations from one another and look like the small grains in-between the large grains shown in the TMAZ.

From the IQ maps and the IPF for a single-pass FSP, grains go from large coarse ones with a distinct orientation in the as-cast material to small randomly oriented grains within the stir zone. In between, the grains must change orientation, separate into smaller grains, and have the  $\kappa$  phase be dispersed evenly within the SZ. While undergoing FSP the temperature is high enough that it is in a two-phase region comprised of primary  $\alpha$  and  $\beta$  [4]. Upon cooling the various  $\kappa$  phases precipitate within the  $\beta$  and the  $\alpha$  phase following the phase transformation sequences already described earlier

### **3. Multi-pass**

Figure 20 shows IQ maps for the  $\alpha$  phase of representative locations in the multi-pass HAZ, TMAZ, SZ that saw one tool traverse and SZ that saw two tool traverses. The black spots represent the data that was removed for the  $\kappa$  phases. By comparing Figure 20 (a) to Figure 18 (a), the grain structure changes little between the as-cast material and the heat affected zone for a multi-pass system. As with the single-pass, primary  $\alpha$  grains remain large in the HAZ with  $\kappa$  phases in the grains and along the grain boundaries.

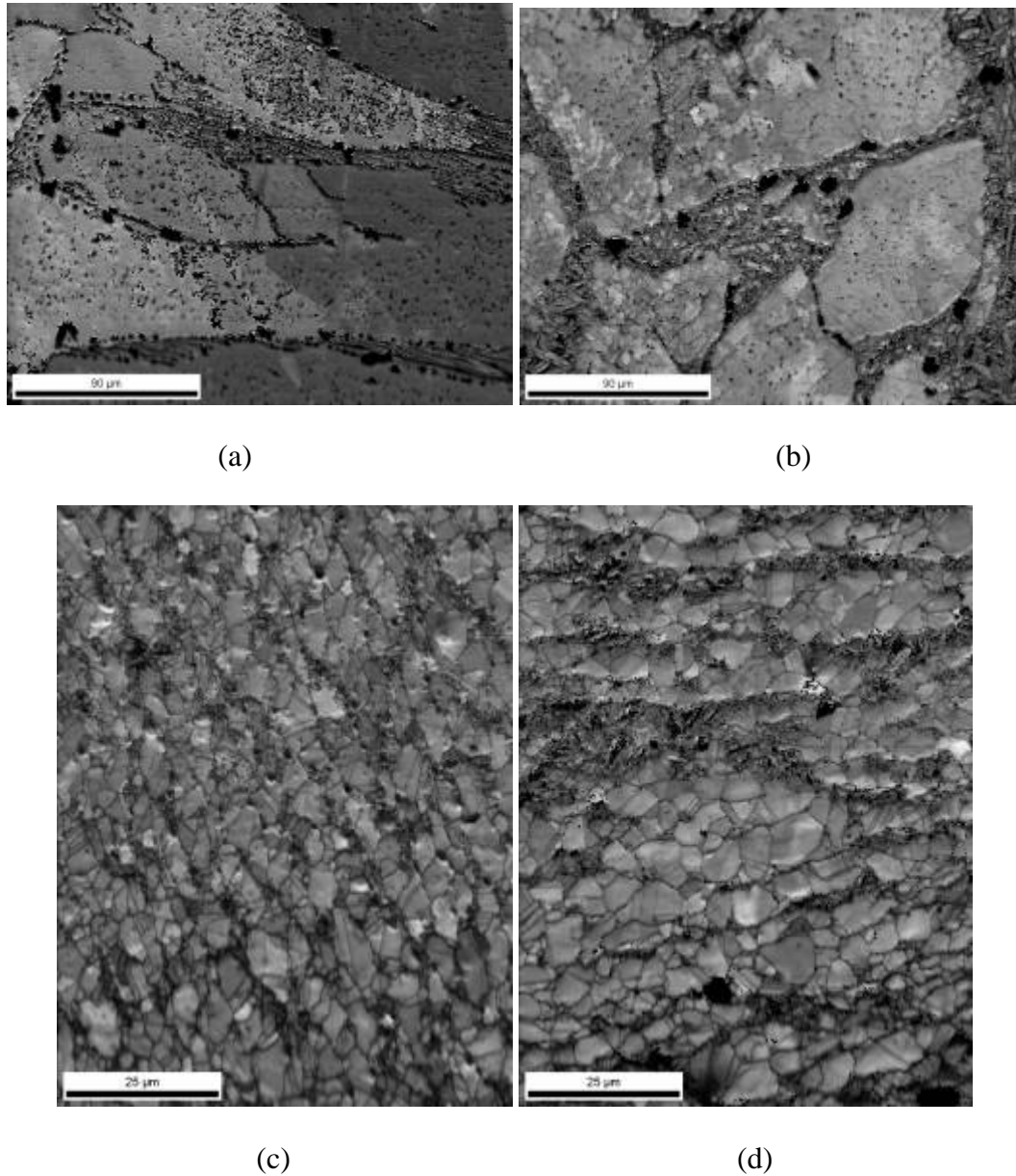
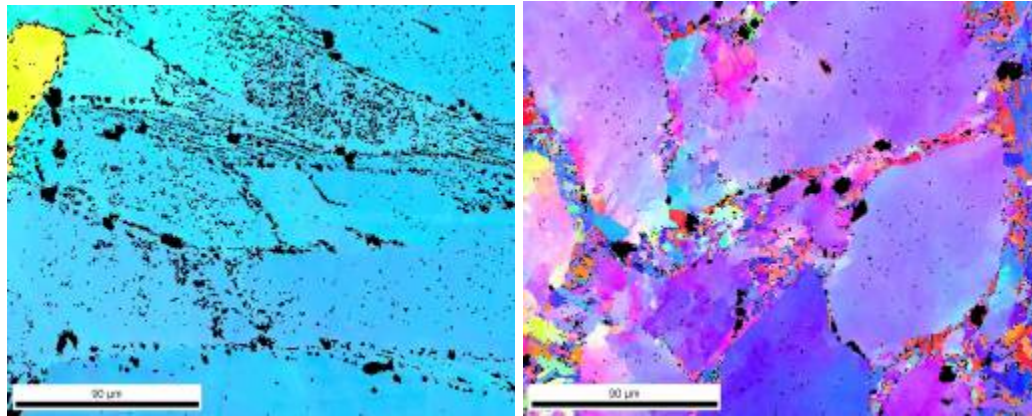


Figure 20. Representative comparison of multi-pass image quality from (a) HAZ (b) TMAZ (c) Stir Zone with one pass of tool (d) stir zone with two passes.

In Figure 20 (b), there is still a large primary  $\alpha$  grain in the TMAZ. As in the single-pass system, some of the large grains seem to be made up of smaller sub grains. In between the large grains, there are some smaller grains mixed in with the  $\kappa$  phases. These small grains are the about the same size as the as the ones that are making up the larger grain.

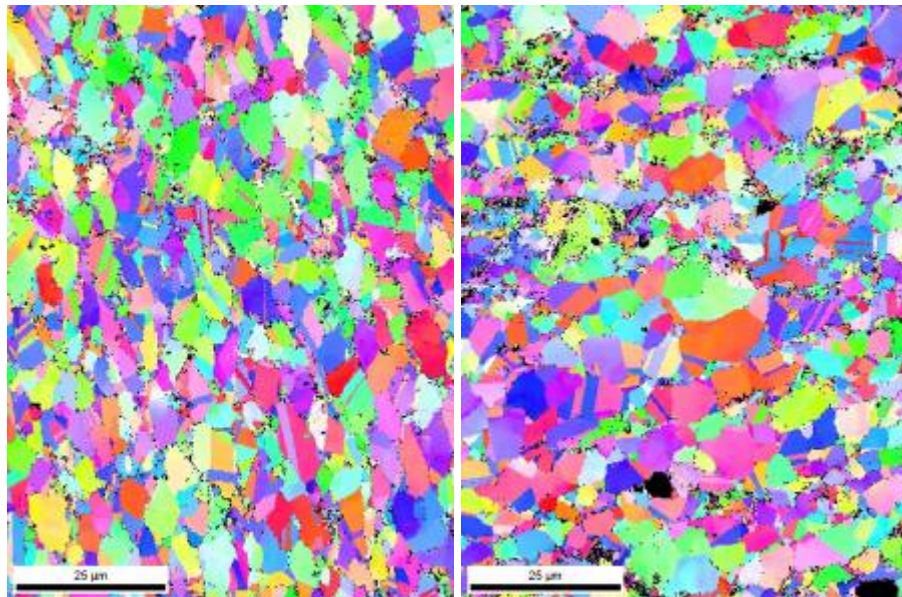
Similar to the single-pass sample, seeing the tool one time leaves the grain structure in the SZ looking like there are no large grains remaining (Figure 20 (c)). Within the stir zone, there are only small grains with the  $\kappa$  phase in between. There are no large  $\kappa$  phases remaining as well and they are dispersed evenly between all the grains. Seeing the tool a second time, in the stir zone (Figure 20 (d)), results in slightly coarse  $\alpha$  grains.





(a)

(b)



(c)

(d)

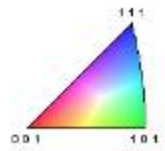


Figure 21. Representative comparison of multi-pass IPF from (a) HAZ (b) TMAZ (c) Stir Zone with one pass of tool (d) stir zone with two passes.

As with the single-pass sample, IPFs will be used to assess the orientation within the grains. In the base material, there is one color per large  $\alpha$  phase area (see Figure 19 (a)). This shows that the base material does in fact have a coarse texture with a single definable orientation per grain. In the multi-pass HAZ (Figure 21 (a)) there is a slow orientation change (different shades of blue) from one side of the large  $\alpha$  phase formation to the other. This change in orientation is within the tolerance to identify these formations large  $\alpha$  phase grains. The change in orientation across a grain the HAZ for multi-pass is less than it is for single-pass.

In the TMAZ (Figure 21 (b)) the large grain-like structures have small shifts in orientation from one end to the other. However, unlike the smooth transitions in orientation seen in the HAZ the some of the grains in the TMAZ shows small, sharp changes in orientation within the grain boundaries. These sharp changes happen along what looks like smaller grains or sub grains. In between the large grains there are smaller grains of random orientation. These grains are the same size as the sub grains that compose the larger grains. In the SZ (Figure 21 (c) and (d)) the small grains have different orientations from one another and look like the small grains in-between the large grains shown in the TMAZ. Seeing the tool a second time does not change the randomness of the orientation of the grains in the SZ.

From the IQ maps and the IPF for a multi-pass FSP, grains go from large, coarse ones with distinct orientation in the as-cast material to small randomly oriented grains within the stir zone. In between, the grains must change orientation, separate into smaller grains, and have the  $\kappa$  phase be dispersed evenly within the SZ. While undergoing FSP the temperature is high enough that it is a two-phase system  $\alpha$  and  $\beta$  [E]. Upon cooling the  $\beta$  phase and some  $\alpha$  phase turns into bainite. In order for the  $\kappa$  phase to be dispersed evenly after cooling, the  $\beta$  phase must be evenly dispersed during the processing.

### **C. MISORIENTATION ANGLES**

The IPF images seen in the previous section give a visual representation of orientations for each scan. From the IPF maps, it is easy to see relative grain sizes, twins, and grain boundaries. Grains are created to have the lowest possible boundary energy.



This gives rise to grains with smooth, round boundaries. In many cases, triple junctions exhibit 120-degree boundary angles. However, in some IPF there are long, thin rectangular features (see Figure 22). These features are annealing twins. Annealing twins are formed as a consequence of growth accidents during recrystallization of deformed FCC metals such as alpha-brass, copper, nickel, and austenitic iron [10]. The lattice in the twin is rotated by 60-degree about a  $\langle 111 \rangle$  axis related to the surrounding parent lattice.

It could be expected that during the FSP there is sufficient stress to form mechanical twins. Mechanical twins tend to be lenticular i.e., lens-shaped with sharp edges [10]. Annealing twins are not pointed since there is no deformation associated with their formation [10]. What are seen in Figure 22 are straight lines with no points to them. Thus, these twins are annealing twins and not mechanical twins.

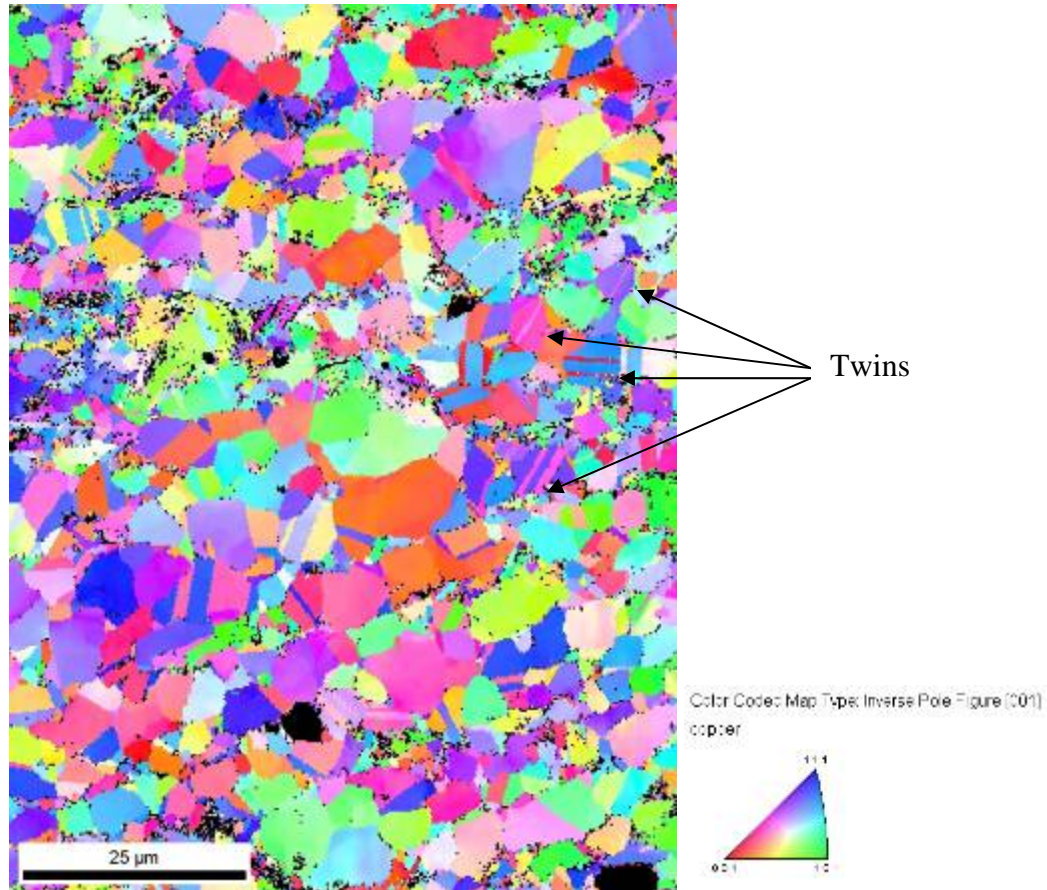


Figure 22. Representative Inverse Pole Figure from inside a multi-pass stir Zone showing annealing twins and a refined grain structure. The black spots represent the  $\kappa$  phases.

Since IPF give a visual representation of the orientation change but not a quantitative measure, misorientation angle data were extracted. Misorientation angle is the difference in orientation between two adjacent sub sections of the crystalline material. To be able to compare the data from one scan to another, the number of points with a given misorientation angle was divided by the total number of extracted points to give the number fraction at each misorientation angle. If the misorientation angle was zero, the two points were considered to be part of the same grain. Data from the same grain was not extracted for use in the misorientation number fraction calculations. The data left for use in the number fraction calculation came from locations where orientation changed. Since most of the time when orientation changes it is a grain boundary, this number fraction calculated will be called the ‘number fraction of grain boundary misorientation angles’. All extracted data can be seen in the Appendixes.

These number fractions can be plotted versus the misorientation angle to give a relative view of large-angle and small-angle grain boundaries. Figure 23 is a sample plot inside the multi-pass SZ that has seen only one pass of the tool. From the IPF in Figure 22, there are annealing twins located inside some of the grains. The peak at 60 degrees in Figure 23 is due to annealing twins. Other than the peak for annealing twins, an indication that there is random orientation is relatively constant number fractions at each angle. This will be assessed later by analysis of the corresponding pole figure data.

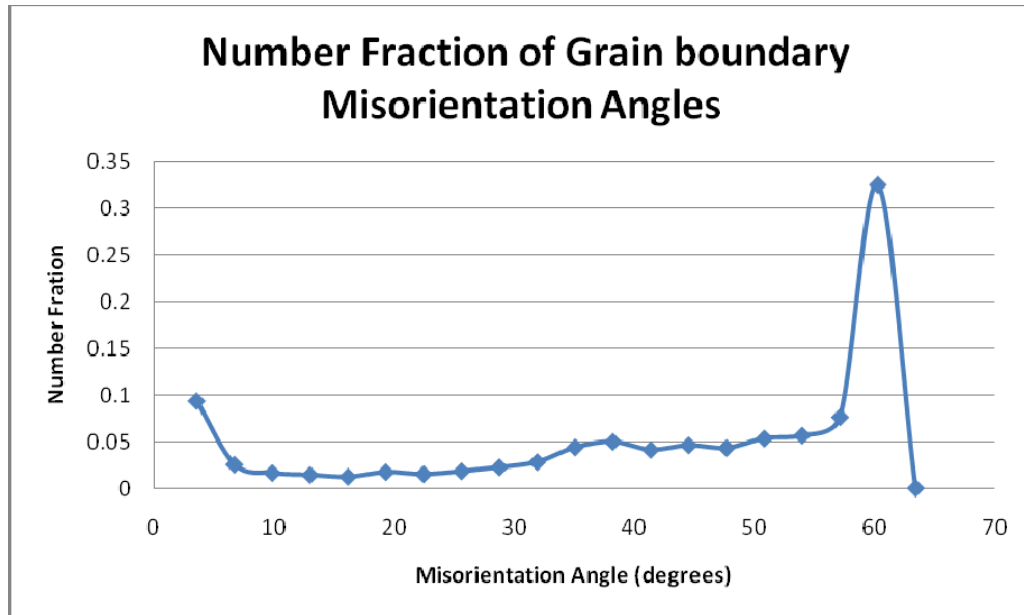
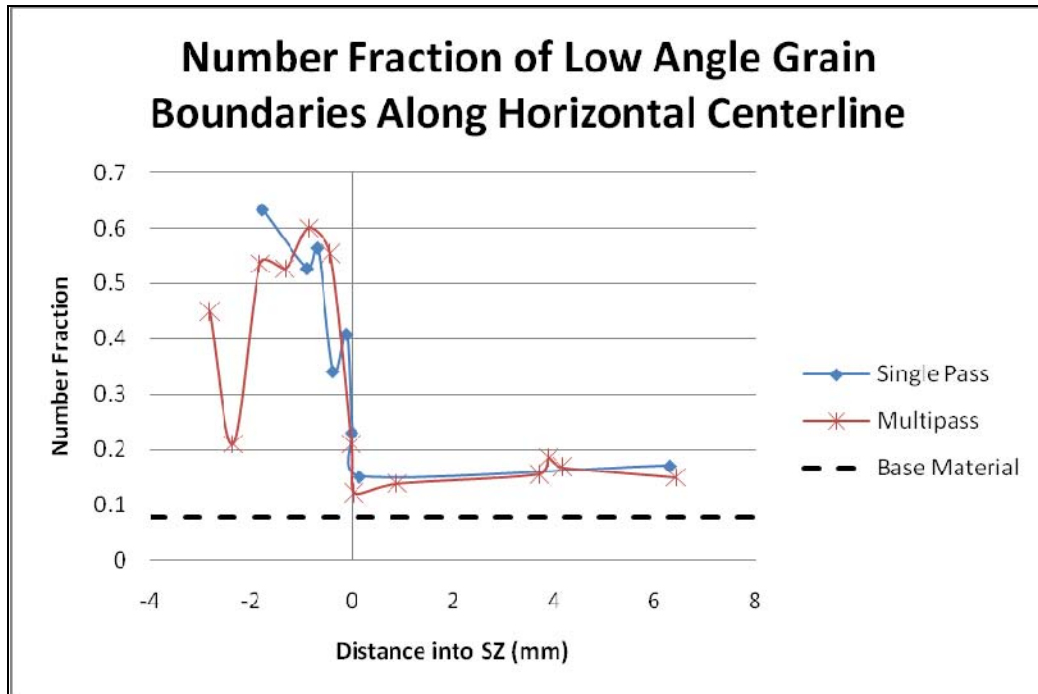


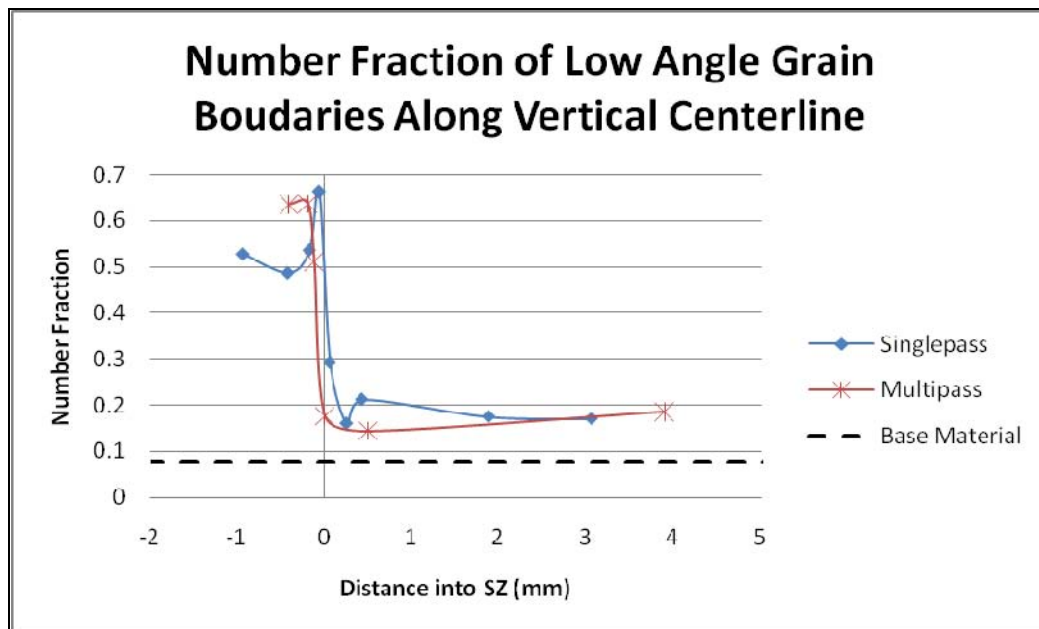
Figure 23. Representative misorientation graph. The Number Fraction of Grain Boundary Misorientation Angles for multipass scan 8.

If there were a large number fraction of low angle boundaries, less than 15 degrees, then it would show that there is residual strain from prior deformation. From all of the scan locations for both multi-pass and single-pass the number fraction of low angle boundaries was extracted. This data is plotted in Figure 24 (a) and (b) and compared to the base material. Figure 24 (a) shows the number fraction of low angle grain boundaries from outside the SZ moving into the SZ along a horizontal line for both the single-pass and the multi-pass scans. This data was taken from the scans 1-8 for single-pass and scans 1-13 for the multi-pass. The black dotted line is the number fraction of low angle grain boundaries from the base material to give a comparison point. The vertical line at zero represents the TMAZ-SZ interface.

Figure 24 (b) shows the number fraction of low angle grain boundaries from outside the SZ moving into the SZ along a vertical line for both the single-pass and the multi-pass scans. This data was taken from the scans A-I for single-pass and scans A-F for the multi-pass. The black dotted line is the number fraction of low angle grain boundaries from the base material to give a comparison point. The vertical line at zero again represents TMAZ-SZ interface.



(a)



(b)

Figure 24. Number Fraction of Low angle Grain boundaries (a) for single and multipass along horizontal centerline (b) for single and multipass along vertical centerline.

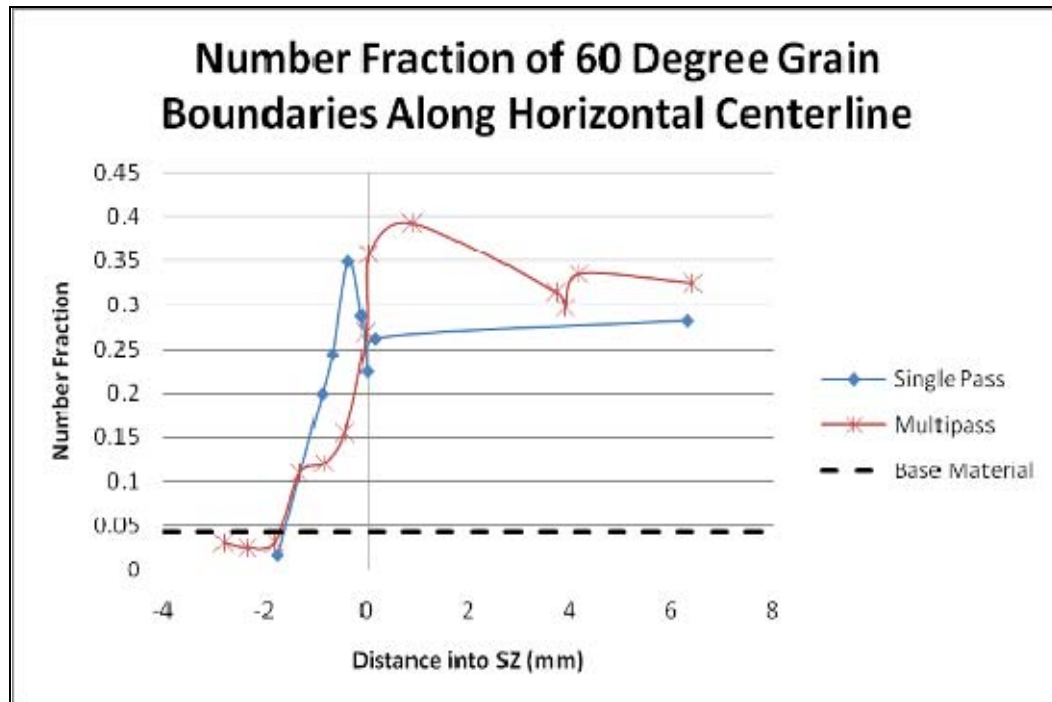
From Figure 24, it can be seen that there is a trend followed by both single-pass and multi-pass material. Moving from the HAZ to the stir zone, the number fraction of low-angle grain boundaries drops through the TMAZ. Inside the stir zone there is no preferred orientation.

Since there are not many small angle boundaries in the SZ than it can be concluded that there must be a large portion of higher angle grain boundaries. However, the data that would be used to extract the large angle grain boundaries also include the data for annealing twins. The number fraction of 60 degree ‘grain boundaries’ were plotted for all of the data in Figure 25 (a) and (b).

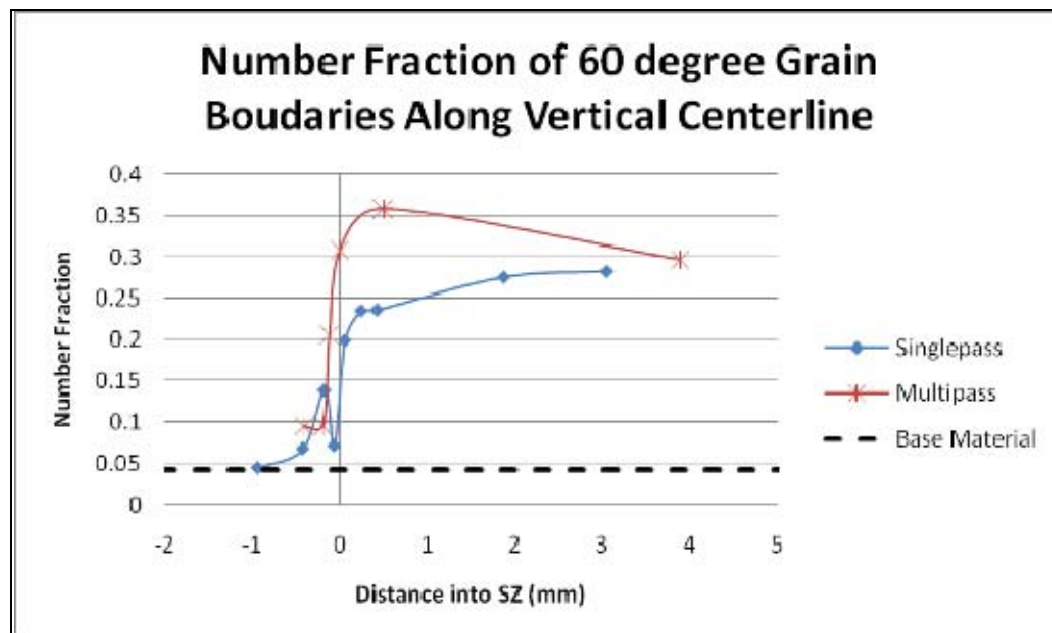
Figure 25 (a) shows the number fraction of 60-degree angle grain boundaries from HAZ moving into the SZ along a horizontal line for both the single-pass and the multi-pass scans. This data was taken from the scans 1-8 for single-pass and scans 1-13 for the multi-pass. The black dotted line is the number fraction of 60-degree grain boundaries from the base material to give a comparison point. The vertical line at zero represents the TMAZ-SZ interface.

Figure 25 (b) shows the number fraction of 60-degree grain boundaries from the HAZ moving into the SZ along a vertical line for both the single-pass and the multi-pass scans. These data were taken from the scans A-I for single-pass and scans A-F for the multi-pass. The black dotted line is the number fraction of 60-degree grain boundaries from the base material to give a comparison point.

These plots show a trend that is similar for both multipass and single-pass looking from the base material into the stir zone. From the base material to the HAZ there is almost no change in the number fraction of 60 degree grain boundaries; however, as you get into the TMAZ the number fraction of 60 degree grain boundaries starts to rise until starts to level out inside the SZ.



(a)



(b)

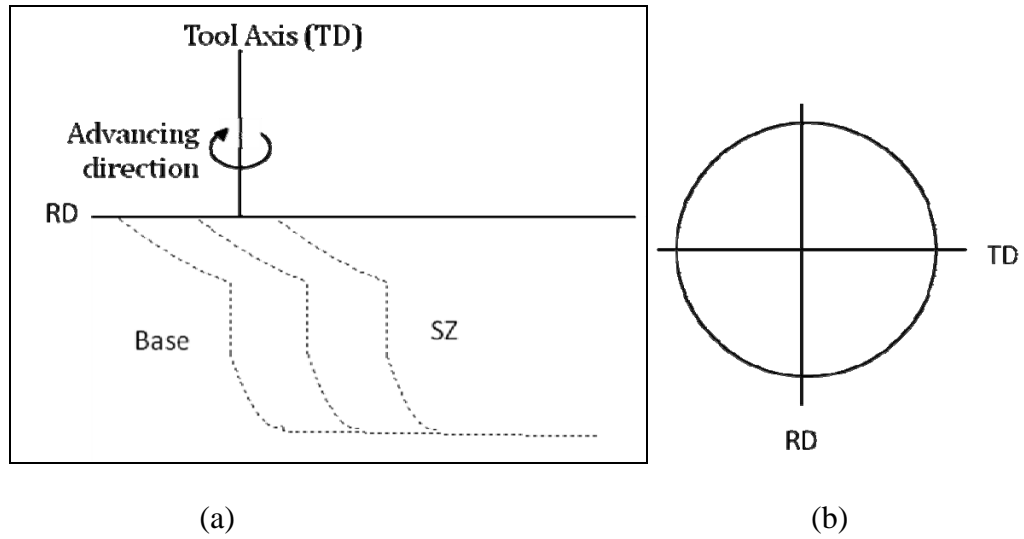
Figure 25. Number fraction of 60 degree Grain boundary misorientation (a) for single and multipass along horizontal centerline (b) for single and multipass along vertical centerline.

#### **D. TEXTURE**

Texture refers to the distribution of orientation within a poly-crystalline structure. If there is a fully random orientation within the poly-crystalline structure the material is said to have no texture. As there becomes a more preferred orientation than the material has a texture. The type of texture ranges from weak to strong depending on how narrowly the orientation is distributed. One way to look at the texture of a sample is through pole figures.

Pole figures are stereographic projections that are used to represent the orientation distribution of a poly-crystalline structure. Each black dot in a pole figure represents a data point from the scan. It is typical to measure or plot three pole figures with respect to the three lowest Miller indices since a single pole figure does not uniquely determine the orientation(s) [11]. This is because only the plane normal to the Miller index is measured. If the pole figure has the same intensity in all directions than the sample has a random texture. If there is a high intensity than there is a preferred orientation. For the purposes of representing pole figures in this study, the intensity of the orientation was calculated with a Harmonic Series Expansion with Gaussian smoothing of  $5^\circ$ .

Orientation of the FSP samples used in this study is shown in Figure 26(a) along with the reference axis directions in the pole figures in Figure 26 (b). ND refers to the FSP tool traverse direction which is the direction into Figure 26(a). TD is the axis of FSP tool rotation and RD is the radial direction of the FSP tool. The RD and TD axis are plotted on all the pole figures that follow.



TD=Axis of Tool Rotation

RD = Radial Direction of Tool

Figure 26. (a) Sketch of transverse section of FSP multi-pass sample with (b) pole figure axis defined.

The tool geometry and the spiral feature on the tool surface will cause the direction of the shear stresses experienced in the samples to be at an angle. Figure 27 shows a pole figure for as-cast material. From the earlier IPF of the as-cast material, the sample had two grain orientations one per grain. The pole figures also show there are one main orientation and a second, less intense orientation. The intensity is shown in the color coded pole figure on the right. This pole figures shows that before friction stir processing there is a single orientation and the feature is a large grain.



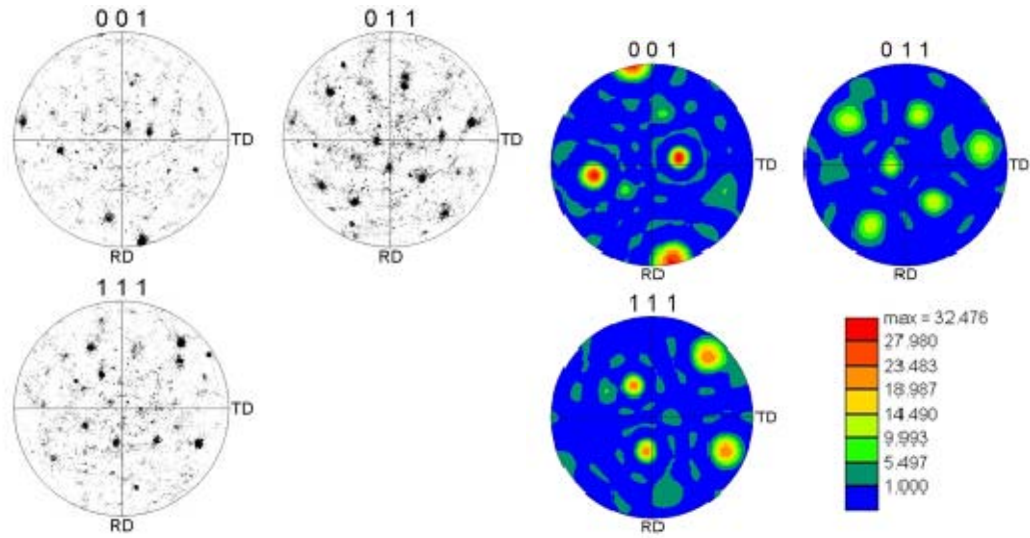


Figure 27. Representative as-cast pole figure with texture pole.

To assess the texture created by FSP, representative pole figures will be examined for both the single-pass and the multi-pass sample. Since there is likely to be shearing during FSP these pole figures will be compared to the three shear fibers A, B, and C [18]. Shear fiber A has a preferred orientation in any  $\langle uvw \rangle$  direction in the  $\{111\}$  plane [18]. Shear fiber B has a preferred orientation in  $\langle 110 \rangle$  direction in any  $\{hkl\}$  plane [18]. Shear fiber C has a preferred orientation in the  $\langle 110 \rangle$  direction in the  $\{100\}$  plane [18]. There,  $\{hkl\}$  is the lattice plane parallel to the shear plane while  $\langle uvw \rangle$  is the lattice direction parallel to the shear direction.

After the single-pass and multi-pass pole figures were obtained, the peak intensities from all the data points will be combined to assess the pattern of behavior. The pole figures from all data locations can be viewed in the appendixes.

### 1. Single-Pass Texture

Figure 28 shows a representative pole figure and its corresponding texture pole figure for the single-pass HAZ. This figure shows three locations of high intensity in the 001 pole figure. This represents a single orientation in the HAZ. There appears to be a slight spreading about an axis in the lower left quadrant.

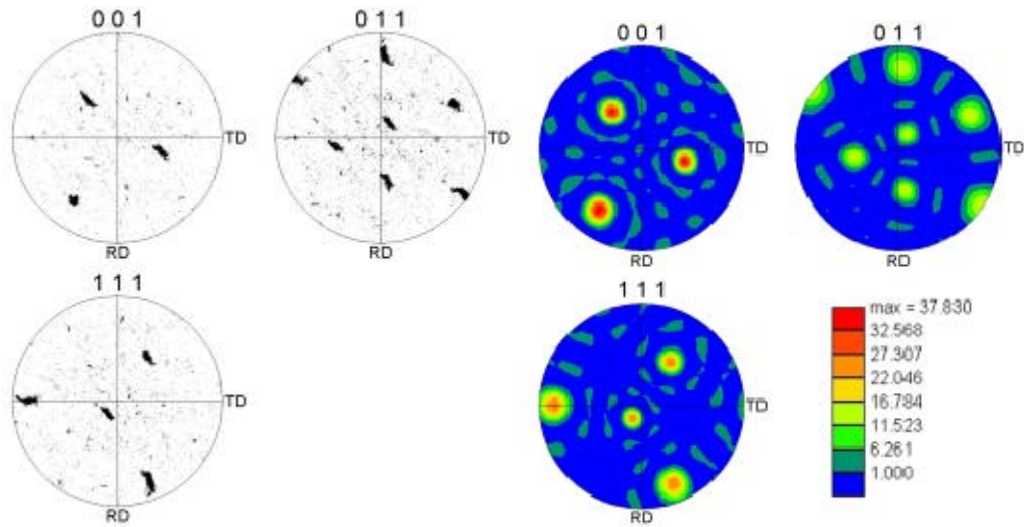


Figure 28. Representative Single-Pass HAZ pole figure with coorisponding texture pole figure. This was taken from Single-Pass scan A.

Figure 29 shows representative pole figure data for the TMAZ. This texture is consistant with a B shear fiber which is in the  $\langle 110 \rangle$  direction in any  $\{hkl\}$  plane. The apparent rotation about a  $\langle 011 \rangle$  approximatly aligned with the sample normal suggests that the B-fiber orientation is distributed about such an axis by tool rotation.

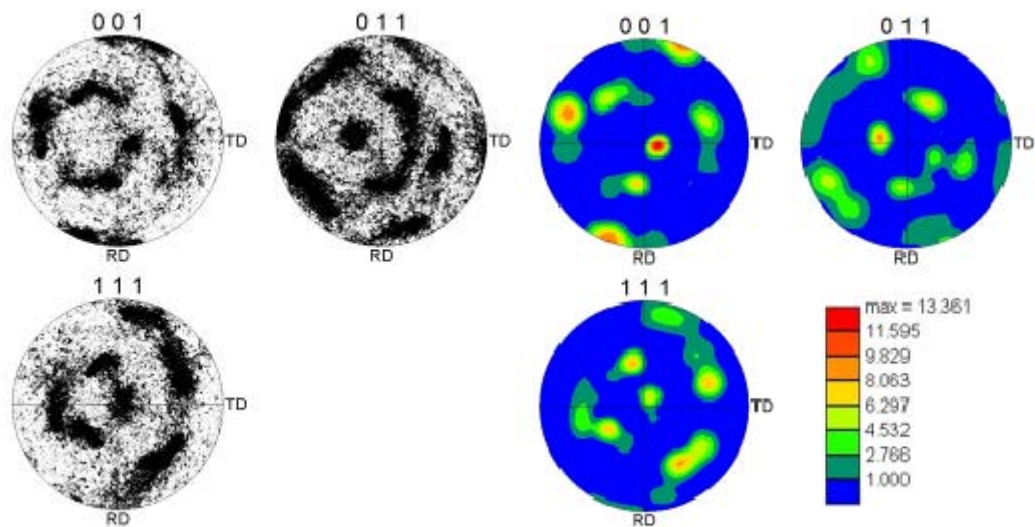


Figure 29. Representative Single-Pass TMAZ pole figure with coorisponding texture pole figure. This was taken from single-pass scan 5.

Figure 30 is representative pole figure data for the single-pass SZ. From the pole figure there is an even distribution of orientations throughout the entire plot. The intensity plot shows there is not a single direction that is more prevalent than anyother. In the SZ there is no texture and a random distribution. This confirms what was viewed from the IPF.

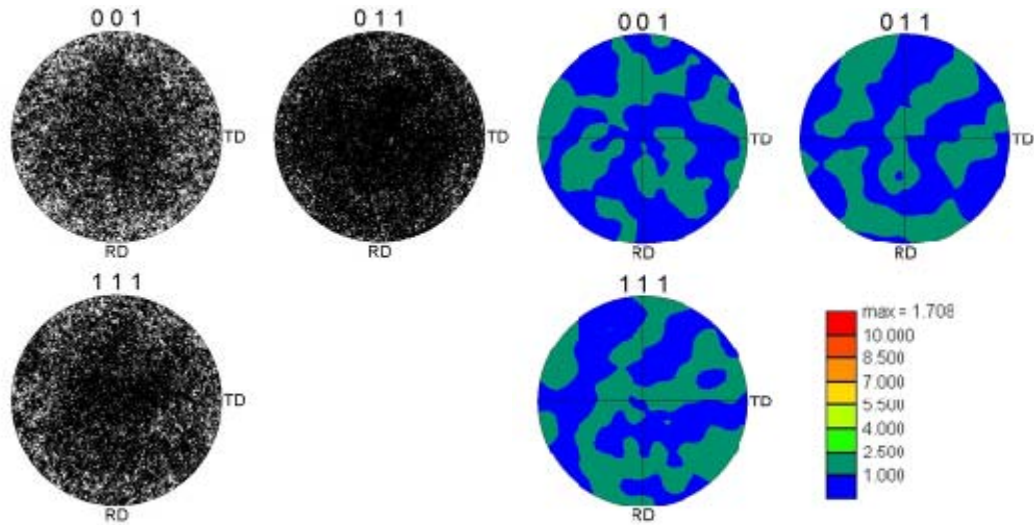


Figure 30. Representative Single-Pass Stir Zone pole figure with coorisponding texture pole figure. This was taken from single-pass scan 7.

## 2. Multipass Texture

Figure 31 shows a representative pole figure data for the multipass HAZ. This figure is similar to what was observed the single-pass HAZ. A single dominant orientation accompanied by several minor orientations in the field of view (Figure 20 a).

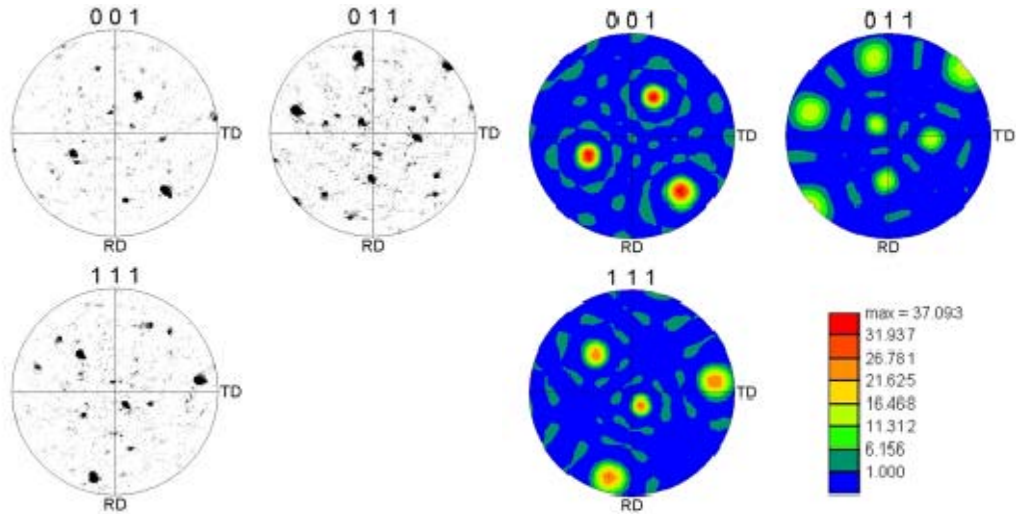


Figure 31. Representative Multipass HAZ pole figure with corresponding texture pole figure. Taken from the multipass sample scan 2.

Figure 32 shows representative pole figure data for the multipass TMAZ. There are three relatively high intensity locations in the 001 pole figure. These are present from the base material orientation. Notice that the peak intensity on the TMAZ texture pole figure is less than the peak intensity in the HAZ texture pole figure. This figure also shows a location with relatively high intensity in the 011 pole figure. Around this location there is the start of a pattern of rotation. This texture is consistent with B-type shear fiber which is in the  $\langle 110 \rangle$  direction on any  $\{hkl\}$  plane. This is similar to what was observed in the single-pass TMAZ texture pole figure (Figure 29).

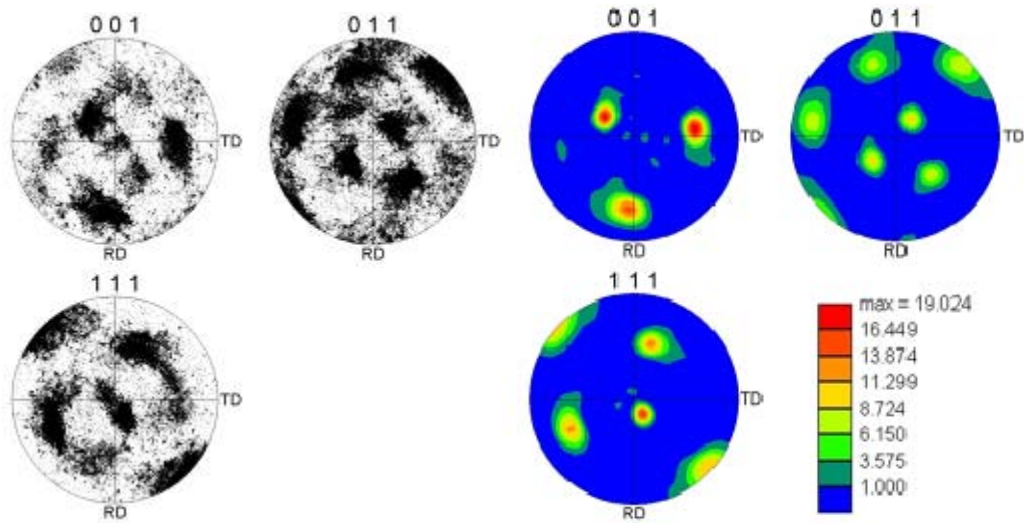


Figure 32. Representative Multipass TMAZ pole figure with coorisponding texture pole figure. Taken from the multipass sample scan scan 6.

Figure 33 is representative pole figure data for the multipass SZ. From the pole figure there is an even distribution of orientations throughout the entire plot. The intensity plot shows there is not a single direction that is more prevalant than any other. In the SZ there is no texture and a random distribution. This is similar to what was viewed in the IPF (Figure 21 (c)).

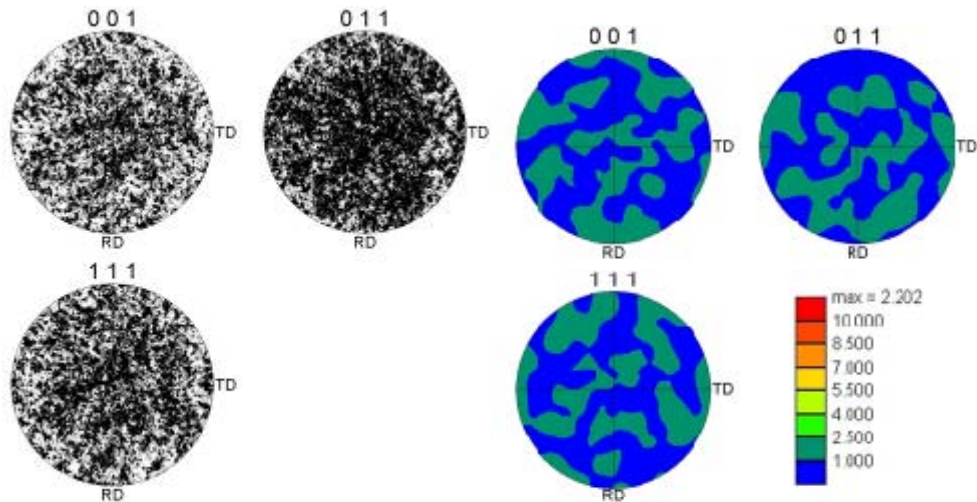


Figure 33. Representative Multipass Stir Zone pole figure with coorisponding texture pole figure. Images from multi-pass scan 11.

### 3. FSP Texture Summary

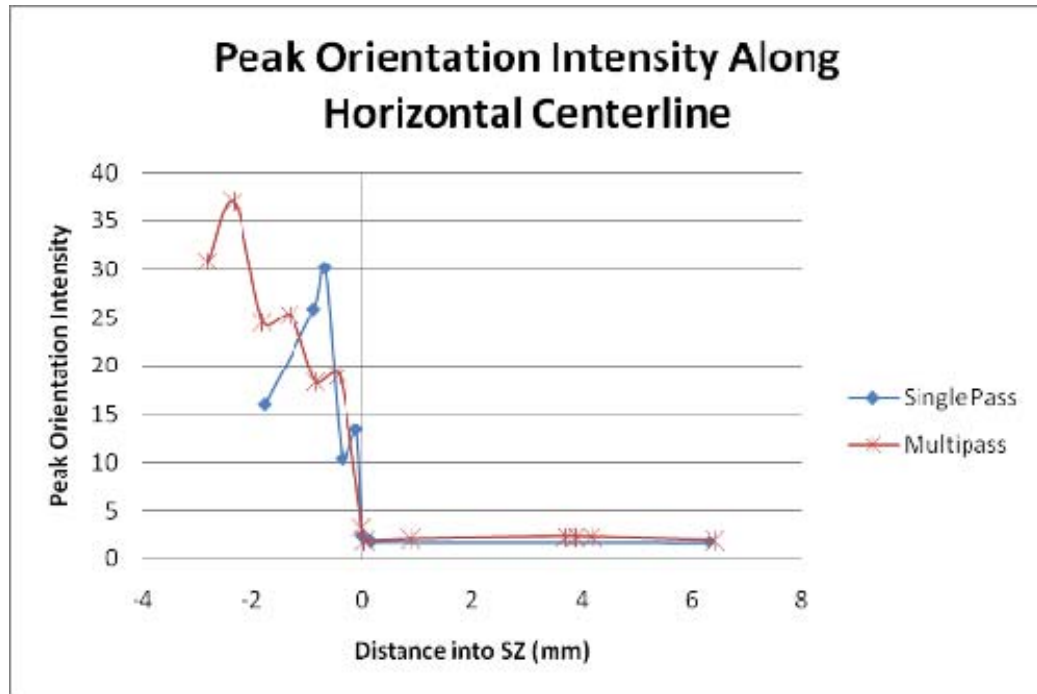
From the multipass and single-pass samples 3 similar observations were made. One, there is texture similar to the as-cast material in the HAZ. Two, in the TMAZ there is the formation of a B-type shear texture with lower peak intensities than the HAZ. Three, there is random orientation with no texture inside the stirzone. The data from all of the scan locations was combined to form Figure 34 (a) and (b).

Figure 34 (a) shows the peak intensity from the pole figures from HAZ moving into the SZ along a horizontal line for both the single-pass and the multi-pass scans. This data was taken from the scans 1-8 for single-pass and scans 1-13 for the multi-pass. The vertical line at zero represents TMAZ-SZ interface. To the right is the distance into the stir zone.

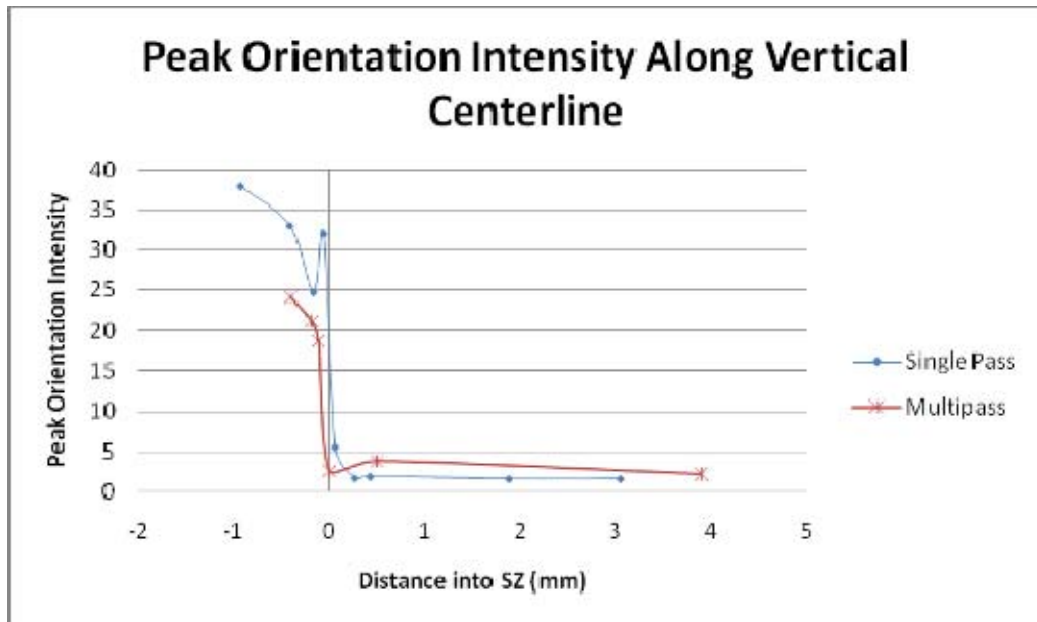
Figure 34 (b) shows the peak intensity from the pole figures from outside the SZ moving into the SZ along a vertical line for both the single-pass and the multi-pass scans. This data was taken from the scans A-I for single-pass and scans A-F for the multi-pass. The vertical line at zero represents the TMAZ-SZ interface. To the right is the distance into the stir zone.

Figure 34 shows that peak intensities drop through the TMAZ. Once the SZ is reached there is very little texture or preferred orientation inside the stir zone. These two graphs show that there is a trend of preferred orientation outside the stirzone and random orientation inside the stir zone.





(a)



(b)

Figure 34. Peak intensities given by texture pole figures for all data locations. Peak intensities over ten represent a preferred orientation or texture. (a) for single and multipass along horizontal.

## **E. PLAUSIBLE MODELS FOR FRICTION STIR PROCESSING OF NAB**

There is not yet an encompassing model for the deformation and recrystallization during FSP. Dynamic restoration and grain boundary sliding will be examined for their applicability in modeling FSP. Dynamic restoration models from hot rolling are the models currently used to classify friction stir processing recrystallization. However, multiphase systems like NAB do not fit the model as well as some other materials.

Grain boundary sliding is a possible model but from the data collected in these experiments it is not conclusive that it is the correct model either. Data acquired in this study suggests that any model must predict the formation of a shear texture in the TMAZ and its subsequent weakening into the SZ.

### **1. Dynamic Restoration**

Currently, deformation modeling in friction stir processed aluminum is done with the dynamic restoration models from hot rolling. These models have been applied to NAB in the past as well. Dynamic restoration refers to the processes that have deformation and restoration take place at the same time. Dynamic recovery, discontinuous dynamic recrystallization, geometric dynamic recrystallization and recrystallization via particle stimulated nucleation are the four main dynamic restoration types.

Dynamic recovery occurs in metals with high stacking fault energy. At moderate strains in steady state, it can be recognized by the prior grains retain their identity and change shape while dislocation and sub grain dislocation and sub-grain structures remain approximately constant. While at very large strains it can be recognized by the separation of the prior boundaries may be reduced to the sub grain size [12]. However, NAB has relatively low stacking fault energy, which is characteristic of materials that create twin boundaries in recrystallization [12].

Discontinuous dynamic recrystallization occurs in metals of low stacking fault energy. It is recognized by the new dislocation-free grains that form at sites such as prior grain boundaries, deformation band interfaces or boundaries of newly recrystallized



grains and it is accompanied with deformation textures with characteristic recrystallization textures [12]. NAB shows no texture inside the SZ so this is not plausible.

Geometric dynamic recrystallization is observed during dynamic recovery when the separations of prior grain boundaries approach sub grain size; however, the texture before deformation is retained [12]. NAB does not undergo dynamic recovery but even if it did there is no retained texture in the SZ.

Recrystallization via particle stimulated nucleation involves the formation and growth of new grains from fine cells or sub grains in the deformation zones. This deformation shows highly misoriented cells or sub grains form in zones surrounding non deforming particles. Recrystallization textures seem to be random or have weak deformation components [12]. NAB has random or weak recrystallization components inside the SZ. There is nothing that was seen in OIM to negate this as a possible recrystallization technique inside the SZ. However, in the TMAZ there is a preferred orientation. The sub grains have the same shape and size as the grains in the SZ.

## **2. Grain Boundary Sliding**

Grain boundary sliding is deformation of a material by grains boundaries sliding along the boundaries of adjacent grains. Grain boundary sliding can be a mechanism for accommodating strain incompatibility between neighboring grains. Grain boundary sliding is more likely with smaller grains and/or the presence of a melt for plastic materials [13]. Some experiments show that, depending on the material, grain boundary sliding normally produces random orientation; however, preferred orientation is seen when grain boundary sliding is coupled with slip [13].

Even though it exhibits limited plasticity at room temperature, at the temperatures present during deformation in friction stir processing it acts like a plastic material. This is because there are two phases,  $\alpha$  and  $\beta$ . The  $\beta$  phase (BCC crystal structure) may be more ductile than the  $\alpha$  phase. It is possible that the  $\beta$  phase could act like a melt for the  $\alpha$  phase grains to move along. In order for this to be possible, the  $\beta$  phase would have to have time to diffuse through the alpha grains.

*a. Sequence of Microstructural Development in Ni Al Bronze During FSP*

From the results obtained on the microstructural features (from this work and prior cited work from this group) and the detailed orientation data that formed the main work of this thesis and elsewhere, a model for the sequence of microstructural development has been developed [Menon, McNelley, Unpublished work, NPS, 2010]. This model can be outlined with the help of the sketches in figures 35-38. At elevated temperatures, two phases, viz., the primary  $\alpha$  phase and the surrounding  $\beta$  phase, co-exist in these alloys during FSP as depicted in Figure 35. Upon cooling, the  $\beta$  phase transforms into  $\alpha$  and  $\kappa$  phases. As the temperature drops, recrystallization of the primary  $\alpha$  phase also occurs. From the optical microscopy of previous work [4] and the image quality maps presented earlier, it is clear that the large  $\alpha$  grains in the base metal develop sub grain structure rapidly as visualized in the sketch in Figure 35.

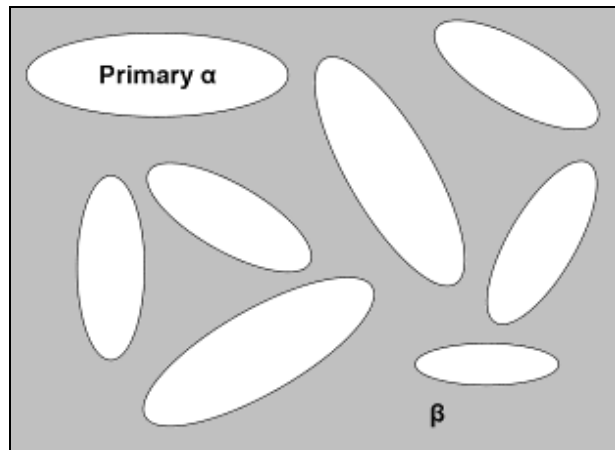


Figure 35. Sketch of grain structure while at an elevated temperature.  
(Created by T.R. McNelly)

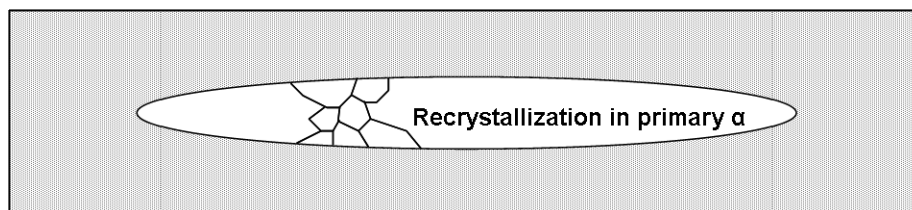


Figure 36. Sketch of subgrains within the recrystallized primary  $\alpha$  grains.  
(Created by T.R. McNelly)

Friction stir process applies shear forces along the alpha grains while they are at the elevated temperature. These forces cause the primary  $\alpha$  grains to elongate. See Figure 37 for a sketch of the elongated grain with sub grains included. This elongation with a preferred orientation was seen in the texture plots in the TMAZ. As the grains elongate the diameter gets closer to the diameter of the sub grains.

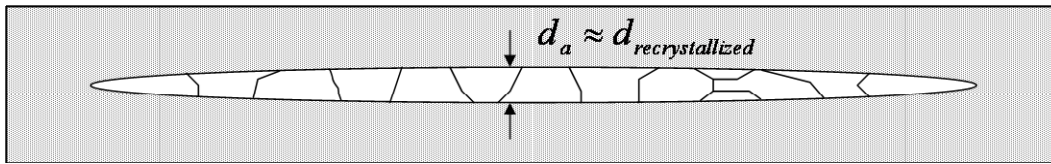


Figure 37. Sketch of an elongated primary  $\alpha$  grain with a diameter about the size of the sub grains. (Created by T.R. McNelly)

Once the elongated grain reaches the size of the sub grains, the surrounding  $\beta$  phase spreads along the  $\alpha$ : $\alpha$  sub grain boundaries. Once the more ductile  $\beta$  phase is between the  $\alpha$  sub grains, the sub grains are free to slide along the  $\alpha$ : $\beta$  interfaces during deformation instead of further shape change alone. See Figure 38 for a representation. The idea of sliding inside the stir zone would account for the random texture and refined grains seen in the data.

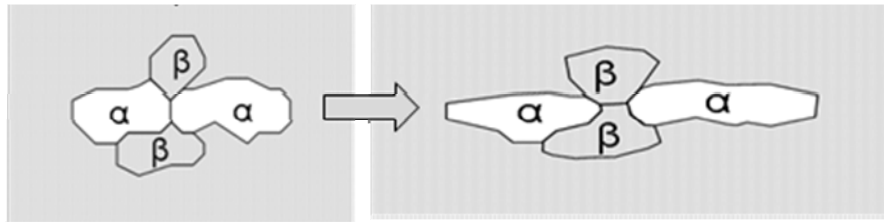


Figure 38. Sketch of  $\beta$  phase spreading along the primary  $\alpha$  subgrains. (Created by T.R. McNelly)

### ***b. Diffusion of Iron in Copper***

In the model above,  $\beta$  phase must diffuse between the  $\alpha$  sub grains. A conservative rough estimate is done by simplifying the NAB to an iron copper two phase system. The diffusion length equation (equation 1) will be used to calculate the diffusion time for 10  $\mu\text{m}$  or about half the length of a grain in the stir zone.

$$\text{Diffusion Length} = \sqrt{Dt} \quad (1)$$

Where D is the diffusion coefficient and t is time. This equation requires the calculation of a diffusion coefficient for a multi component system using Darken's equation (Equation 2) [19].

$$D_{Fe-Cu} = D_{Fe}N_{Cu} + D_{Cu}N_{Fe} \quad (2)$$

Where D is the diffusion coefficient and N is the molar concentration. The diffusion coefficients were calculated using equation 2 for copper and equation 3 for iron.

$$D_{Cu} = 0.468 \exp(-47140 / RT) \quad (3)$$

Where D is in  $\text{cm}^2\text{sec}^{-1}$  and temperature is in the range of 685-1062°C [14]

$$D_{Fe} = 0.18 \exp(-64500 / RT) \quad (4)$$

Where D is in  $\text{cm}^2\text{sec}^{-1}$  and temperature is greater than 700°C [15]

Since peak temperatures during friction stir processing are between 800 and 900°C a conservative estimate would be to calculate time it takes for iron to diffuse in a temperature equal to 800°C. By using root mean square diffusion equation (equation 1), the estimated time iron requires to move 10  $\mu\text{m}$  in copper is 0.008 sec. Since the tool traverse speed was 2 inches per minute, the temperature would be above 800°C for more than 0.008 sec. This means there is enough time for the  $\beta$  particles to diffuse around the  $\alpha$  particles. Grain boundary sliding is a plausible model for FSP of NAB. It is also more consistent with what was seen in the data than dynamic recovery.

THIS PAGE INTENTIONALLY LEFT BLANK

## V. CONCLUSIONS

Friction Stir Processing (FSP) is a promising technique that can be used to reduce production and repair time/cost for Navy Propellers. FSP refines the grains and removes the pores created during casting. This would eliminate the need for heat treatment and fusion welding. This thesis looked at data from processed NAB taken with OIM. From this the grain orientation and texture, was used to look at plausibility of modeling FSP of NAB with either dynamic recovery or grain boundary sliding.

### A. CONCLUSIONS FROM RESULTS

During FSP, the as-cast microstructure experiences both high temperatures as well as high strain rates for deformation. Substantial changes in the microstructures are observed. In this work, the details of the evolution of microstructures in Ni Al bronze during both single-pass and multi-pass friction stir processing for 1200 rpm /2 ipm was examined primarily by OIM. The following conclusions could be drawn based on this study:

1. As-cast, inhomogeneous microstructures composed of large  $\alpha$  grains and lamellar eutectoid regions are completely replaced by a highly refined, homogeneous distribution of fine equiaxed  $\alpha$  grains and regions of  $(\alpha + \kappa)$  formed as a result of transformation of the  $\beta$  phase.

2. In the advancing side of both the single-pass and multi-pass friction stir processed samples, development of distinct fiber texture in the TMAZ was observed. The fiber texture indicates that the lattice rotates about the [110] axis. This is consistent with B type shear texture with rotational symmetry about the [110] axis caused by the tool rotation.

3. The change in texture resulting from the increasing strain along the radial direction of the tool could be followed by examining the peak intensities in the pole figures obtained from various regions from the base material to the stir zone. This study

shows that there was a rapid development of texture as the TMAZ was approached from the base material and a very rapid drop as the stir zone was reached and random orientations prevailed.

4. Based on the microstructural and texture data obtained here (and from ongoing work by Prof. McNelley's group) a model for the microstructural development in Ni Al bronze during FSP has been proposed and was briefly outlined here. According to this, high temperature high strain rate deformation leads to  $\beta$  phase formation, substructure development in  $\alpha$  and spreading of  $\beta$  along  $\alpha:\alpha$  boundaries with subsequent interface sliding. Following FSP, the  $\beta$  phase regions undergo phase transformations and the microstructure is a mixture of fine, equiaxed, randomly oriented  $\alpha$  grains and  $\beta$  transformation products distributed in a homogeneous fashion.

## **B. FUTURE RESEARCH**

1. More OIM experiments on both single-pass and multi-pass FSP samples under various rpm/ipm combinations must be carried out and data substantiated with the volume of microstructural data already available in Dr. McNelley's group.

2. More data on other sections, in particular plan sections, under different FSP conditions must be obtained. Studies on texture development on the retreating side may also be useful.

3. Study the feasibility of creating a desired shape like a propeller without leaving a hole where the tool is extract. For example, what is the cost of casting the propeller with a tool extraction point, removing the excess material, and then reshaping the propeller?

## APPENDIX A – SINGLE-PASS

### A. EXTRA DATA AND FIGURES FOR HORIZONTAL CENTERLINE

Table 5. Single-Pass Horizontal Centerline Number Fraction of Grain Boundaries at a Misorientation Angle.

| Angle<br>[degrees]         | Single-pass Horizontal Centerline - Number Fraction |          |          |          |          |          |          |          |
|----------------------------|---|----------|----------|----------|----------|----------|----------|----------|
|                            | Scan 8  | Scan 7   | Scan 6   | Scan 5   | Scan 4   | Scan 3   | Scan 2   | Scan 1   |
| 3.575                      | 0.111664  | 0.094026 | 0.138792 | 0.239286 | 0.207425 | 0.381768 | 0.334419 | 0.491076 |
| 6.725                      | 0.0281677   | 0.025543 | 0.038105 | 0.090717 | 0.07019  | 0.098977 | 0.100816 | 0.09898  |
| 9.875                      | 0.0165334   | 0.017449 | 0.029226 | 0.050536 | 0.040408 | 0.052305 | 0.056168 | 0.029503 |
| 13.025                     | 0.014708  | 0.014495 | 0.024927 | 0.028498 | 0.023582 | 0.031421 | 0.036138 | 0.014114 |
| 16.175                     | 0.014813  | 0.015305 | 0.020423 | 0.017725 | 0.018581 | 0.020347 | 0.020065 | 0.004826 |
| 19.325                     | 0.0139422   | 0.017357 | 0.019857 | 0.011956 | 0.015681 | 0.009158 | 0.017789 | 0.002823 |
| 22.475                     | 0.0175091   | 0.018742 | 0.018454 | 0.011356 | 0.01153  | 0.007549 | 0.010435 | 0.00428  |
| 25.625                     | 0.0217264   | 0.024209 | 0.020063 | 0.008953 | 0.009777 | 0.00889  | 0.014567 | 0.014387 |
| 28.775                     | 0.024433  | 0.030261 | 0.020899 | 0.011265 | 0.011322 | 0.004713 | 0.013062 | 0.017483 |
| 31.925                     | 0.0335075   | 0.034806 | 0.030461 | 0.015832 | 0.016358 | 0.006667 | 0.018699 | 0.026407 |
| 35.075                     | 0.0426974   | 0.047926 | 0.040537 | 0.023985 | 0.020143 | 0.008698 | 0.021711 | 0.034238 |
| 38.225                     | 0.0489709   | 0.052593 | 0.04073  | 0.017416 | 0.021602 | 0.008698 | 0.019995 | 0.034966 |
| 41.375                     | 0.0467153   | 0.051414 | 0.040769 | 0.017161 | 0.020508 | 0.009733 | 0.017614 | 0.033327 |
| 44.525                     | 0.0541743   | 0.057876 | 0.051412 | 0.019872 | 0.029416 | 0.044986 | 0.032882 | 0.055819 |
| 47.675                     | 0.0503137   | 0.054983 | 0.050099 | 0.016378 | 0.020456 | 0.006323 | 0.015303 | 0.02668  |
| 50.825                     | 0.0527475   | 0.054994 | 0.056225 | 0.024768 | 0.023547 | 0.007855 | 0.014147 | 0.022856 |
| 53.975                     | 0.0544051   | 0.054942 | 0.056868 | 0.033466 | 0.027767 | 0.009082 | 0.01989  | 0.039428 |
| 57.125                     | 0.070393  | 0.070196 | 0.077047 | 0.072738 | 0.061785 | 0.03805  | 0.036313 | 0.030687 |
| 60.275                     | 0.282243  | 0.262453 | 0.224899 | 0.28782  | 0.349332 | 0.244626 | 0.199846 | 0.017756 |
| 63.425                     | 0.0003357   | 0.000431 | 0.000206 | 0.000273 | 0.00059  | 0.000153 | 0.00014  | 0.000364 |
| low angle                  | 0.1710731   | 0.151512 | 0.23105  | 0.409037 | 0.341605 | 0.564471 | 0.527542 | 0.633673 |
| high angle                 | 0.8289271   | 0.848488 | 0.76895  | 0.590963 | 0.658395 | 0.435529 | 0.472459 | 0.366327 |
| Total<br>Average<br>Number | 40.7349   | 40.9102  | 37.6161  | 32.3382  | 35.5436  | 24.972   | 25.1822  | 18.307   |
| distance<br>into SZ        | 6.306   | 0.154    | 0        | -0.112   | -0.372   | -0.684   | -0.888   | -1.771   |



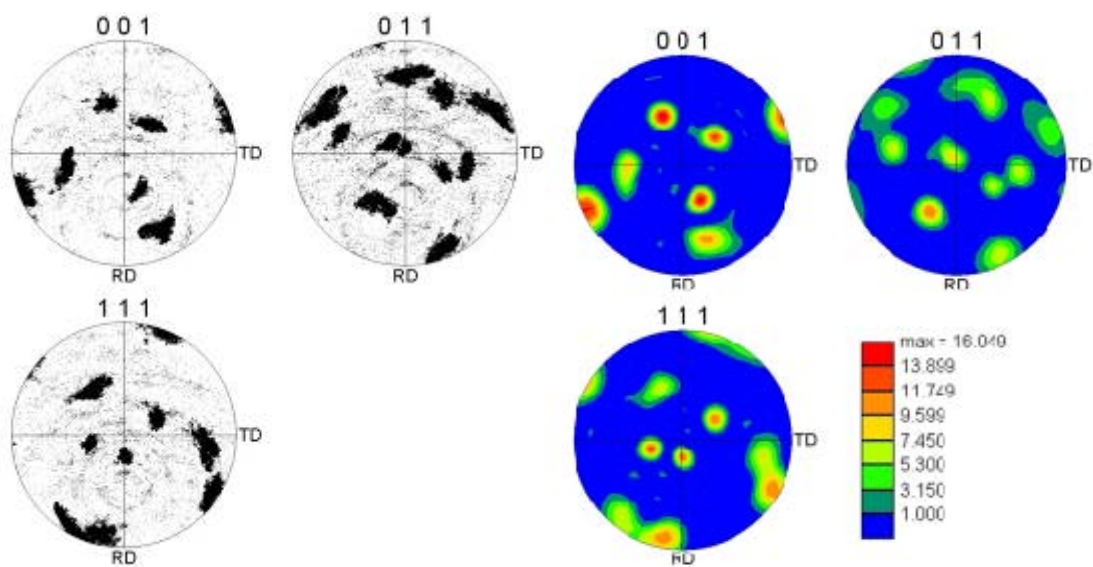


Figure 39. Single-Pass Pole Figure with Coorispending texture pole figure from Scan 1.

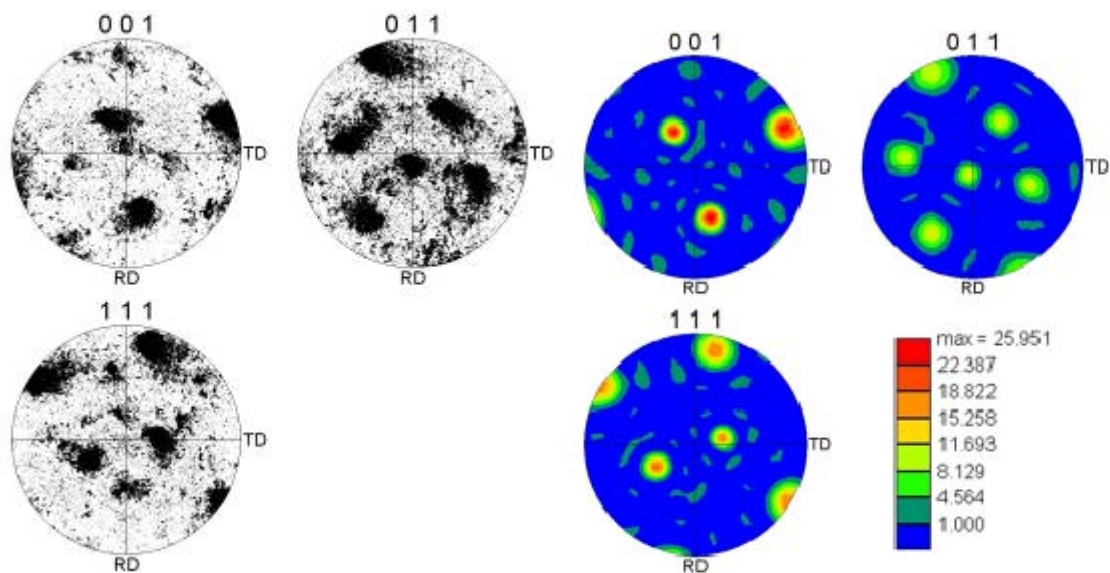


Figure 40. Single-Pass Pole Figure with coorispending texture pole figure from Scan 2.

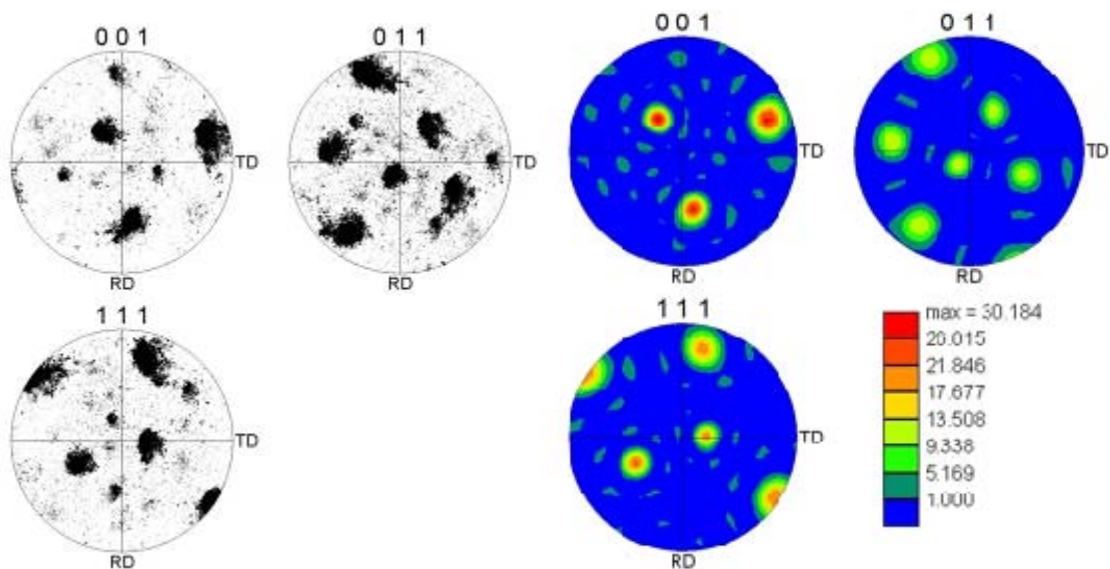


Figure 41. Single-Pass Pole Figure with coorresponding texture pole figure from Scan 3.

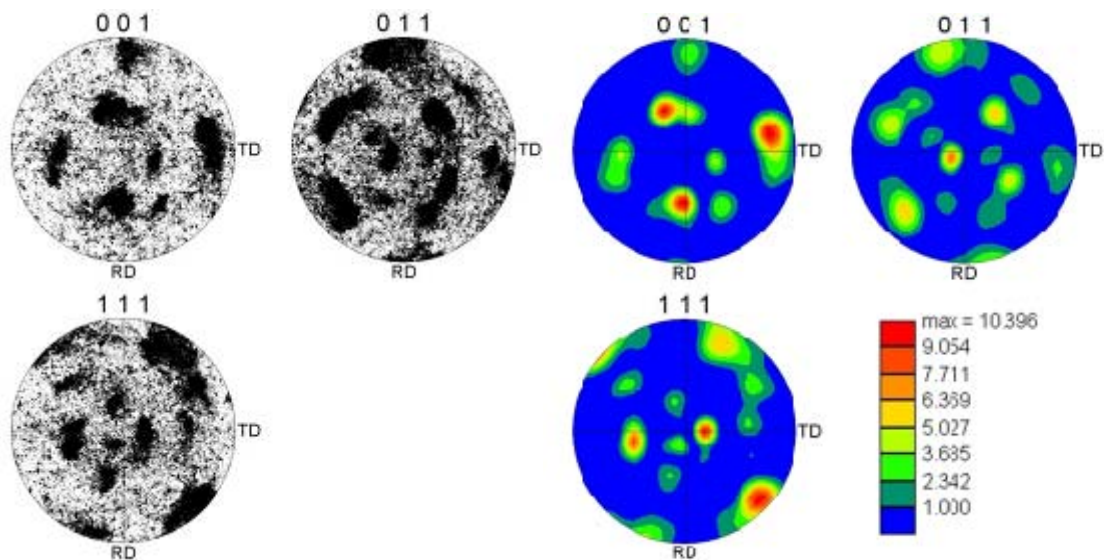


Figure 42. Single-Pass Pole Figure with coorresponding texture pole figure from Scan 4.

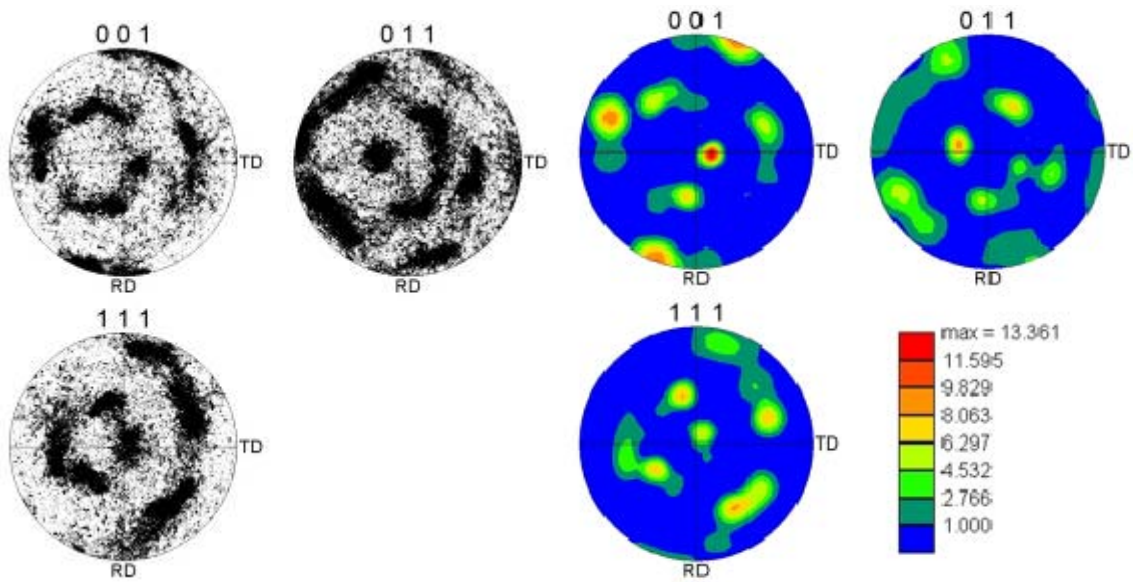


Figure 43. Single-Pass Pole Figure with coorispnding texture pole figure from Scan 5.

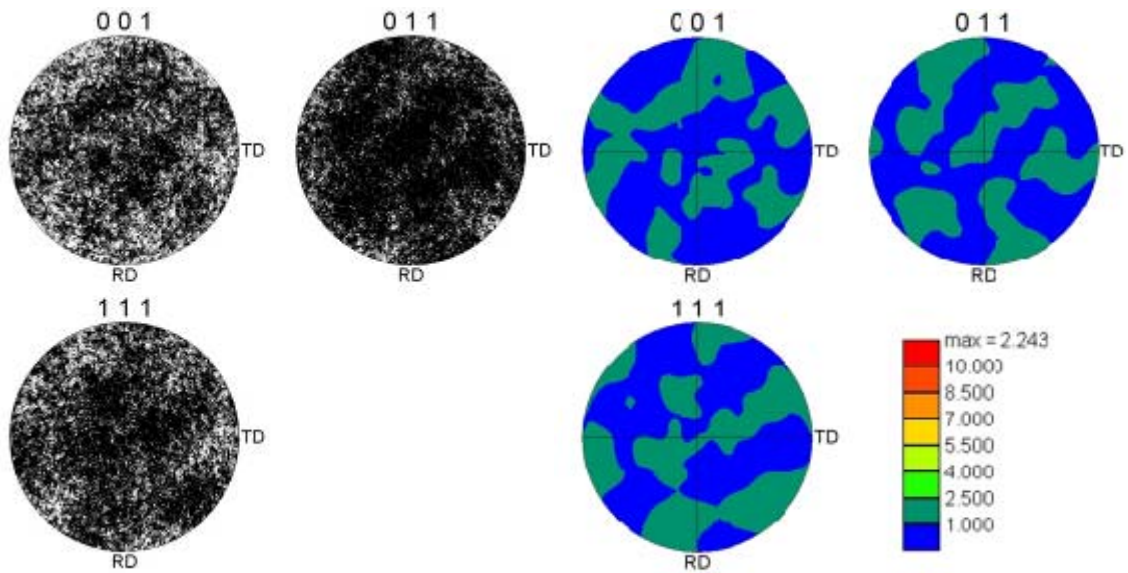


Figure 44. Single-Pass Pole Figure with coorispnding texture pole figure from Scan 6.



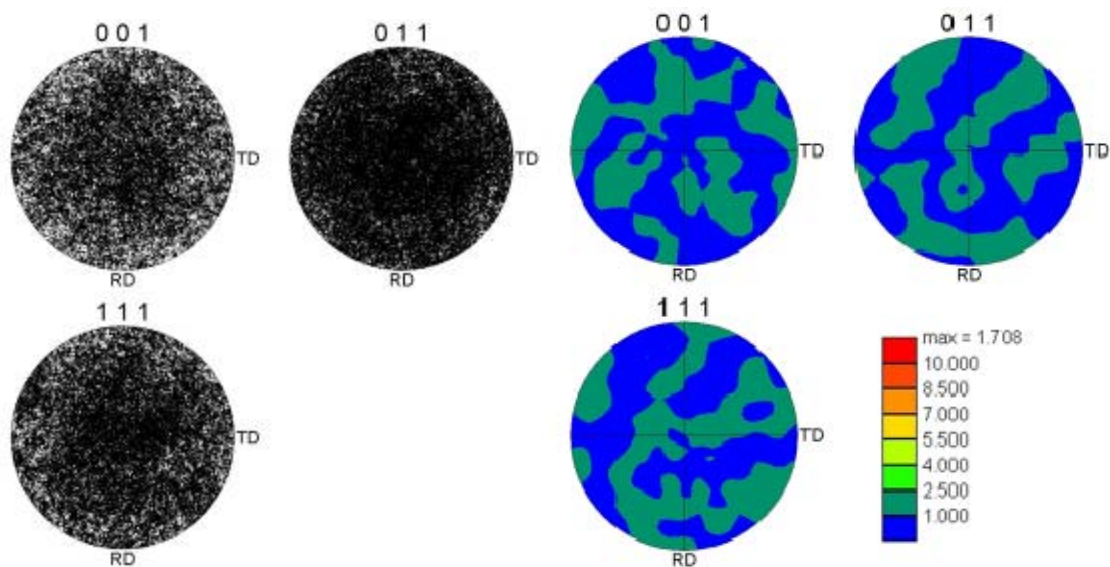


Figure 45. Single-Pass Pole Figure with corresponding texture pole figure from Scan 7.

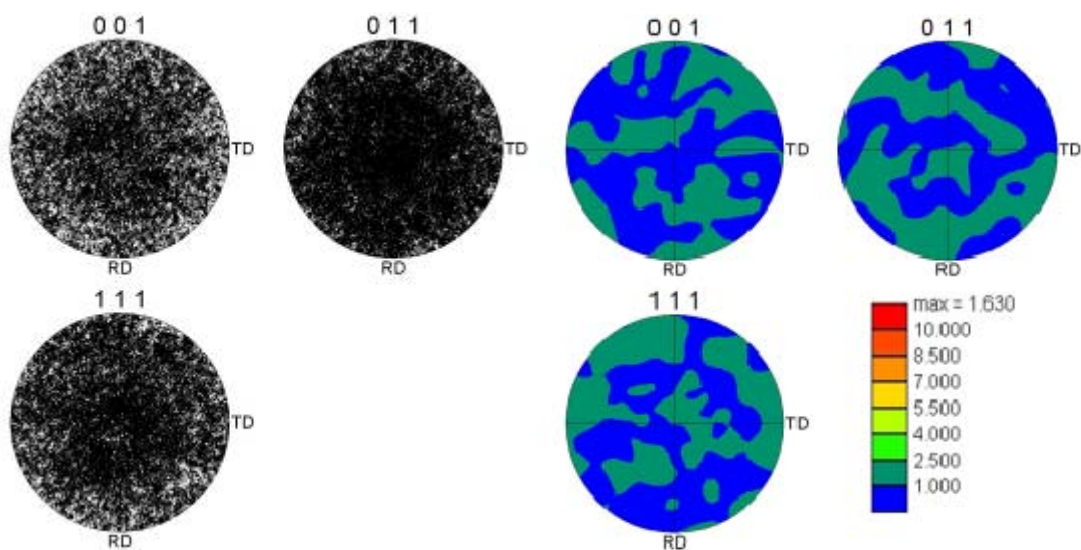


Figure 46. Single-Pass Pole Figure with corresponding texture pole figure from Scan 8.

## B. EXTRA DATA AND FIGURES FOR VERTICAL CENTERLINE

Table 6. Single-Pass Vertical Centerline Number Fraction of Grain Boundaries at a Misorientation Angle.

| Angle<br>[degrees] | Single-Pass Vertical Centerline - Number Fraction |          |          |          |          |          |          |          |          |
|--------------------|---|----------|----------|----------|----------|----------|----------|----------|----------|
|                    | Scan A  | Scan B   | Scan C   | Scan D   | Scan E   | Scan F   | Scan G   | Scan H   | Scan I   |
| 3.575              | 0.448091  | 0.340883 | 0.36681  | 0.466848 | 0.169288 | 0.098437 | 0.13441  | 0.111869 | 0.111664 |
| 6.725              | 0.05964   | 0.101633 | 0.099903 | 0.119959 | 0.055856 | 0.027378 | 0.037638 | 0.028542 | 0.028168 |
| 9.875              | 0.012622  | 0.039664 | 0.045818 | 0.048608 | 0.03922  | 0.019253 | 0.022617 | 0.018342 | 0.016533 |
| 13.025             | 0.007258  | 0.004714 | 0.023833 | 0.027225 | 0.02844  | 0.015367 | 0.017746 | 0.01667  | 0.014708 |
| 16.175             | 0.010729  | 0.001035 | 0.012488 | 0.017072 | 0.021717 | 0.013583 | 0.016328 | 0.015269 | 0.014813 |
| 19.325             | 0.005364  | 0.002529 | 0.009014 | 0.013896 | 0.018947 | 0.016586 | 0.016081 | 0.015112 | 0.013942 |
| 22.475             | 0.002524  | 0.00161  | 0.00686  | 0.01055  | 0.017608 | 0.014484 | 0.019016 | 0.016649 | 0.017509 |
| 25.625             | 0.011676  | 0.002069 | 0.005716 | 0.012875 | 0.019407 | 0.021408 | 0.020755 | 0.019878 | 0.021726 |
| 28.775             | 0.015147  | 0.006323 | 0.010685 | 0.013556 | 0.020917 | 0.02706  | 0.023925 | 0.024926 | 0.024433 |
| 31.925             | 0.032502  | 0.021269 | 0.025899 | 0.014633 | 0.027285 | 0.045271 | 0.031534 | 0.032838 | 0.033508 |
| 35.075             | 0.064058  | 0.03748  | 0.027834 | 0.01815  | 0.037618 | 0.063905 | 0.043508 | 0.04516  | 0.042697 |
| 38.225             | 0.042916  | 0.034721 | 0.02203  | 0.02161  | 0.035806 | 0.054014 | 0.042744 | 0.049664 | 0.048971 |
| 41.375             | 0.026191  | 0.032306 | 0.024888 | 0.015824 | 0.036292 | 0.048839 | 0.042361 | 0.046299 | 0.046715 |
| 44.525             | 0.061849  | 0.220281 | 0.057119 | 0.02541  | 0.043789 | 0.061309 | 0.053276 | 0.054064 | 0.054174 |
| 47.675             | 0.0142  | 0.010922 | 0.017589 | 0.015654 | 0.043159 | 0.05495  | 0.046641 | 0.04703  | 0.050314 |
| 50.825             | 0.021773  | 0.015176 | 0.02203  | 0.018774 | 0.051996 | 0.050782 | 0.052992 | 0.049727 | 0.052748 |
| 53.975             | 0.075103  | 0.032191 | 0.030121 | 0.028246 | 0.054806 | 0.055427 | 0.057764 | 0.053782 | 0.054405 |
| 57.125             | 0.042916  | 0.026903 | 0.052986 | 0.039533 | 0.079031 | 0.076588 | 0.084686 | 0.078467 | 0.070393 |
| 60.275             | 0.044494  | 0.067832 | 0.138071 | 0.071465 | 0.198529 | 0.234761 | 0.235719 | 0.275221 | 0.282243 |
| 63.425             | 0.000947  | 0.00046  | 0.000308 | 0.000113 | 0.000289 | 0.000601 | 0.000259 | 0.000491 | 0.000336 |
| low angle          | 0.527611  | 0.486894 | 0.536364 | 0.662639 | 0.292804 | 0.160435 | 0.212412 | 0.175423 | 0.171073 |
| high angle         | 0.472389  | 0.513107 | 0.463636 | 0.33736  | 0.707195 | 0.839565 | 0.787589 | 0.824577 | 0.828927 |
| Total              |   |          |          |          |          |          |          |          |          |
| Average            |   |          |          |          |          |          |          |          |          |
| Number             | 22.8072   | 25.5844  | 24.5974  | 17.9749  | 34.9154  | 40.1902  | 38.5901  | 40.5407  | 40.7349  |
| distance           |   |          |          |          |          |          |          |          |          |
| into SZ            | -0.9355   | -0.4185  | -0.1725  | -0.0625  | 0.0625   | 0.2525   | 0.4295   | 1.8835   | 3.0625   |

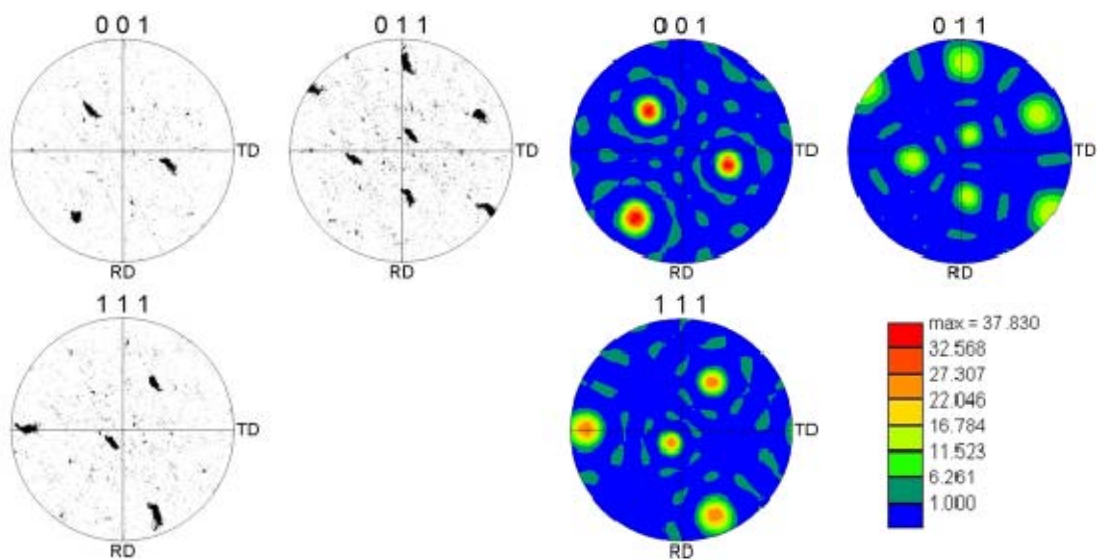


Figure 47. Single-Pass Pole Figure with coorisponding texture pole figure from Scan A.

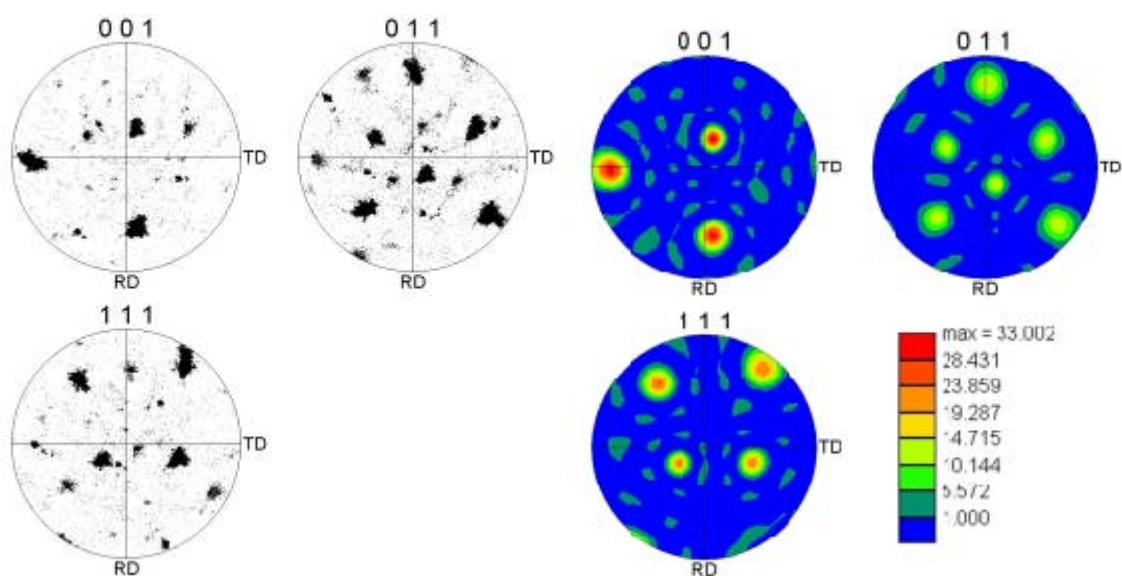


Figure 48. Single-Pass Pole Figure with coorisponding texture pole figure from Scan B.

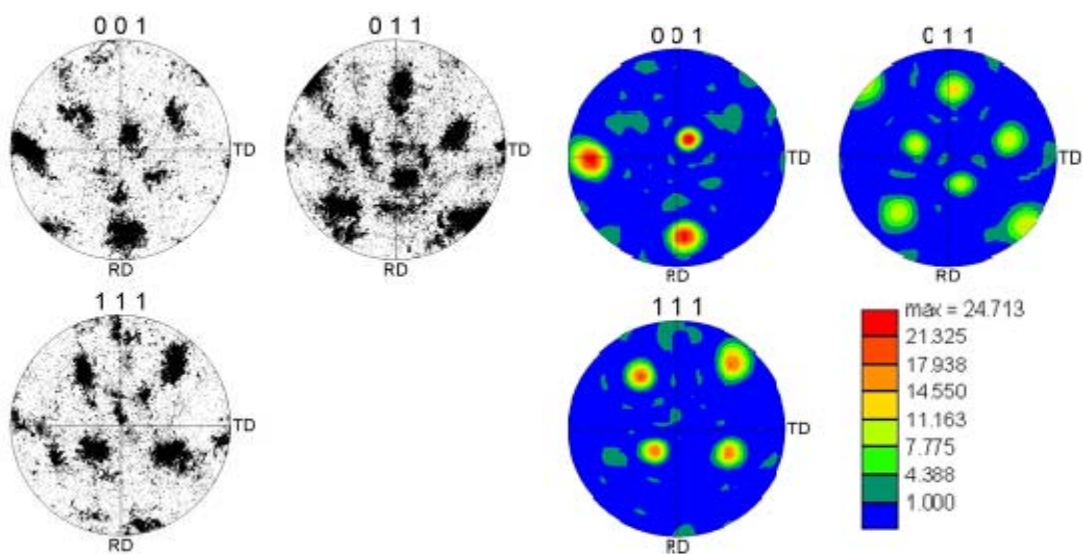


Figure 49. Single-Pass Pole Figure with coorispnding texture pole figure from Scan C.

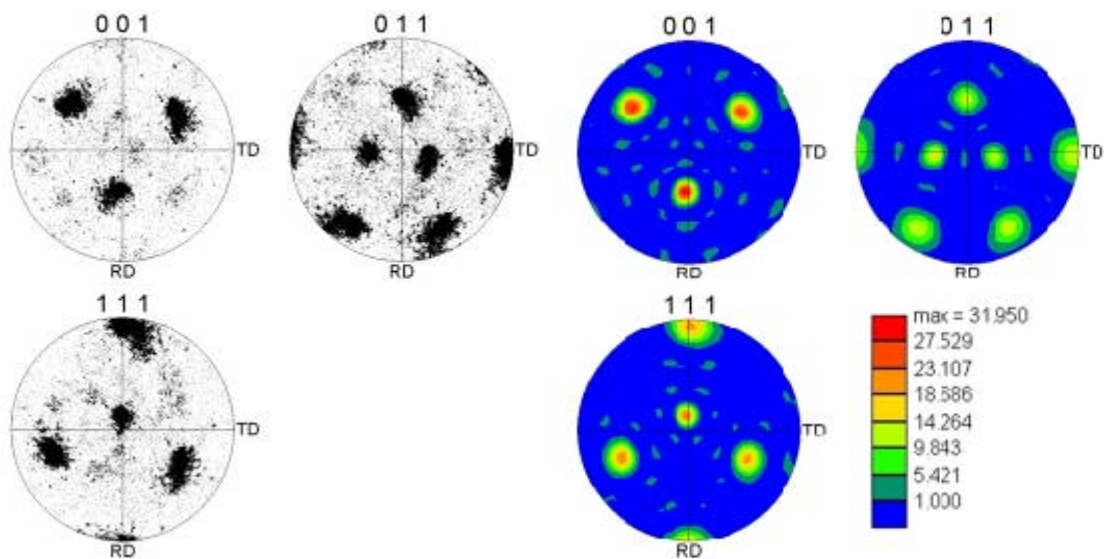


Figure 50. Single-Pass Pole Figure with coorispnding texture pole figure from Scan D.



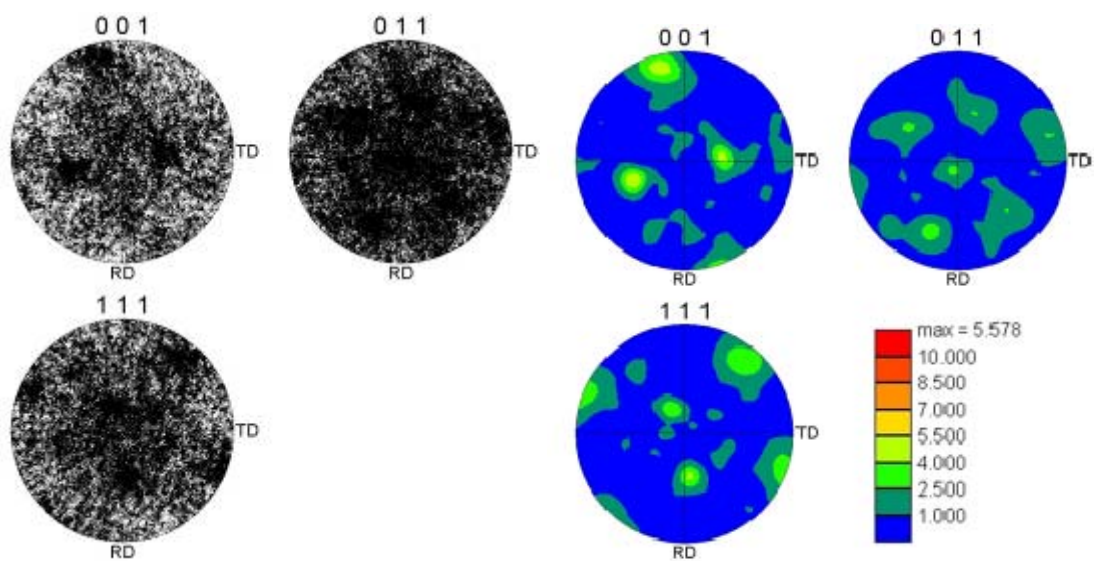


Figure 51. Single-Pass Pole Figure with coorisponding texture pole figure from Scan E.

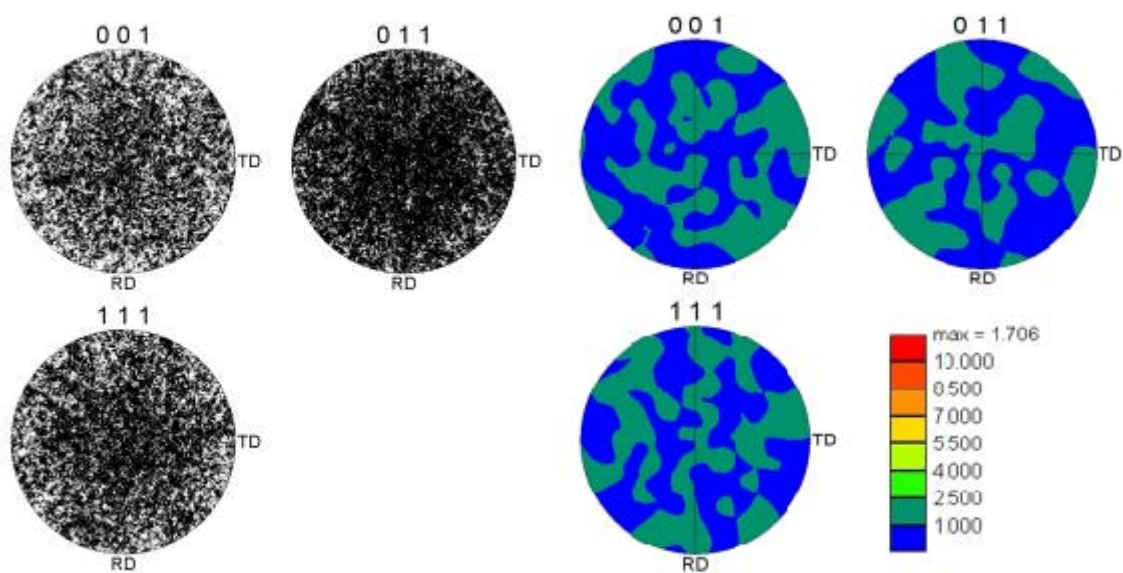


Figure 52. Single-Pass Pole Figure with coorisponding texture pole figure from Scan F.



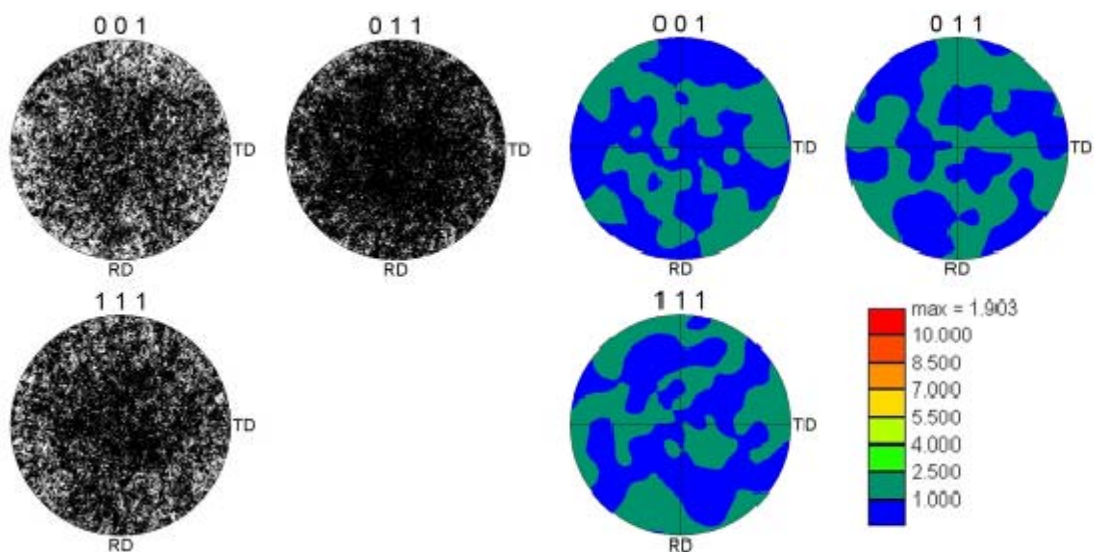


Figure 53. Single-Pass Pole Figure with coorisponding texture pole figure from Scan G.

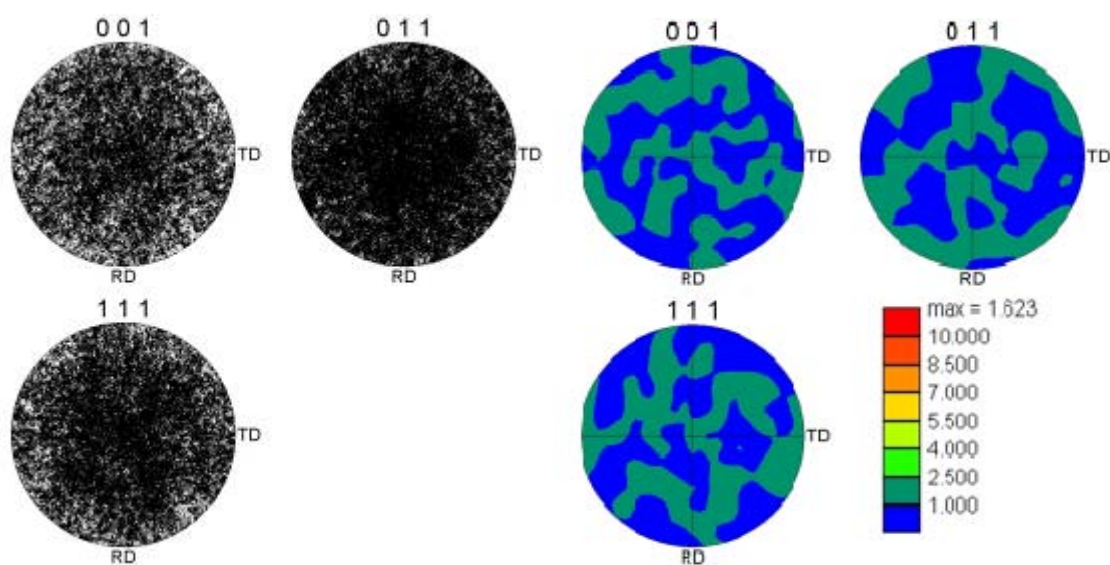


Figure 54. Single-Pass Pole Figure with coorisponding texture pole figure from Scan H.

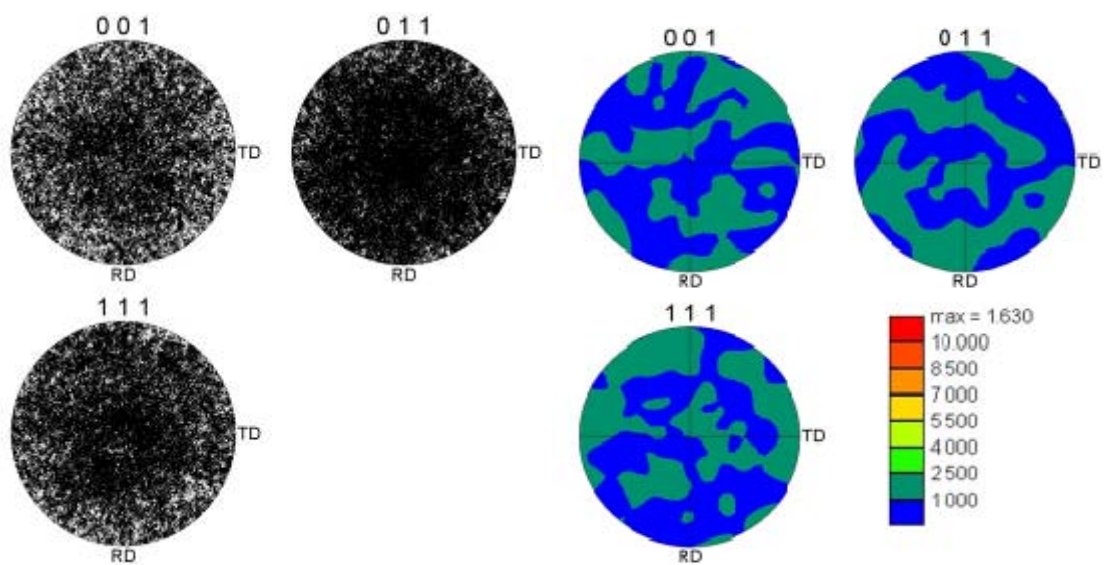


Figure 55. Single-Pass Pole Figure with coorispending texture pole figure from Scan I.

THIS PAGE INTENTIONALLY LEFT BLANK

## **APPENDIX B – MULTI-PASS**

### **A. EXTRA DATA AND FIGURES FOR HORIZONTAL CENTERLINE**

Table 7. Multi-pass Horizontal Centerline Number Fraction of Grain Boundaries at a Misorientation Angle.

| Angle<br>[degrees]      | Multi-pass Horizontal Centerline-Number Fraction |          |          |          |          |          |          |          |          |          |          |          |          |
|-------------------------|--|----------|----------|----------|----------|----------|----------|----------|----------|----------|----------|----------|----------|
|                         | Scan 13  | Scan 12  | Scan 11  | Scan 10  | Scan 9   | Scan 8   | Scan 7   | Scan 6   | Scan 5   | Scan 4   | Scan 3   | Scan 2   | Scan 1   |
| 3.575                   | 0.093478   | 0.104983 | 0.118649 | 0.099359 | 0.09132  | 0.078279 | 0.108193 | 0.353414 | 0.40212  | 0.405342 | 0.459544 | 0.163394 | 0.39066  |
| 6.725                   | 0.025512   | 0.029802 | 0.032869 | 0.02668  | 0.022669 | 0.018202 | 0.039572 | 0.101869 | 0.104424 | 0.068273 | 0.060965 | 0.024242 | 0.043693 |
| 9.875                   | 0.016478   | 0.01948  | 0.01981  | 0.017021 | 0.014581 | 0.013211 | 0.036705 | 0.066277 | 0.064117 | 0.030634 | 0.011719 | 0.010667 | 0.008696 |
| 13.025                  | 0.014392   | 0.014105 | 0.01468  | 0.013097 | 0.010287 | 0.012615 | 0.025821 | 0.032197 | 0.029493 | 0.022042 | 0.003117 | 0.012121 | 0.005904 |
| 16.175                  | 0.012411   | 0.014584 | 0.01133  | 0.012873 | 0.012901 | 0.011698 | 0.026404 | 0.01799  | 0.018771 | 0.013729 | 0.002493 | 0.010667 | 0.000644 |
| 19.325                  | 0.017378   | 0.013643 | 0.013931 | 0.01803  | 0.008649 | 0.013415 | 0.028447 | 0.01775  | 0.014409 | 0.010647 | 0.003241 | 0.010667 | 0.003221 |
| 22.475                  | 0.015202   | 0.0139   | 0.015553 | 0.013546 | 0.009707 | 0.017009 | 0.015383 | 0.006403 | 0.00725  | 0.008966 | 0.005486 | 0.017697 | 0.004079 |
| 25.625                  | 0.018353   | 0.016279 | 0.017566 | 0.018497 | 0.013979 | 0.018231 | 0.014181 | 0.005941 | 0.005806 | 0.007845 | 0.012467 | 0.013576 | 0.016425 |
| 28.775                  | 0.02263  | 0.020456 | 0.021824 | 0.020272 | 0.019641 | 0.022611 | 0.019039 | 0.008026 | 0.006359 | 0.012515 | 0.019948 | 0.030788 | 0.078154 |
| 31.925                  | 0.028228   | 0.028689 | 0.033849 | 0.033892 | 0.030219 | 0.030104 | 0.026954 | 0.010517 | 0.008971 | 0.0198   | 0.045506 | 0.060364 | 0.070531 |
| 35.075                  | 0.043895   | 0.040141 | 0.042739 | 0.047886 | 0.039863 | 0.041525 | 0.03583  | 0.010886 | 0.016129 | 0.024563 | 0.075053 | 0.087758 | 0.082233 |
| 38.225                  | 0.049868   | 0.041699 | 0.050809 | 0.049754 | 0.043928 | 0.054067 | 0.033581 | 0.01144  | 0.016191 | 0.022789 | 0.067822 | 0.063273 | 0.028341 |
| 41.375                  | 0.041269   | 0.040929 | 0.041492 | 0.047774 | 0.0364   | 0.049775 | 0.031795 | 0.012233 | 0.013026 | 0.022789 | 0.029173 | 0.156364 | 0.023081 |
| 44.525                  | 0.046041   | 0.047947 | 0.049419 | 0.053136 | 0.048865 | 0.051027 | 0.039074 | 0.015056 | 0.017512 | 0.05884  | 0.074928 | 0.118061 | 0.050993 |
| 47.675                  | 0.04325  | 0.04365  | 0.045838 | 0.045737 | 0.041522 | 0.045861 | 0.042439 | 0.016126 | 0.01275  | 0.022415 | 0.014462 | 0.042909 | 0.044337 |
| 50.825                  | 0.05341  | 0.04704  | 0.047549 | 0.049736 | 0.048408 | 0.050619 | 0.07123  | 0.047715 | 0.036068 | 0.034837 | 0.019324 | 0.03103  | 0.039292 |
| 53.975                  | 0.056696   | 0.051542 | 0.050702 | 0.049568 | 0.048263 | 0.048422 | 0.05389  | 0.032253 | 0.033794 | 0.039133 | 0.03815  | 0.057939 | 0.03854  |
| 57.125                  | 0.07637  | 0.075626 | 0.074503 | 0.067541 | 0.06639  | 0.064994 | 0.08129  | 0.07827  | 0.072074 | 0.065471 | 0.024436 | 0.06303  | 0.037681 |
| 60.275                  | 0.324899   | 0.335302 | 0.296694 | 0.315229 | 0.392181 | 0.358233 | 0.269709 | 0.155507 | 0.120492 | 0.109088 | 0.031792 | 0.025455 | 0.030811 |
| 63.425                  | 0.00024  | 0.000205 | 0.000196 | 0.000374 | 0.000228 | 0.000102 | 0.000464 | 0.000129 | 0.000246 | 0.00028  | 0.000374 | 0        | 0.002684 |
| low angle               | 0.149859   | 0.16837  | 0.186008 | 0.156157 | 0.138857 | 0.122307 | 0.210291 | 0.553757 | 0.600154 | 0.526291 | 0.535345 | 0.210424 | 0.448953 |
| high angle              | 0.850141   | 0.83163  | 0.813992 | 0.843843 | 0.861143 | 0.877693 | 0.78971  | 0.446243 | 0.399847 | 0.473709 | 0.464655 | 0.789577 | 0.551047 |
| Total Average<br>Number | 42.5227  | 42.074   | 40.6086  | 41.8222  | 44.2203  | 43.9164  | 39.3242  | 25.0218  | 22.3708  | 24.5735  | 21.2336  | 33.9639  | 24.2625  |
| distance into<br>SZ     | 6.42   | 4.166    | 3.893    | 3.715    | 0.885    | 0.032    | -0.018   | -0.435   | -0.855   | -1.327   | -1.824   | -2.359   | -2.824   |

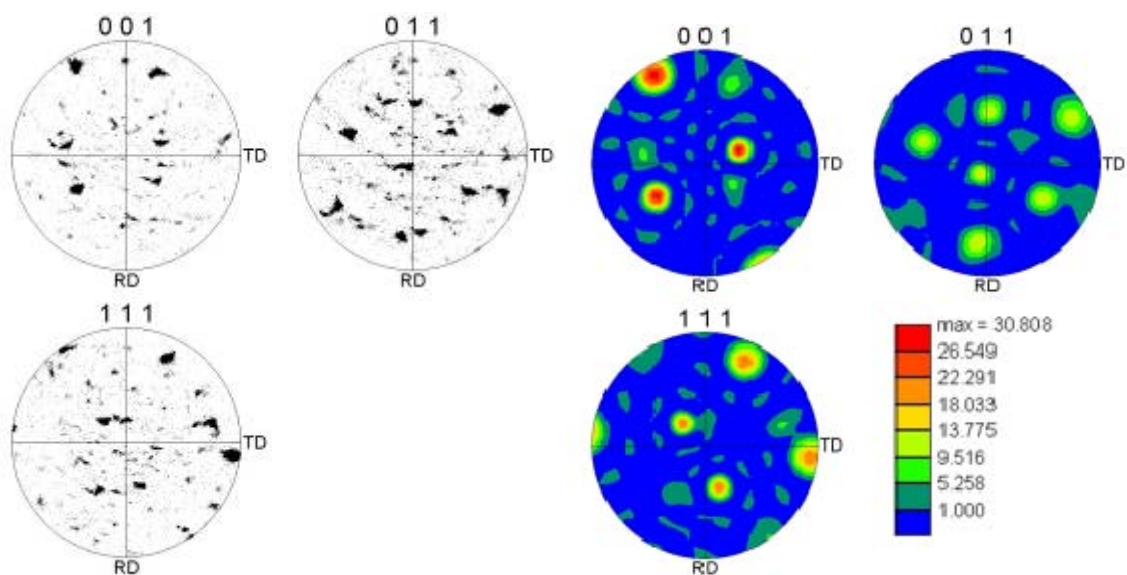


Figure 56. Multipass Pole Figure with coorisponding texture pole figure from Scan 1.

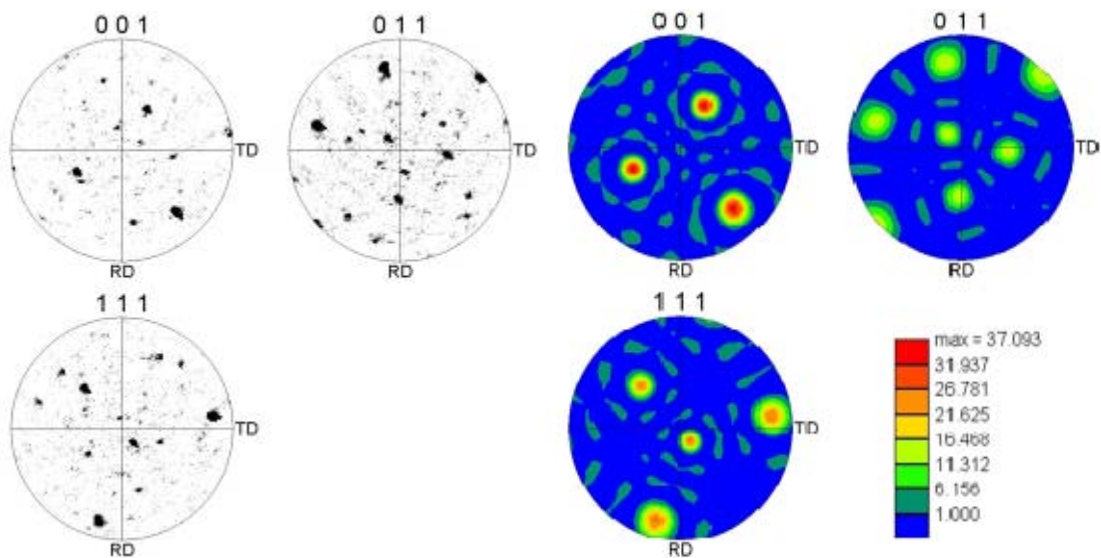


Figure 57. Multipass Pole Figure with coorisponding texture pole figure from Scan 2.

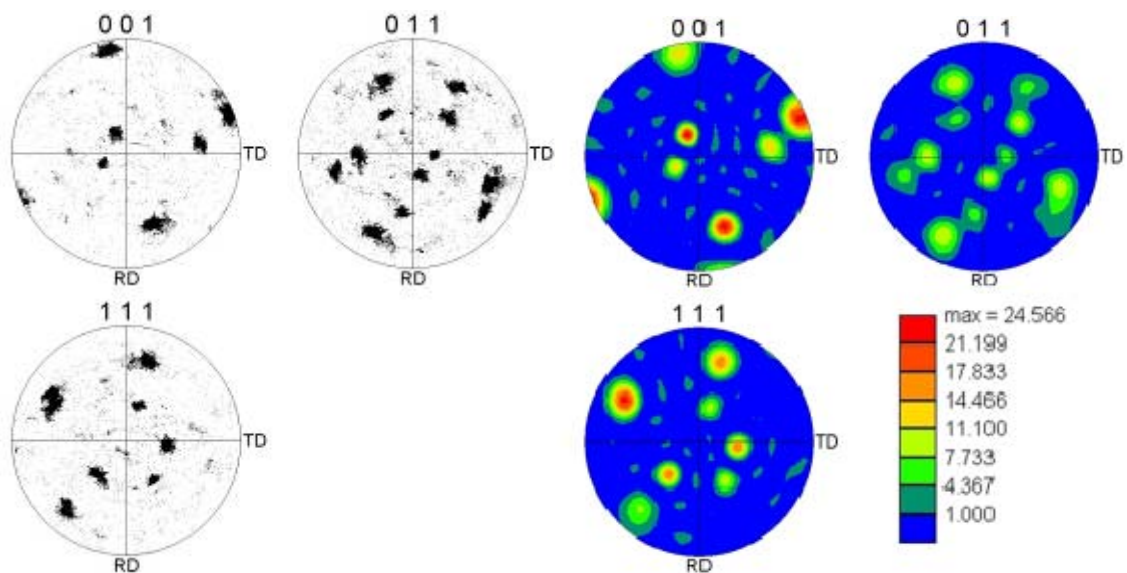


Figure 58. Multipass Pole Figure with coorisponding texture pole figure from Scan 3.

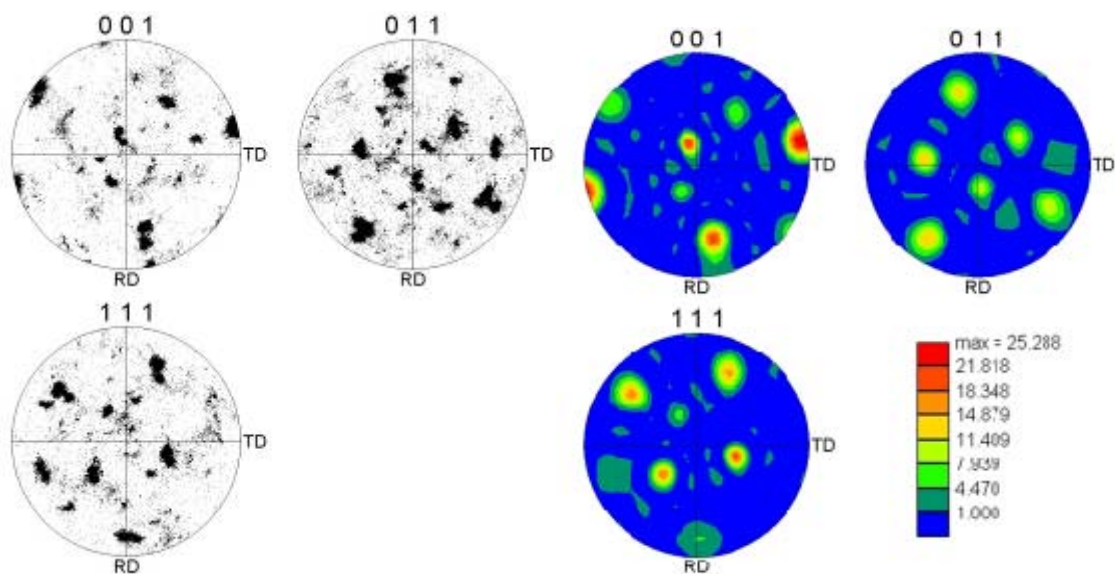


Figure 59. Multipass Pole Figure with coorisponding texture pole figure from Scan 4.



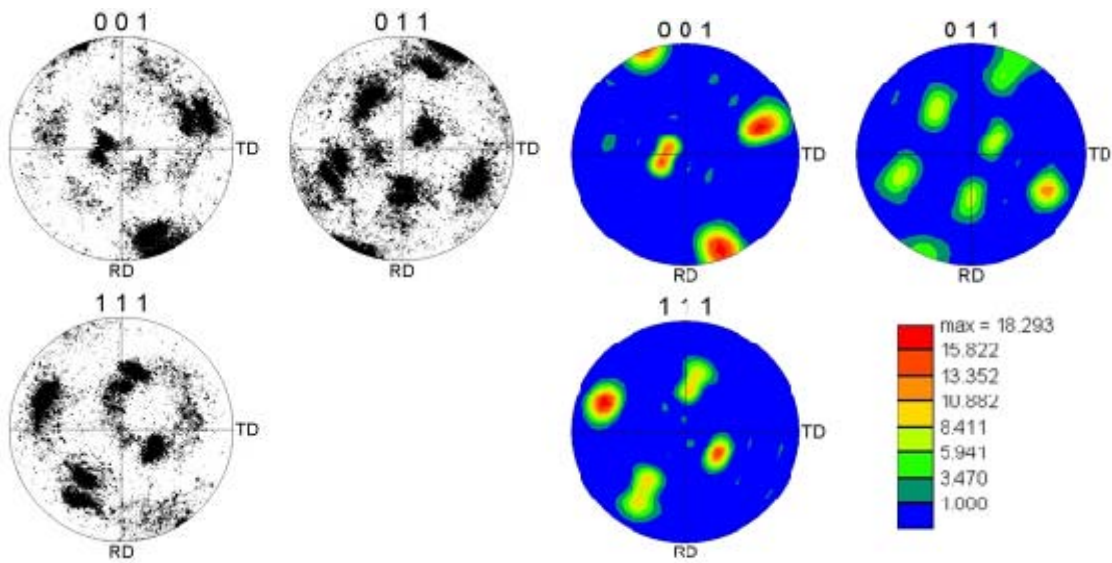


Figure 60. Multipass Pole Figure with coorisponding texture pole figure from Scan 5.

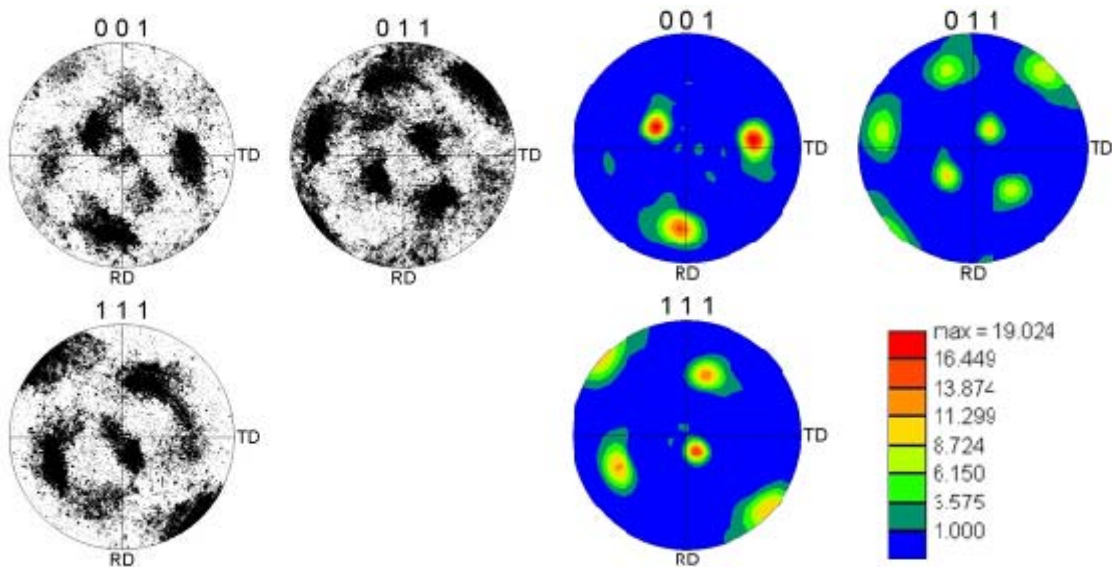


Figure 61. Multipass Pole Figure with coorisponding texture pole figure from Scan 6.



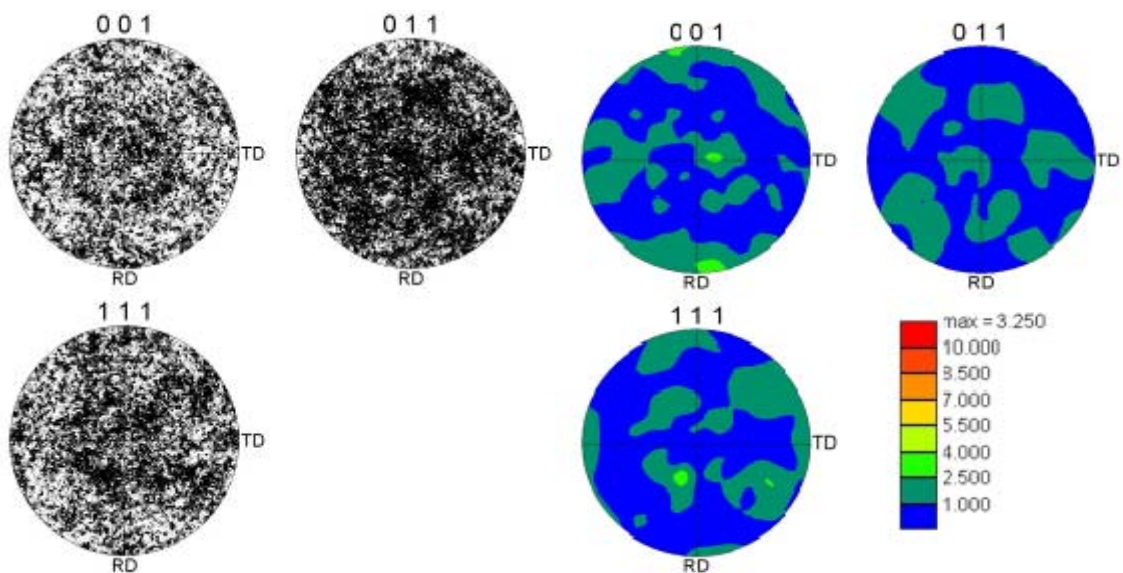


Figure 62. Multipass Pole Figure with coorisponding texture pole figure from Scan 7.

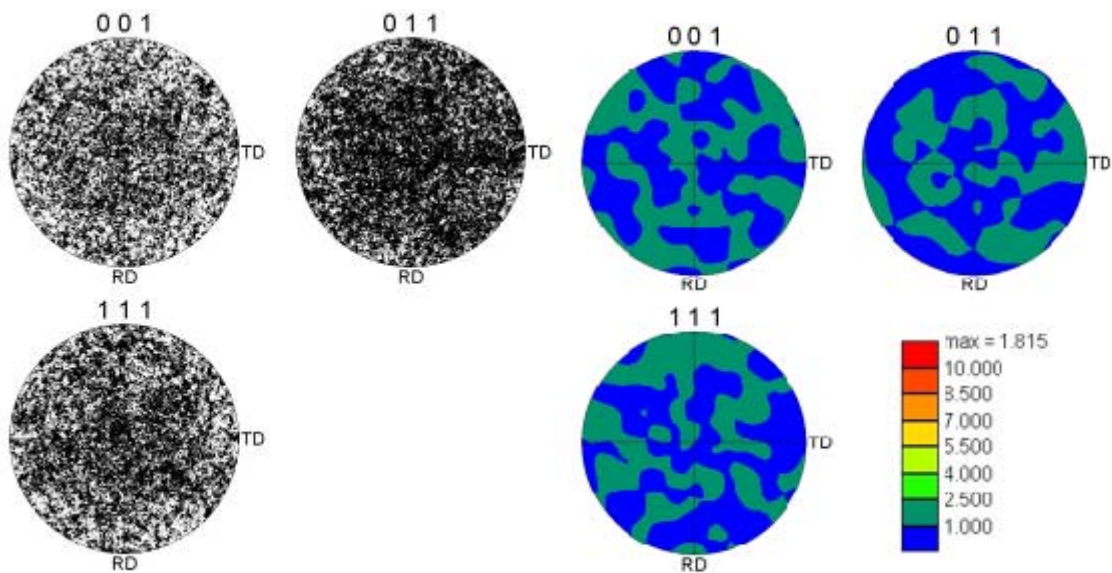


Figure 63. Multipass Pole Figure with coorisponding texture pole figure from Scan 8.

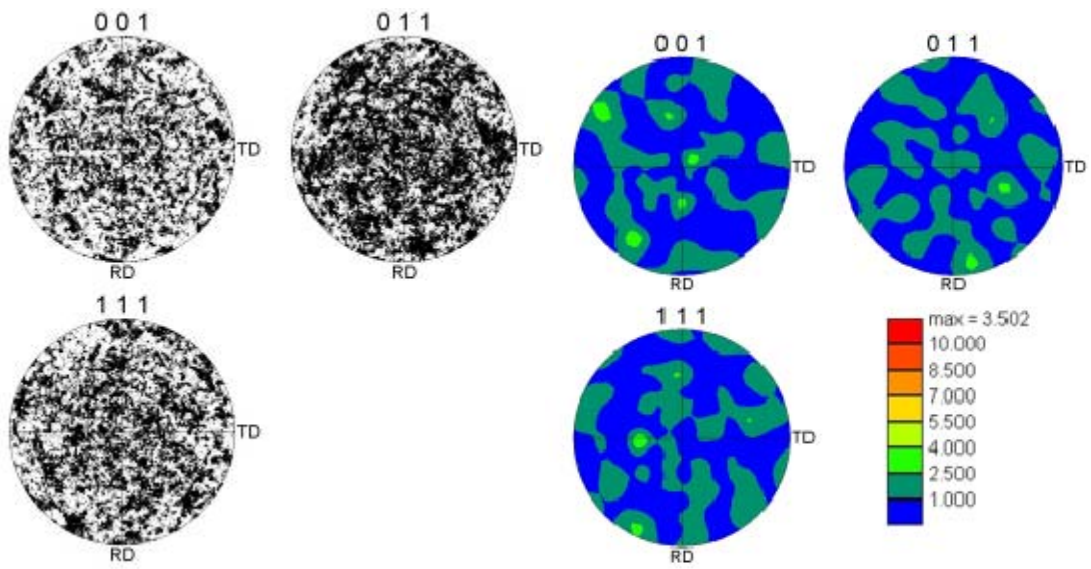


Figure 64. Multipass Pole Figure with coorisponding texture pole figure from Scan 9.

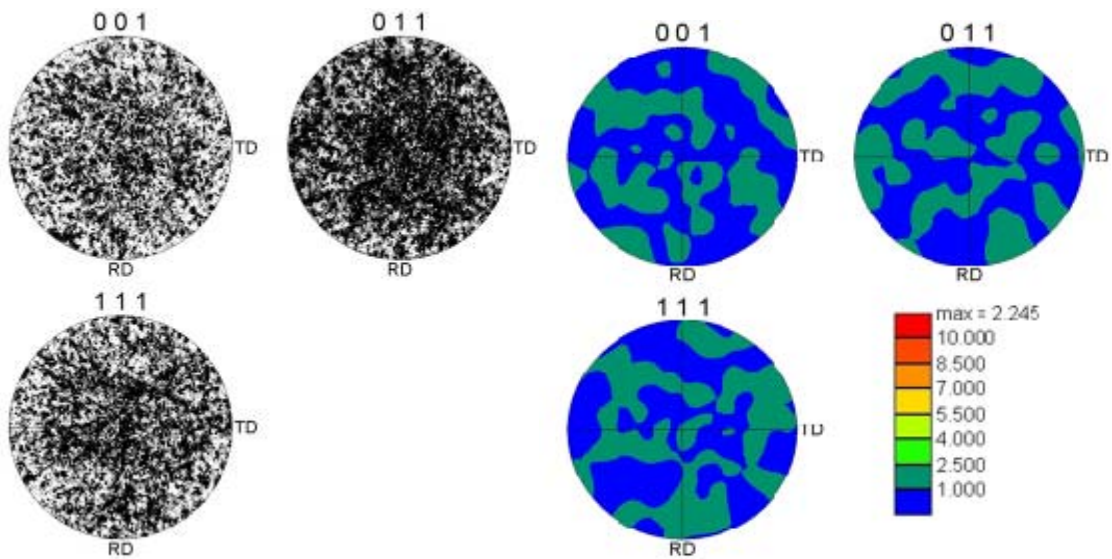


Figure 65. Multipass Pole Figure with coorisponding texture pole figure from Scan 10.

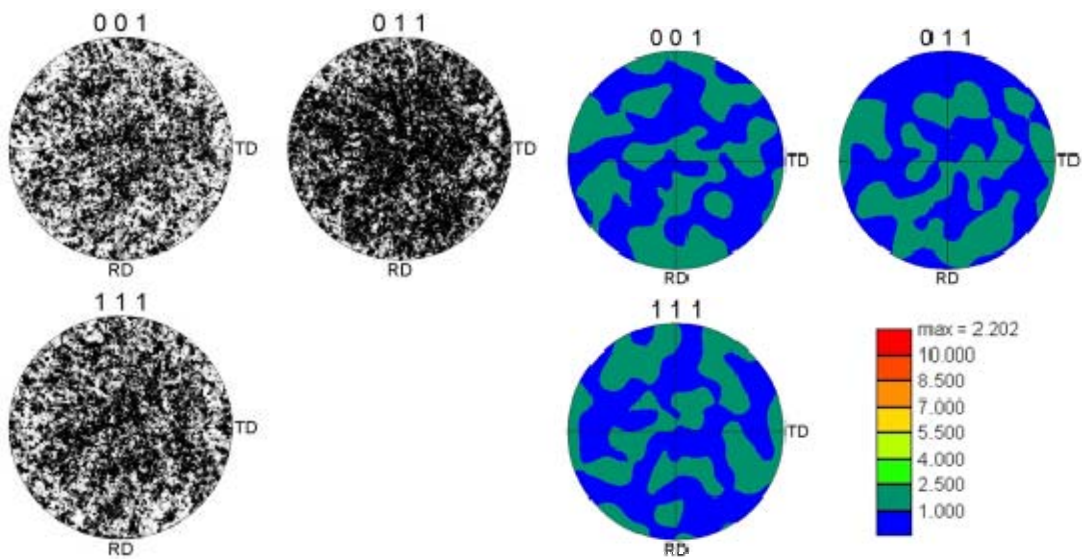


Figure 66. Multipass Pole Figure with coorisponding texture pole figure from Scan 11.

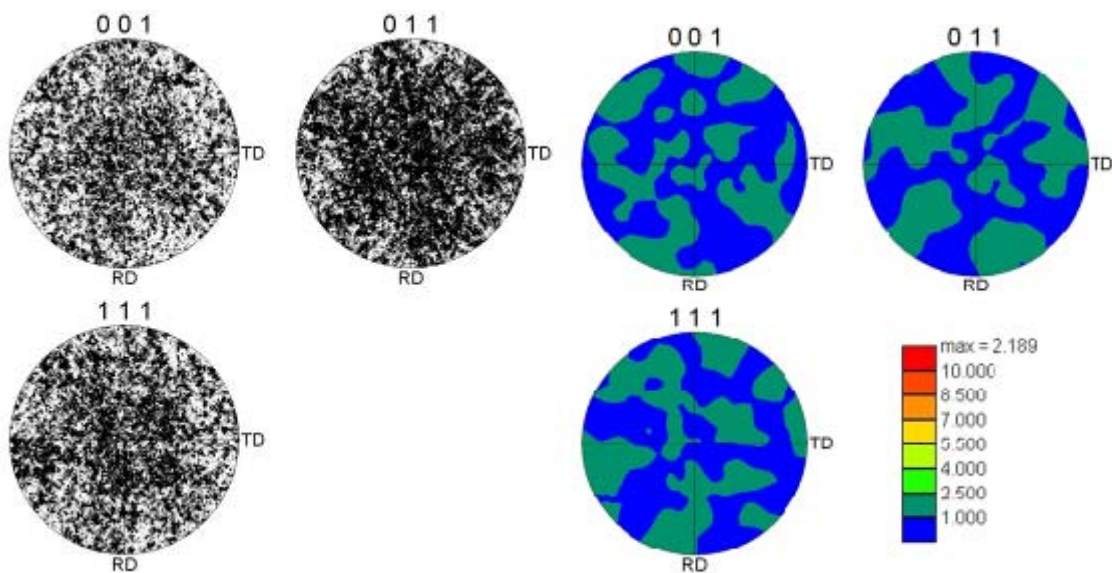


Figure 67. Multipass Pole Figure with coorisponding texture pole figure from Scan 12.

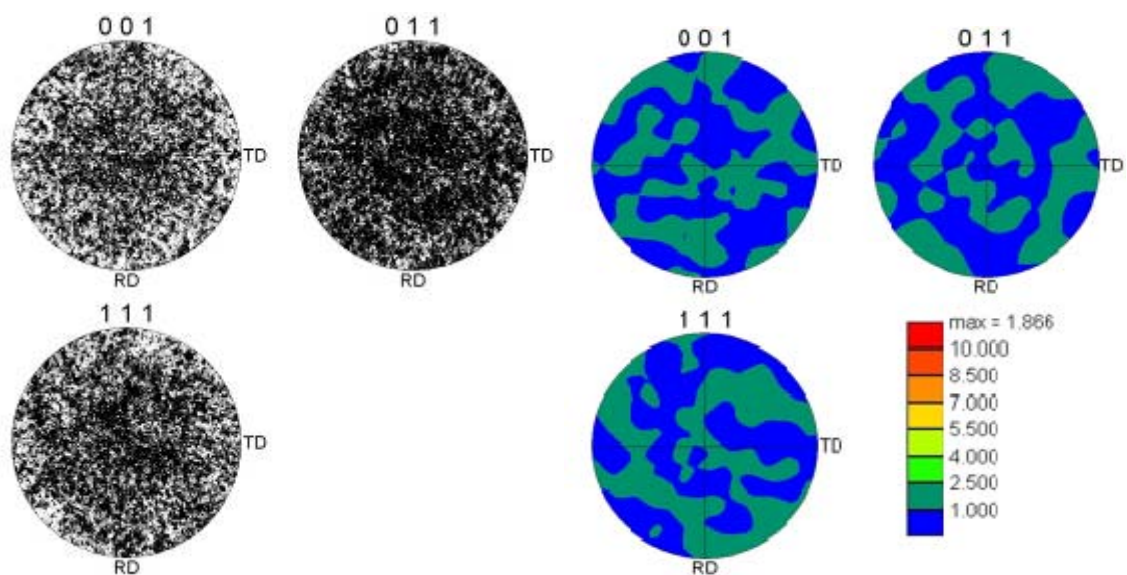


Figure 68. Multipass Pole Figure with corresponding texture pole figure from Scan 13.



## B. EXTRA DATA AND FIGURES FOR VERTICAL CENTERLINE

Table 8. Multi-pass Vertical Centerline Number Fraction of Grain Boundaries at a Misorientation Angle.

| Angle<br>[degrees]         | Multi-pass Vertical Centerline - Number Fraction |          |          |          |          |          |
|----------------------------|--|----------|----------|----------|----------|----------|
|                            | Scan A   | Scan B   | Scan C   | Scan D   | Scan E   | Scan F   |
| 3.575                      | 0.437804   | 0.429903 | 0.300053 | 0.117459 | 0.094265 | 0.118649 |
| 6.725                      | 0.110276   | 0.12809  | 0.116802 | 0.026144 | 0.022258 | 0.032869 |
| 9.875                      | 0.0611   | 0.050261 | 0.064165 | 0.017993 | 0.013214 | 0.01981  |
| 13.025                     | 0.026011   | 0.028111 | 0.029074 | 0.014952 | 0.014385 | 0.01468  |
| 16.175                     | 0.014628   | 0.014673 | 0.015971 | 0.015438 | 0.019768 | 0.01133  |
| 19.325                     | 0.007655   | 0.011874 | 0.017901 | 0.017147 | 0.016172 | 0.013931 |
| 22.475                     | 0.005606   | 0.004265 | 0.013762 | 0.013207 | 0.015938 | 0.015553 |
| 25.625                     | 0.007342   | 0.005714 | 0.008532 | 0.014377 | 0.01347  | 0.017566 |
| 28.775                     | 0.009164   | 0.008316 | 0.01003  | 0.018623 | 0.019832 | 0.021824 |
| 31.925                     | 0.021885   | 0.019433 | 0.018968 | 0.037174 | 0.031918 | 0.033849 |
| 35.075                     | 0.02769  | 0.041862 | 0.027702 | 0.04671  | 0.044664 | 0.042739 |
| 38.225                     | 0.020803   | 0.02271  | 0.023335 | 0.04142  | 0.0396   | 0.050809 |
| 41.375                     | 0.01716  | 0.015892 | 0.013356 | 0.041204 | 0.038579 | 0.041492 |
| 44.525                     | 0.022226   | 0.019663 | 0.019679 | 0.043111 | 0.046643 | 0.049419 |
| 47.675                     | 0.014798   | 0.012928 | 0.020339 | 0.036616 | 0.044409 | 0.045838 |
| 50.825                     | 0.021458   | 0.022924 | 0.024478 | 0.054285 | 0.048452 | 0.047549 |
| 53.975                     | 0.028402   | 0.026448 | 0.028337 | 0.056876 | 0.051176 | 0.050702 |
| 57.125                     | 0.051453   | 0.041121 | 0.042404 | 0.079925 | 0.06656  | 0.074503 |
| 60.275                     | 0.09434  | 0.095483 | 0.205012 | 0.307195 | 0.358336 | 0.296694 |
| 63.425                     | 0.000199   | 0.000329 | 0.000102 | 0.000144 | 0.000362 | 0.000196 |
| low angle                  | 0.635191   | 0.636365 | 0.510093 | 0.176548 | 0.144122 | 0.186008 |
| high angle                 | 0.364808   | 0.363635 | 0.489906 | 0.823452 | 0.855879 | 0.813992 |
| Total<br>Average<br>Number | 20.0351  | 19.7364  | 26.4441  | 41.218   | 42.9958  | 40.6086  |
| distance<br>into SZ        | -0.407   | -0.19    | -0.119   | 0        | 0.5      | 3.893    |

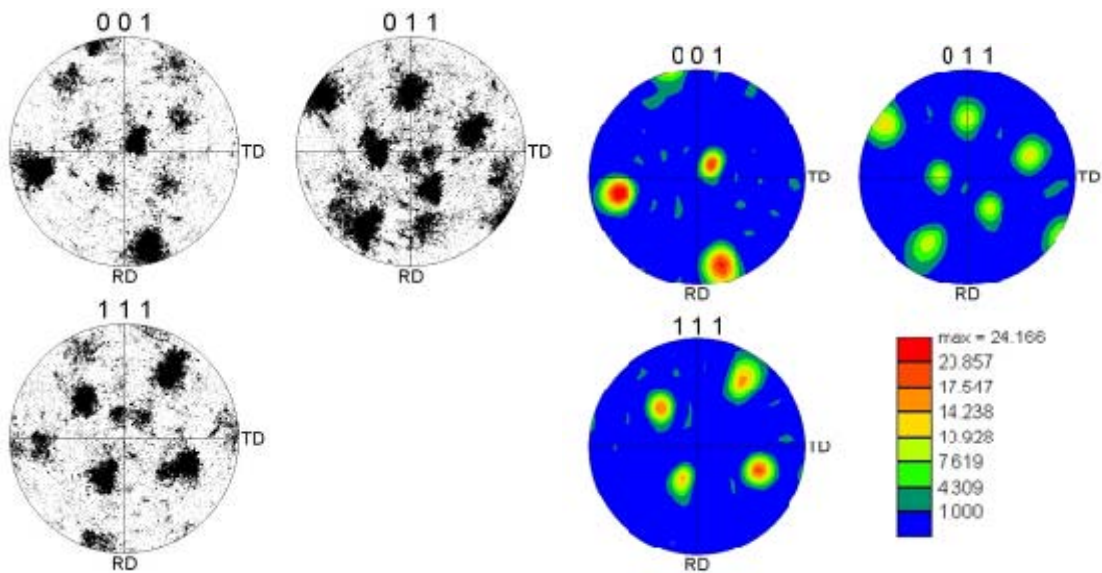


Figure 69. Multipass Pole Figure with coorisponding texture pole figure from Scan A.

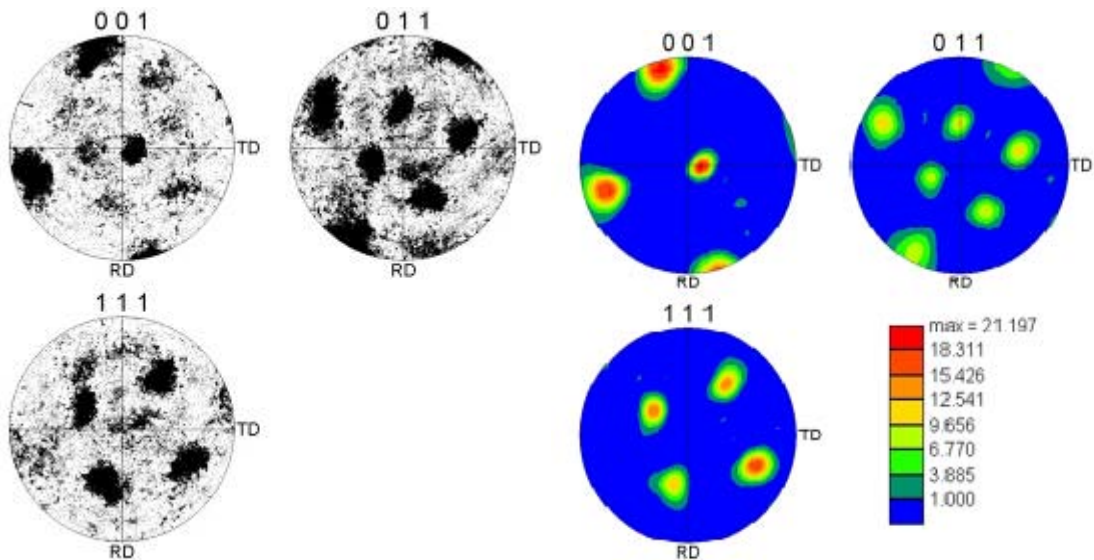


Figure 70. Multipass Pole Figure with coorisponding texture pole figure from Scan B.

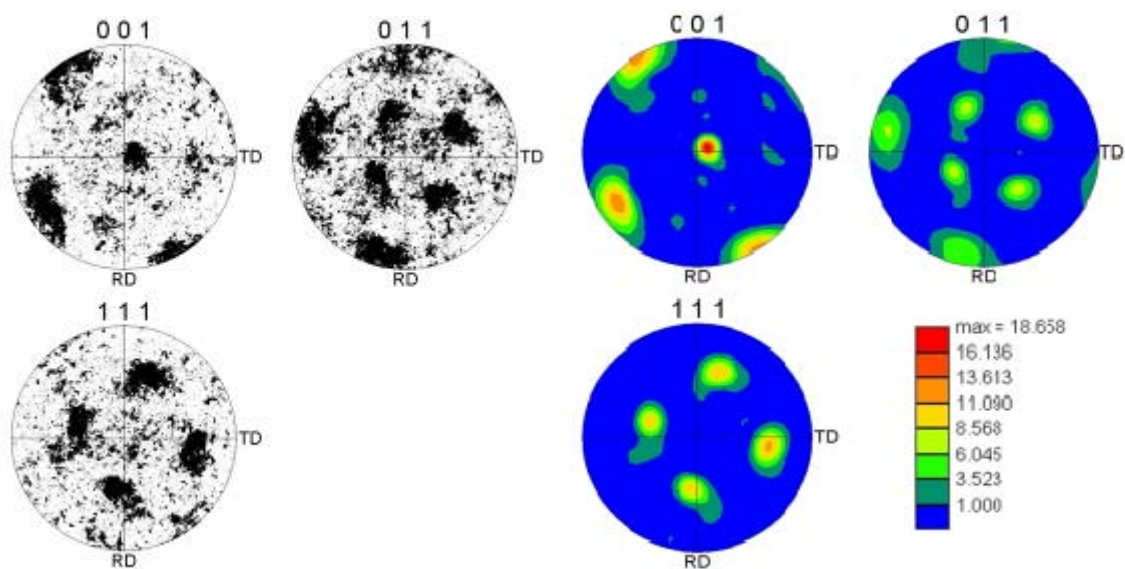


Figure 71. Multipass Pole Figure with coorisponding texture pole figure from Scan C.

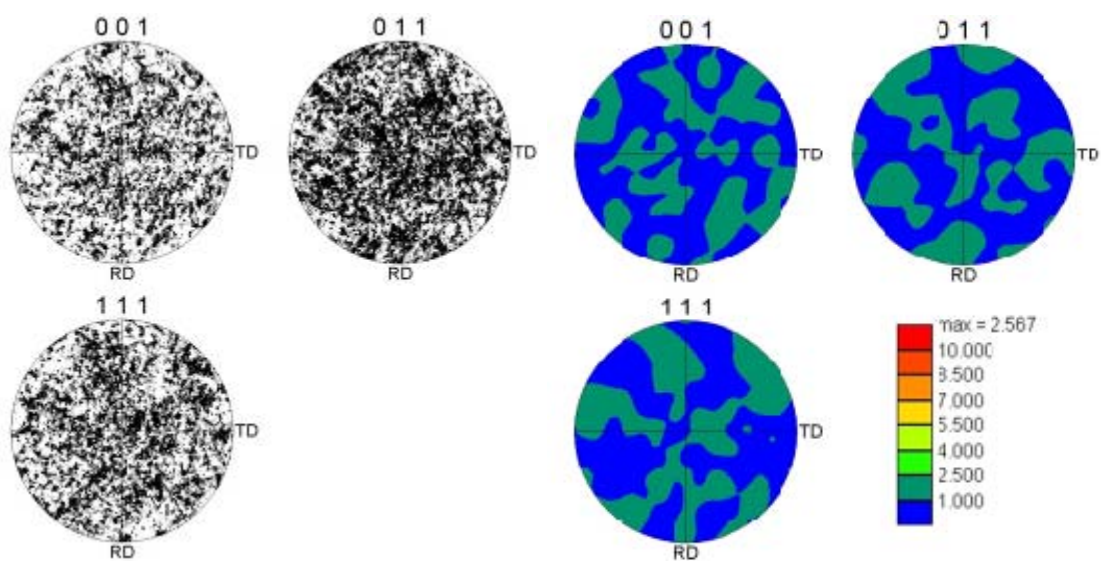


Figure 72. Multipass Pole Figure with coorisponding texture pole figure from Scan D.

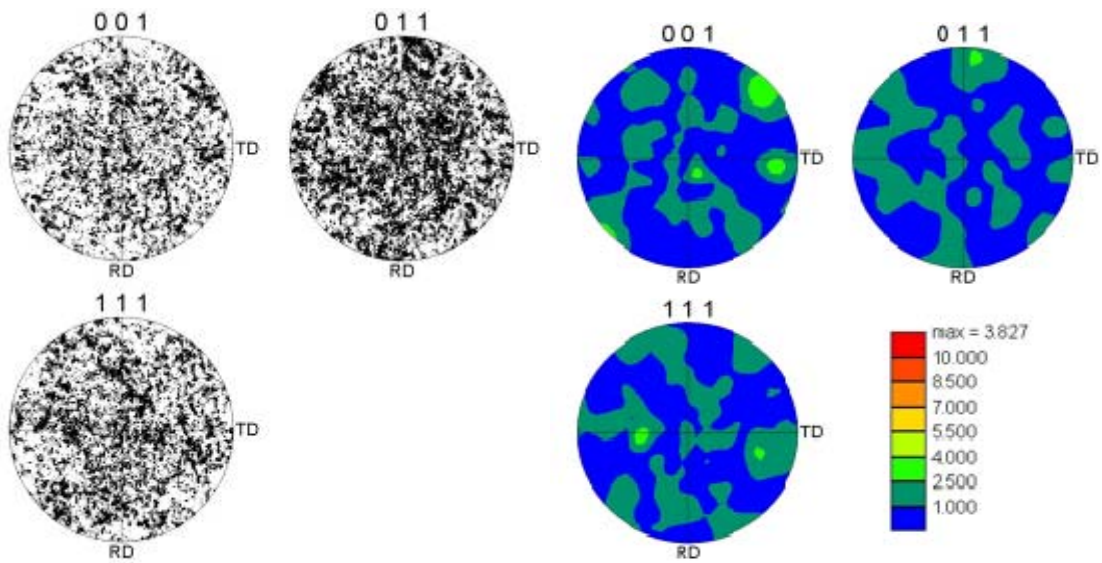


Figure 73. Multipass Pole Figure with corresponding texture pole figure from Scan E.

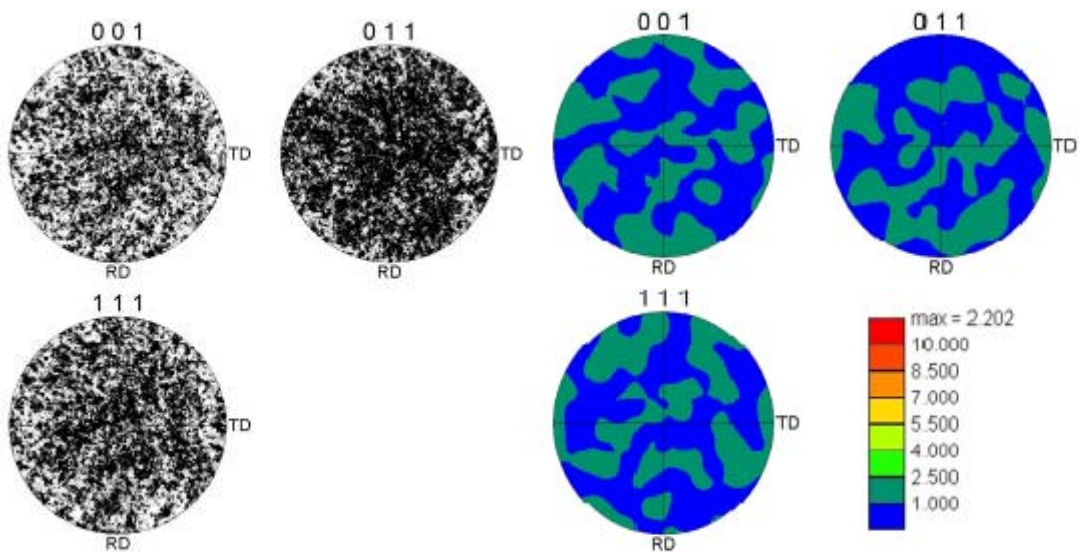


Figure 74. Multipass Pole Figure with corresponding texture pole figure from Scan F.



THIS PAGE INTENTIONALLY LEFT BLANK

## LIST OF REFERENCES

- [1] J. A. Duma. "Heat Treatments for Optimizing Mechanical and Corrosion Resisting Properties of Nickel-Aluminum Bronzes," *Naval Engineers Journal*, vol. 87, pp. 45–64, 1975.
- [2] T. R. McNelley and K. Oh-Ishi, "The Influence of Friction Stir Processing Parameters on Microstructure of As-Cast NiAl Bronze." *Metallurgical and Materials Transactions A*, vol. 36A pp. 1575–1585. June 2005.
- [3] W. M. Thomas et al., "Friction Stir Butt Welding," International Patent Appl. No. PCT/GB92/02203 and GB Patent Appl. No. 9125978. December 8, 1991, U.S. Patent No. 5,460,317 – from [16] in support of information by Stephan Kallee and Dave Nicholas TWI.
- [4] E. A. Nelson, "Microstructural Effects of Multiple Passes during friction stir processing of Nickel Aluminum Bronze," M.S. thesis, Dept. Mech. Eng., Naval Postgraduate School, Monterey, CA, December 2009.
- [5] R. A. Williams, "A Microstructural and Mechanical Property Correlation of Friction Stir Processed Nickel Aluminum Bronze," M.S. thesis, Dept. Mech. Eng., Naval Postgraduate School, Monterey, CA, September 2004.
- [6] R. S. Mishra and Z. Y. Ma, "Friction Stir Welding and Processing," *Materials Science and Engineering*, vol. 50, pp. 1–78, 2005.
- [7] M. D. Fuller, "Friction Stir Processing and Fusion Welding in Nickel Aluminum Propeller Bronze," M.S. Thesis, Dept. Mech. Eng., Naval Postgraduate School, Monterey, CA, 2006.
- [8] F. Hansan, A. Jahanafrooz, G. W. Lorimer, and N. Ridley, "The Morphology, Crystallography, and Chemistry of Phases in As-Cast Nickel-Aluminum Bronze," *Metallurgical Transactions A*, vol. 13A, pp. 1337–1345, 1982.
- [9] C. F. Walton Jr., "Microtextural Characterization of Shear Textures in the Thermo-Mechanically affected Zone of Friction Stir Processed Nickel Aluminum Bronze," M.S. thesis, Dept. Mech. Eng., Naval Postgraduate School, Monterey, CA,, June 2003.
- [10] T. Sourmail, P. Openacker, G. Hopkin and H. K. D. H. Bhadeshia, "Annealing twins" [PPT] Phase Transformations and complex Properties Research Group University of Cambridge. Retrieved from <http://www.msm.cam.ac.uk/phase-trans/abstracts/annealing.twin.html>

- [11] A. D. Rollett and P. Kalu, (2005) *Intro to X-ray Pole Figures 27-750 Advanced Characterization and Microstructural Analysis* [PPT], Carnegie Mellon department of Materials Science and Engineering, Retrieved from [neon.materials.cmu.edu/rollett/27750.old.Spg05/Intro.Xray.PFs.ppt](http://neon.materials.cmu.edu/rollett/27750.old.Spg05/Intro.Xray.PFs.ppt)
- [12] Y. H. Zhao, Y. T. Zhu, X. Z. Liao, Z. Horita, T. G. Langdon, “Tailoring stacking fault energy for high ductility and high strength in ultrafine grained Cu and its alloy” *Applied Physics Letter* 89, 121906, Applied Institute of Physics, 2006
- [13] J. H. Ree “Grain boundary Sliding in Experimental Deformation of Octachloropropane” *Journal of the Virtual Explorer*, vol. 2, 2000. Retrieved from <http://virtualexplorer.com.au/special/meansvolume/contribs/ree/index.html>
- [14] A. Kuper, H. Letaw Jr., L. Slifkin, E. Soder, and C. T. Tomizuka. “Self Diffusion in Copper” *Phys.Rev.* vol. 96, pp 1224–1225, 1954.
- [15] F.S. Buffington, K Hirano, M Cohen, “Self diffusion in Iron,” *Acta Metallurgica*, vol. 9, issue 5, pp. 434–439, May 1961.
- [16] R. S. Mishra, Z. Y. Ma, and I. Charit, *Mater. Sci. Engng. A*, vol. A341, pp. 307–310, 2003.
- [17] ASTM Standard B-148, 1997 (2009), “Standard Specification for Aluminum Bronze Sand Castings,” ASTM International, West Conshohocken, PA, 2006DOI:10.1520/B0148-97R09, Retrieved from [www.astm.org](http://www.astm.org)
- [18] A. D. Rollett “Thermomechanical Processing Textures – III” [PPT] Retrieved from [neon.materials.cmu.edu/rollett/27750/Metal\\_Textures\\_part3.ppt](http://neon.materials.cmu.edu/rollett/27750/Metal_Textures_part3.ppt)
- [19] L. S. Darken and R W. Gurry, *Physical Chemistry of Metals*, McGraw-Hill, NY, 1953.

## **INITIAL DISTRIBUTION LIST**

1. Defense Technical Information Center  
Ft. Belvoir, Virginia
2. Dudley Knox Library  
Naval Postgraduate School  
Monterey, California
3. Engineering and Technology Curricular Office, Code 34  
Naval Postgraduate School  
Monterey, California
4. Professor Terry R. McNelley, Code ME/Mc  
Naval Postgraduate School  
Monterey, California
5. Professor Sarath Menon  
Naval Postgraduate School  
Monterey, California